UNIVERSITÀ DEGLI STUDI DI UDINE

Corso di Dottorato di Ricerca in Ingegneria Industriale e dell'Informazione
Ciclo XXV

Tesi di Dottorato di Ricerca

EXPERIMENTAL ACTIVITY AND ANALYSIS OF PLC TECHNOLOGY IN VARIOUS SCENARIOS

Relatore:
Prof. Andrea M. Tonello

Dottorando:
Massimo Antoniali

Anno Accademico 2012/2013

Abstract

Power line communications (PLCs) have become a key technology in the telecommunication world, both in terms of stand-alone technology or a technology that can complement other systems, e.g., radio communications. Since PLCs exploit the existing power delivery grid to convey data signals, the application scenarios are multiple. Historically, PLCs have been deployed in outdoor low voltage (< 1 kV) power distribution networks for the automatic metering and the management of the loads. Today, the evolution of the electrical grid toward an intelligent and smart grid that dynamically manages the generation, the distribution and the consumption of the power makes this technology still relevant in this scenario. Therefore, PLCs have raised significant interest in recent years for the possibility of delivering broadband Internet access and high speed services to homes and within the home. The increase in demand for such services has inspired the research activity in the in-home scenario, both toward the direction of the development of independent or integrated solutions, with respect to already existing technologies. Another application scenario that has not been deeply investigated yet is the in-vehicle one, which includes the in-car, in-plane and in-ship scenario.

Since the power grid has not been designed for data communications, the transmission medium is hostile and exhibits high attenuation, multipath propagation and frequency selectivity, due to the presence of branches, discontinuities and unmatched loads. For the proper design of a power line communication (PLC) system, good knowledge of the grid characteristics in terms of propagation channel and disturbances is required. In this respect, we have performed experimental measurement campaigns in all the aforementioned scenarios. We aimed to investigate the grid characteristics from a telecommunication point of view.

In this thesis, we present the results of our experimental activity. Firstly, we analyze the outdoor low voltage and industrial scenario. We have carried out a measurement campaign in an artificial network that can resemble either an outdoor low voltage power distribution network or an industrial or marine power system. We have focused on the channel frequency response, the line impedance and the background PLC noise, within the narrow band and the broad band frequency ranges.

Then, we focus on the in-home scenario. In this context, we have studied the impact of the electrical devices (loads) connected to the power grid on the PLC medium characteristics and on the quality of the data communication. Their behavior has been investigated both in the time and frequency domain, in terms of load impedance and impulsive noise components

that they inject into the network.

Finally, we consider in-vehicle PLC, in particular the in-ship and in-car environment. Firstly, we summarize the results of a channel measurement campaign that we have carried out in a large cruise ship focusing on the low voltage power distribution network in the band 0-50 MHz. Thus, we present the results of an entire PLC noise and channel measurement campaign that we have performed in a compact electrical car.

Contents

List of Figures

List of Tables

List of Acronyms

ACF autocorrelation function

ACG average channel gain

ARIB Association of Radio Industries and Businesses

BB broad band

CB coherence bandwidth

CENELEC European Committee for Electrotechnical Standardization

CDF cumulative distribution function

C-CDF complementary cumulative distribution function

CFL compact fluorescent lamp

CM common mode

CP cyclic prefix

CSMA carrier sense multiple access

CTF channel transfer function

DB-RP distribution board-room panel

DFT discrete fourier transform

DM differential mode

D-NAP distribution network and protection laboratory

DS delay spread

DSO digital storage oscilloscope

DUT device under test

ECU electronic control unit

EMI electromagnetic interference

ESR equivalent series resistance

FCC Federal Communications Commission

I-UWB impulsive ultra wideband

LPTV linear periodically time variant

LTI linear time invariant

LV low voltage

MAC medium access control

MC multicarrier

MIMO multiple-input multiple-output

MV medium voltage

MV/LV medium voltage to low voltage

NB narrow band

OFDM orthogonal frequency division multiplexing

O-LV outdoor low voltage

PI power island

PL path loss

PLC power line communication

PLF power line filter

PRIME power line intelligent metering evolution

PSD power spectral density

RF radio frequency

RMS root mean square

RMS-DS root mean square delay spread

RTS real time simulator

SA spectrum analyzer

SCR silicon control rectifier

SG smart grid

SISO single-input single-output

SS-DB substation switchboard-distribution board

TL transmission line

VNA vector network analyzer

WG waveform generator

Introduction

In this thesis, we present the results of our experimental activity concerning the characterization of the PLC transmission medium. Both the propagation channel and the disturbances. We have investigated several scenarios where PLCs can be applied, i.e., the outdoor and industrial, in-home and in-vehicle scenarios.

The outdoor scenario is the native scenario for the PLC technology. The widespread coverage of the power distribution network and the possibility to access all the entities within the grid via the existing infrastructure are of fundamental importance. The main contributors to the development of PLC solutions have been the electric utility organizations [1]. In fact, the first PLC systems have been deployed in outdoor low voltage (LV, <1 kV) power distribution networks for the automatic metering and management of the loads. In recent years, we have assisted to the evolution of the electrical grid toward a more complex power generation and distribution system, i.e., an intelligent and smart grid (SG). Now, the electricity generated by the various entities of the grid is dynamically and smartly allocated. The three domains, i.e., the generation, the distribution and the consumption of power, operate on a collaborative and cooperative way. Clearly, the management of the SG requires a pervasive telecommunication infrastructure that enables bidirectional, reliable, short and long distance communications. In this context, PLC is a suited technology. Nowadays, the most important PLC technologies that have been developed for command and control applications within the smart grids are the ERDF G3-PLC [2] and the PRIME [3] solutions. G3-PLC is a communication protocol that allows for the remote management of the complete supply chain, from the electricity suppliers to the consumers. Furthermore, G3-PLC is suitable for the automatic meter reading. G3-PLC was initially supposed to operate in Europe, and to transmit in the Cenelec A band (3-95 kHz). Later extensions of the original standard enabled G3-PLC to operate in Cenelec bands B (95-125 kHz), C (125-140 kHz), and D (140-148.5 kHz) [4] and in the frequency band up to 500 kHz regulated by the federal communication commission (FCC) [5]. In all cases, G3-PLC adopts orthogonal frequency division multiplexing (OFDM) in combination with the use of a cyclic prefix (CP). G3-PLC offers data rate up to 34 or 240 kbps when working on the Cenelec A or FCC band, respectively. The MAC layer is based on CSMA [6]. Also the PRIME solution has the physical layer based on OFDM, and the MAC layer based on CSMA. PRIME operates in the Cenelec A band and offers data rate up to 128 kbps.

The PLC devices that work in the frequency bands above specified are referred to as narrow band (NB) devices. This is to distinguish them from broad band (BB) devices that use a higher frequency spectrum and wider bandwidths and allow high rate communications typically for in-home applications such as high speed Internet connection and networking. BB PLC technologies for home networking are Home Plug AV [7] and HD-PLC [8]. Basically, Homeplug AV is an OFDM-based standard that operates in the 2-28 MHz frequency range, while HD-PLC adopts a Wavelet-OFDM modulation method in the same frequency range. Recently, in December 2010, the IEEE P1901 [9] working group has standardized the PHY layer specifications for broad band over power line networks based on the above solutions. The possibility of exploiting the frequency spectrum up to 100-300 MHz for PLC purposes has also gained research interest in recent years [1]. BB PLC solutions offer data rates from 200 Mbps up to 1 Gbps. Clearly, the possibility of delivering broadband Internet and high speed services within the homes without the need of new wires has inspired the research activity. In this respect, the interest moves toward the direction of the development of independent or integrated solutions, w.r.t. the existing wired and wireless technologies. Nevertheless, the high bandwidth and the scalable functionalities of BB PLC can also provide a cost-effective possibility to migrate to advanced remote control and monitoring SG applications.

While outdoor and in-home PLC have raised significant interest, in-vehicle PLC (which includes the in-car, in-plane and in-ship scenarios) is an application that has not been deeply investigated yet. PLC simplifies the design of the in-vehicle communication network and more importantly it saves weight and cost. PLC is suitable for communications between electronic control units (ECUs) inside a vehicle, such as sensors and electronic equipments, in addition or in alternative to existing low-speed and high-reliability buses, e.g., LIN-bus and CAN-bus inside a car. Concerning the electrical vehicles, PLC is an interesting solution also due to the intrinsic nature of the electric power system, w.r.t. the wiring infrastructure of standard vehicles. In fact, electrical vehicles are equipped with a dedicated power grid to supply the electric engine. Battery management to control charge, discharge and energy flow to the electric engine and electronic equipments can be made by integrated boards and ECUs connected via power cables. Furthermore, PLC can support advanced automotive control applications that need relatively high speed, flexibility and scalability for complex networks, e.g., within an airplane, or video streaming between external safety-cameras and in-vehicle displays, or multimedia and entertainment services that would require the installation of new dedicated wires or optical fibers with the consequent increase of weight, cost and complexity of the wiring harness. The in-ship scenario is different. For example, cruise ships are intrinsically hotel and entertainment structures for passengers. Thus, multimedia services are of great interest. PLC can exploit the existing power distribution infrastructure to deliver high speed services to every cabin or to every deck. As a consequence, the research interest moves toward the direction of applying BB PLC solution developed for the in-home scenario.

Research Activity and Thesis Contributions

Channel and noise characterization and modeling and experimental activity are of key importance in PLC. Clearly, the two research areas are strictly related to each other. Statistical approaches to model the PLC channel and the interferences within the grid are based on experimental results. At the same time, measurement results allow to make comparison with the ones obtained by simulation. Our research activity has investigated several scenarios where PLCs can be applied.

In this thesis, we present the results and the contributions of our research activity.

Firstly, in Chapter 1, we discuss the principles and methodologies that we have used in the PLC measurement campaigns. We present an overview of the methodologies that allow the investigation of the grid characteristics in terms of propagation channel and disturbances.

In Chapter 2, we summarize the results of the experimental measurement campaign that we have carried out in the distribution network and protection laboratory (D-NAP) of the University of Strathclyde, Glasgow, UK. The D-NAP is an artificial network that can resemble either an outdoor LV (O-LV) power distribution network or an industrial or marine power system. We have focused on the channel frequency response, the line impedance and the background PLC noise, within the NB and the BB frequency range.

Thus, we have focused on the in-home scenario. In this context, we have carried out an intensive measurement campaign in Italy, where we have collected more than 1200 channel responses in different sites. We have performed measurements between all couples of available outlets for each site, in a frequency range up to 300 MHz, providing a realistic description of the path loss and the line impedance that characterizes the signal paths. The results can be found in [10]. In Chapters 3 and 4, we analyze the results of our study of the impact of the electrical devices (loads) connected to the power grid on the PLC medium characteristics and on the quality of the data communication. Their behavior has been investigated both in the time and frequency domain, in terms of load impedance and impulsive noise components that they inject into the network, in the NB and BB frequency band.

Finally, we have considered the in-vehicle PLC, in particular the in-ship and in-car environment. In Chapter 5, we summarize the results of a channel measurement campaign that we have carried out in a large cruise ship focusing on the low voltage power distribution network in the band 0-50 MHz. In Chapter 6, we present the results of an entire PLC noise and channel measurement campaign that we have performed in a compact electrical car.

Related publications

1. M. Antoniali, A. M. Tonello, M. Lenardon, and A. Qualizza, "Measurements and Analysis of PLC Channels in a Cruise Ship," in *Proc. IEEE Int. Symp. on Power Line Commun. and Its Appl. (ISPLC)*, pp. 102-107, Apr. 2011. **Best Student Paper Award**.

2. A. M. Tonello, M. Antoniali, F. Versolatto, and S. D'Alessandro, "Power Line Communications for In-car Application: Advanced Transmission Techniques," in *Proc. of the 5th Biennial Workshop on Digital Signal Processing for In-Vehicle Systems*, Sept. 2011.

3. M. Antoniali, M. Girotto, and A. M. Tonello, "In-car Power Line Communications: Advanced Transmission Techniques," *International Journal of Automotive Technology*, accepted, Dec. 2012.

4. M. Antoniali, A. M. Tonello, and F. Versolatto, "A Study on the Optimal Receiver Impedance for SNR Maximization in Broadband PLC," *Journal of Electrical and Computer Engineering*, vol. 2013, Article ID 635086, 11 pages, 2013.

5. M. Antoniali, M. De Piante, and A. M. Tonello, "PLC Noise and Channel Characterization in a Compact Electrical Car," *IEEE Int. Symp. on Power Line Commun. and Its Appl. (ISPLC)*, accepted, Jan. 2013.

6. M. Antoniali and A. M. Tonello, "Characterization of Load Impedances in Home Power Line Grids," *IEEE Transactions on Instrumentation and Measurement*, submitted to, Feb. 2013.

7. A. M. Tonello, M. Antoniali, and F. Versolatto, "Time-Frequency Characterization of the PLC Noise," *IEEE Transactions on Electromagnetic Compatibility*, to be submitted to, 2013.

Chapter 1

PLC Measurements

In this chapter, we discuss the principles and methodologies that we have used in the PLC measurement campaigns. The methodologies are based on the review of the methodologies widely adopted by the PLC community, the theory and our experimental engineering experience.

1.1 Introduction

Regardless the considered application scenario, the PLC communication port is the generic access point composed by two feeding conductors of the power grid between which the PLC transceiver signals. Thus, the grid is modeled as a N-port network, where N is the number of access points. In practice, the two feeding conductors are the line (hot) and the neutral wires of a domestic electrical plant or the positive and the negative wires of an electric power system of a vehicle. One of the two conductors is considered the reference conductor, e.g., the neutral wire or the negative one of the aforementioned examples. The objective of the experimental activity is the characterization of the transmission medium represented by the grid section between any couples of access points, i.e., the PLC channel, and the evaluation of the interferences within the grid, from a data transmission point of view. The data communication is between any pair of the ports of the N-port network, namely, the transmitter and receiver ports.

1.1.1 Power Grid Model

Herein, we assume the transmitter to be connected to port 1 and the receiver to port 2 of the power grid and we refer to Fig. 1.1. $V_i(f)$ and $I_i(f)$ are the phasors at frequency f of the voltage and of the current of the i-th port, respectively, with $i = 1, 2$. Note that $I_1(f)$ flows into the transmitter port while $I_2(f)$ flows out of the receiver port. The use of this convention will be clarified in the following. The transmitter is modeled as a real voltage source with its own internal impedance, and the receiver as a passive load. $V_s(f)$

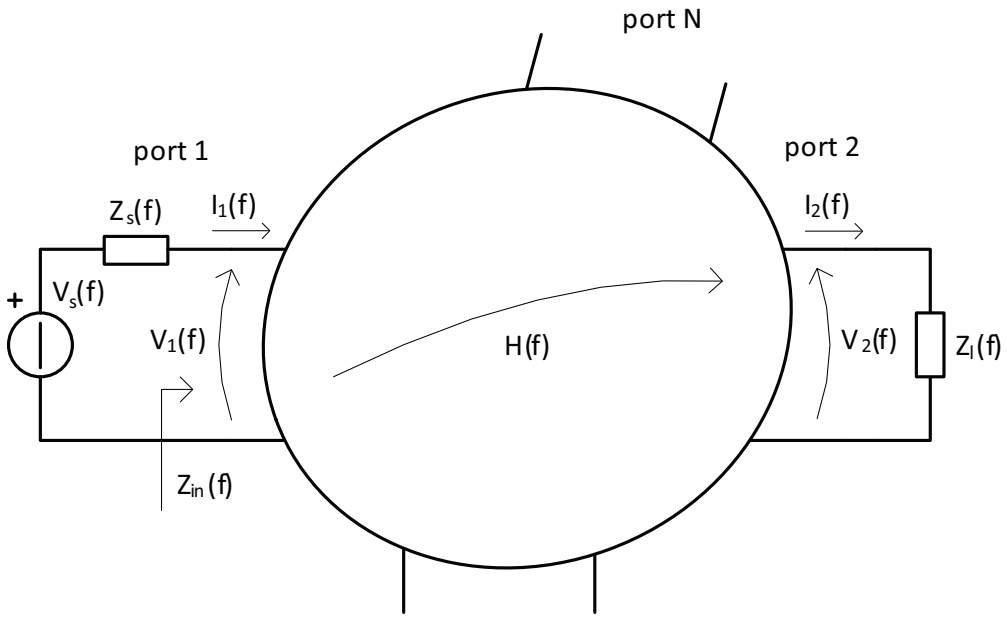

Figure 1.1: Equivalent model of the power grid as a N-port network. The power line link between the transmitter port (port 1) and the receiver port (port 2) is modeled as a two-port network.

is the complex amplitude of the source signal, $Z_s(f)$ denotes the internal impedance of the transmitter and $Z_l(f)$ is the load impedance that is connected at the receiver port.

We define the channel transfer function (CTF) $H(f)$ as the ratio between the receiver and the transmitter ports voltages, in the frequency domain. In the same way, the input impedance $Z_{in}(f)$, or the line impedance, is defined as the ratio between the voltage and the current of the transmitter port.

Concerning the noise, we consider the sum of the background and impulsive contributions at the receiver port.

1.1.2 Loads Model

The PLC medium and the quality of the data communication within the power grid are strongly affected by the presence of unmatched, time variant and noisy loads. Thus, we are also interested on the characterization of the loads connected to the power grid in terms of voltage-to-current relation between their feeding conductors and in terms of the noise components that they inject into the network.

1.1.3 Coupling

Coupling is an important aspect of PLC measurements. The couplers are basically high-pass filters that protect the measurement equipment from the power supply voltage. In the desired frequency range, the frequency response of the couplers must be flat, such that they

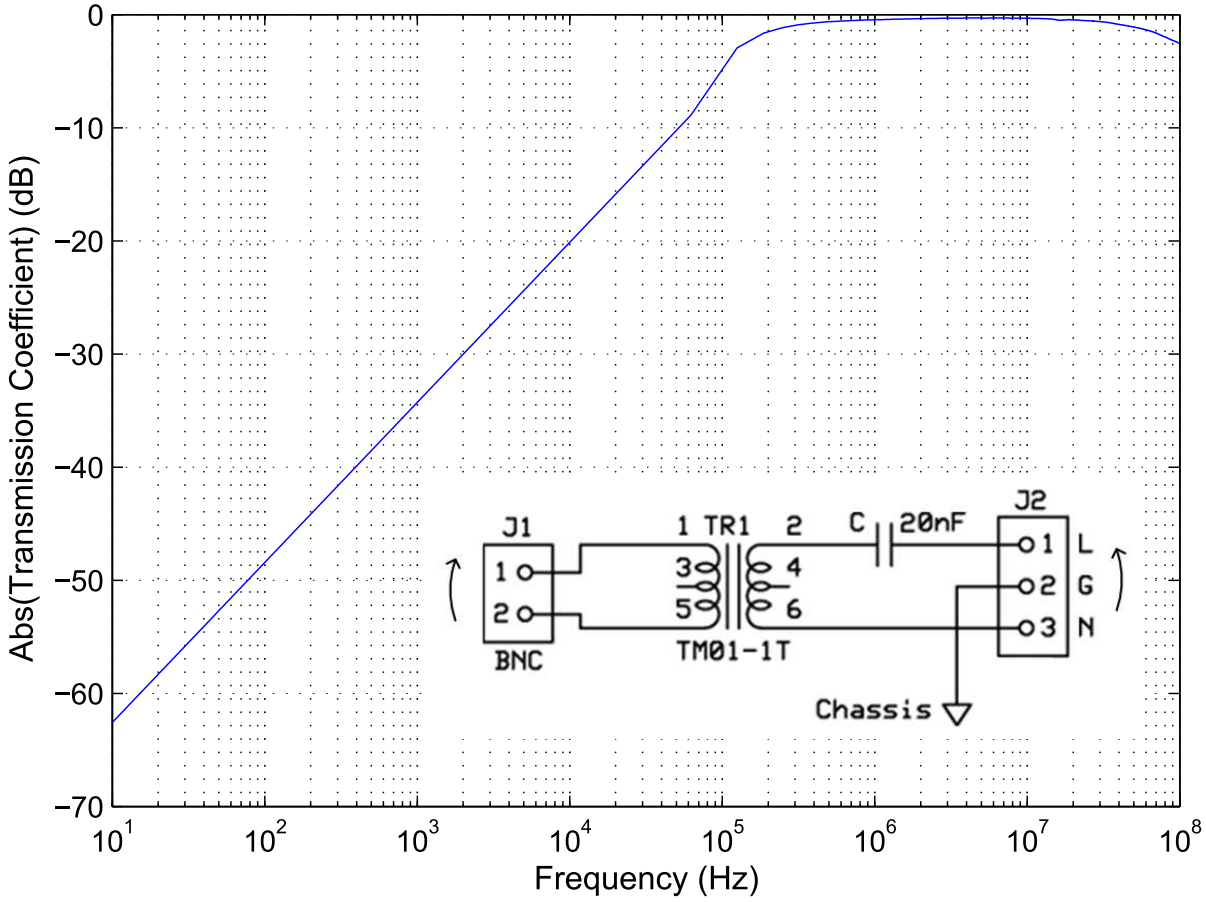

Figure 1.2: Transmission coefficient and schematic of the BB capacitive coupler used for the outdoor and industrial, in-home, and in-car PLC measurements, in the 2-100 MHz frequency range.

do not affect the PLC measurements.

There exist capacitive and inductive couplers. Basically, inductive couplers consist of a toroidal magnetic core. Inductive couplers exploit the mutual coupling between the power cables and the windings of the coupler itself wrapped around the core. Typically, they are used for medium voltage (MV) applications. For LV purposes, capacitive couplers are preferred. Basically, capacitive couplers consist of a radio frequency (RF) transformer (to provide galvanic insulation from the power grid and impedance adaptation) and a capacitor (to filter the DC or AC power supply signal). In the following, we model the couplers as linear time invariant (LTI) two-port networks. As an example, in Fig. 1.2, we show the schematic and the magnitude of the transmission coefficient (see Appendix A) from the port of the coupler directly connected to the measurement equipment (J1, typically a BNC/SMA connector) to the port connected to the power grid (J2). We refer to the BB capacitive coupler that we have used for the outdoor and industrial, in-home, and in-car PLC measurements, in the 2-100 MHz frequency range.

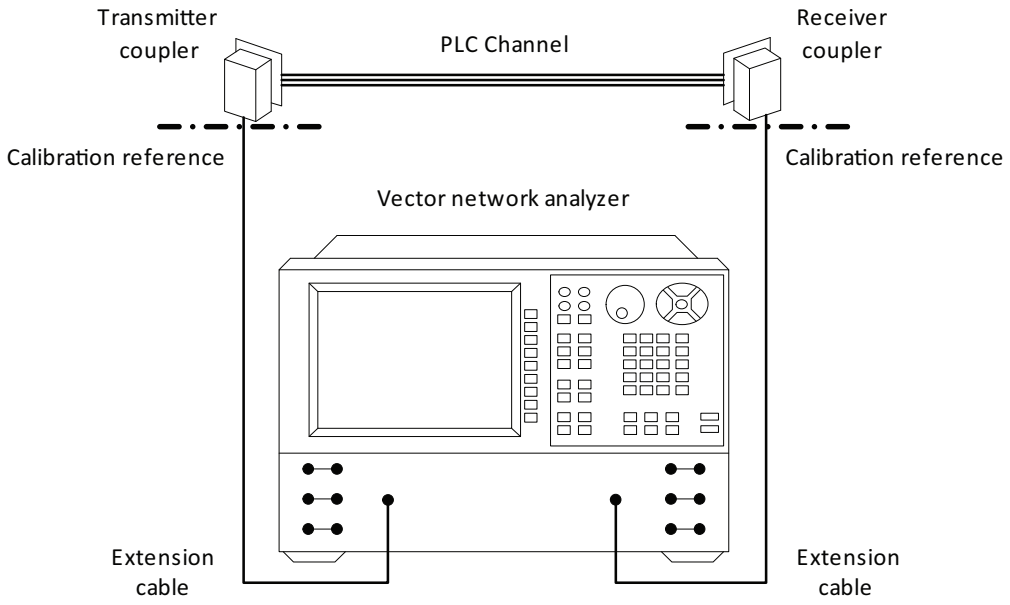

Figure 1.3: Frequency domain approach for PLC channel and line impedance measurements.

1.2 PLC Channel Measurements

The evaluation of the PLC CTF can be performed using two different approaches, i.e., in the frequency and time domain. Hereafter, we refer to the power grid between any transmitter and receiver port as a two-port network.

1.2.1 Frequency Domain Approach

The rigorous approach for the full-characterization of the power grid between couples of access points is the frequency domain one. In Fig. 1.3, we report the schematic of the frequency domain setup. Basically, it uses a two-port vector network analyzer (VNA). This approach can be applied when the transmitter and the receiver access points are close enough to be connected to the same VNA, in combination with extension cables. Nevertheless, the attenuation of the extension cables reduces the effective dynamic range of the instrument. Thus, low loss cables must be used.

The two-port VNA allows for the evaluation of the scattering parameters of the two-port network under test connected to its ports, in the frequency range of interest. The scattering parameters relate the incident and reflected voltage waves at the ports of the network. In Appendix A, we provide further details on the scattering parameters. According to Fig. 1.3, if the standard full 2-port calibration of the instrument is performed including the two extension cables (see the calibration reference), the VNA returns the scattering parameters of the two-port network under test given by the transmitter coupler, the PLC channel and the receiver coupler.

Now, from the measured scattering matrix, it is possible to obtain the transmission matrix

(see Appendix A), that relates the voltages and the currents of the ports of the network under test. The characterization in terms of the transmission matrix is convenient when a cascade connection of multiple two-port networks is deployed. In fact, the transmission matrix of the cascade is equal to the product of the transmission matrices representing the individual networks. This property is known as the chain rule of the transmission matrices. A fundamental prerequisite is the convention of the currents at the input and output ports of each individual network. In fact, the (positive) current that flows out of the output port of a two-port network is the (positive) current that flows into the input port of the subsequent two-port network.

Thus, if $\mathbf{T}_{measure}(f)$ is the transmission matrix at frequency f obtained from the measure

$$\mathbf{T}_{measure}(f) = \mathbf{T}_{coupler,tx}(f)\mathbf{T}_{plc}(f)\mathbf{T}_{coupler,rx}(f), \tag{1.1}$$

were $\mathbf{T}_{coupler,tx}(f)$, $\mathbf{T}_{plc}(f)$ and $\mathbf{T}_{coupler,rx}(f)$ are the transmission matrices of the transmitter coupler, of the PLC channel and of the receiver coupler, respectively, at frequency f. Since the couplers are modeled as LTI two-port networks, their representation in terms of transmission matrix is straightforward. Thus, from the chain rule, their effect is removed and the transmission matrix of the PLC channel is given by

$$\mathbf{T}_{plc}(f) = \mathbf{T}^{-1}_{coupler,tx}(f)\mathbf{T}_{measure}(f)\mathbf{T}^{-1}_{coupler,rx}(f). \tag{1.2}$$

Now, the transmission matrix of the PLC channel $\mathbf{T}_{plc}(f)$ relates the voltages and the currents at the transmitter and receiver ports of the power grid (cf. Fig. 1.1) as follows

$$\begin{bmatrix} V_1(f) \\ I_1(f) \end{bmatrix} = \underbrace{\begin{bmatrix} A(f) & B(f) \\ C(f) & D(f) \end{bmatrix}}_{\mathbf{T}_{plc}(f)} \begin{bmatrix} V_2(f) \\ I_2(f) \end{bmatrix}. \tag{1.3}$$

Thus, the CTF reads

$$H(f) = \frac{V_2(f)}{V_1(f)} = \frac{1}{A(f) + B(f)/Z_l(f)}. \tag{1.4}$$

The transmission matrix approach allows for the computation of the CTF for any load configuration, i.e., for any value of $Z_l(f)$. Furthermore, by inverting the transmission matrix $\mathbf{T}_{plc}(f)$, it is possible to obtain the CTF of the reverse channel, i.e., assuming the transmitter connected to port 2 and the receiver to port 1 of the power grid.

The frequency domain approach is suitable for time invariant and time variant channel measurements. To investigate the time variant behavior of the PLC channel, the zero-span mode of the VNA is exploited. This feature allows for the evaluation of the two-port network parameters at a certain frequency, in a finite number of time instants. This approach is particularly interesting in the in-home scenario. As it will be explained, the PLC channel

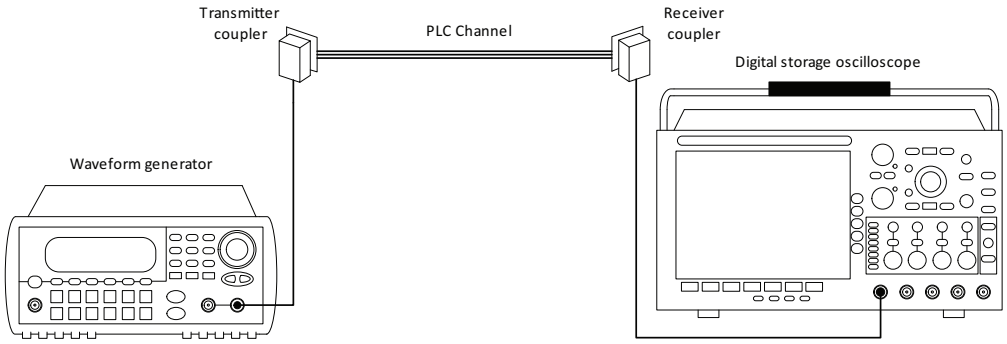

Figure 1.4: Time domain approach for PLC channel measurements.

is affected by the non-linearity of the loads. Thus, the PLC channel is periodically time variant, with a repetition frequency integer multiple of the mains frequency. If the time span is fixed equal to the mains period and the VNA is synchronized to the mains cycle, the time variant behavior can be appreciated. The equations that relate the voltages and the currents at the transmitter and receiver ports are the same of (1.1)-(1.4). Now, all the quantities are expressed at the time t, at the frequency f, e.g., $H(t, f)$. Thus, the PLC channel is modeled as a linear periodically time variant (LPTV) two-port network.

1.2.2 Time Domain Approach

The time domain approach consists of injecting a wideband pulse into the power grid at the transmitter side and acquiring it at the receiver side. Therefore, the CTF is obtained via discrete Fourier transform (DFT) of the transmitted and received signals. As depicted in Fig. 1.4, the time domain approach uses a combination of a waveform generator (WG) and a digital storage oscilloscope (DSO). The bandwidth of the pulse is a function of the desired frequency range. The sampling rate of the DSO is set in order to avoid aliasing components due to the transmitted pulse is not strictly limited in bandwidth in practice. This approach is suitable for the evaluation of the CTF between distant access points, that can not be connected to the same VNA exploiting the frequency domain approach.

As for the frequency domain approach, this setup allows time invariant and time variant measurements. To this aim, a burst of wideband pulses is injected into the grid. The number of subsequent pulses is a function of the desired time span and resolution.

To remove the effect of the couplers, the frequency response of the coupler-to-coupler connection is subtracted from the measured response.

1.3 PLC Impedance Measurements

As mentioned above, the input impedance, or the line impedance, is defined as the ratio between the voltage and the current of the transmitter port. In communication terms,

the line impedance is the load seen by the transmitter. The line impedance varies from access point to access point and it is extremely variable due to the loads connected to the power grid. Thus, also the knowledge of the impedance of the loads is of key importance. The measurements for the line and load impedance characterization are performed in the frequency domain, using a VNA.

1.3.1 Line Impedance Measurements

We refer to Fig. 1.1 and to the frequency domain approach for the PLC channel measurements. According to (1.3), the transmission matrix $\mathbf{T}_{plc}(f)$ relates the voltages and the currents of the transmitter and receiver ports. Thus, the line impedance reads

$$Z_{in}(f) = \frac{V_1(f)}{I_1(f)} = \frac{A(f) + B(f)/Z_l(f)}{C(f) + D(f)/Z_l(f)}. \tag{1.5}$$

Again, the transmission matrix approach allows for the computation of the line impedance for any value of the receiver impedance. Furthermore, the network impedance at the receiver port, or the output impedance, can also be addressed as

$$Z_o(f) = \frac{V_2(f)}{-I_2(f)} = \frac{B(f) + D(f)Z_s(f)}{A(f) + C(f)Z_s(f)}. \tag{1.6}$$

The output impedance can be interpreted as the line impedance at the port 2 when the impedance $Z_s(f)$ is connected to the port 1.

As for the PLC channel measurements, the time variant input and output impedances are obtainable exploiting the zero-span mode of the VNA, i.e., $Z_{in}(t, f)$ and $Z_o(t, f)$.

1.3.2 Load Impedance Measurements

We are interested on the characterization of the loads connected to the power grid in terms of the voltage-to-current relation between their feeding conductors. In Fig. 1.5, we depict the schematic of the load impedance measurement setup. Simply, we refer to the in-home scenario, where the electrical appliances connected to the power grid are modeled as loads. The VNA measures the reflection coefficient $\rho(f)$ of the device under test (DUT) from which the impedance value is obtained.

The loads must be supplied, thus the port of the VNA is connected to the power grid through a coupler. To compensate the effect of the power grid and of the coupler, the calibration reference of the VNA must be fixed after the coupler, on the grid side. This means that the coupler should be connected to the power grid during the 1-port reflection calibration of the VNA. Clearly, the procedure of the calibration is not the standard one. To emulate the standard ‘open’, a measurement is performed without any load connected to the power grid. The standard ‘short’ is replaced with a high voltage capacitor whose

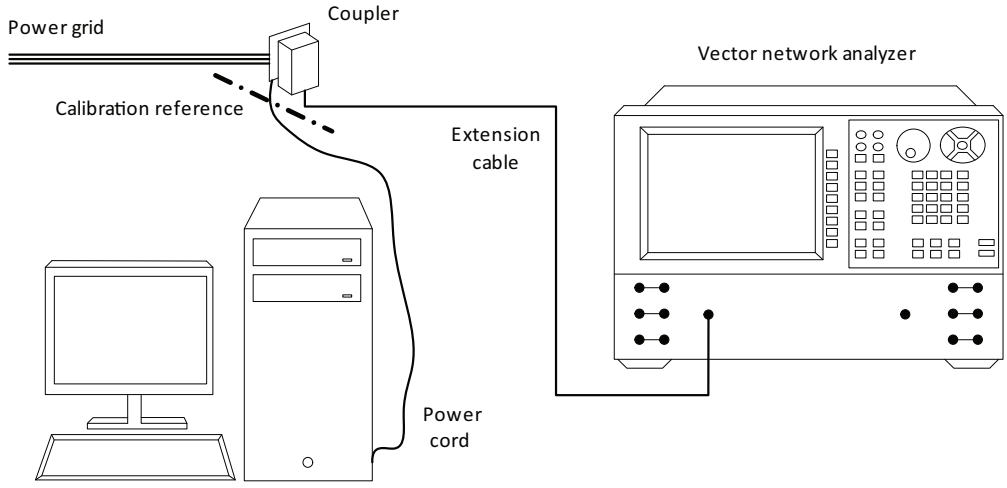

Figure 1.5: Frequency domain approach for PLC load impedance measurements.

impedance is negligible in the frequency range of interest. The standard 'load' is replaced with the series combination of the aforementioned capacitor and the standard load.

From the corrected reflection coefficient, the effective impedance value of the load is obtained as follows

$$Z(f) = Z_0 \frac{1+\rho(f)}{1-\rho(f)}, \tag{1.7}$$

where Z_0 is the reference impedance. In general, the reference impedance of the VNA is real and equal to $Z_0 = 50\ \Omega$.

Again, the time variant behavior is investigated exploiting the zero-span mode of the VNA. Thus, the load impedance reads $Z(t, f)$.

1.4 PLC Noise Measurements

In PLC, the knowledge of the interferences within the grid is fundamental for the evaluation of the achievable performance in terms of potential data transmission rate and for the design of the front-end of the PLC devices. Furthermore, the analysis of the noise sources provides a clear indication of the devices that should kept far from the PLC devices.

In the following, we describe the approaches to perform background noise, impulsive noise and noise at the source measurements.

1.4.1 Background Noise Measurements

Typically, the PLC background noise is modeled as stationary additive colored Gaussian noise, with zero mean. Therefore, this contribute is completely described by its power spectral density (PSD). We show the setup in Fig. 1.6. The PSD of the noise is obtainable either using a spectrum analyzer (SA), or a DSO. Again, a coupler must be used to protect

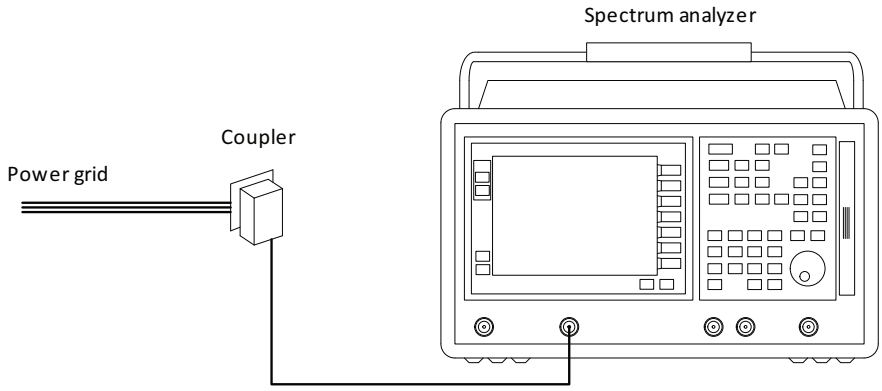

Figure 1.6: PLC background measurements approach.

the measurement equipment. The knowledge of how the coupler affects the acquisition and the noise floor of the instrument used for measurements are fundamental. This to distinguish the real contribution of the PLC noise from the contribution due to the coupler and the limits of the instrument. Firstly, an acquisition of noise samples when the coupler is disconnected from the power grid must be performed. If the noise measure is performed using a DSO, the noise PSD is computed via the periodogram of the noise samples. In the following, we refer to this acquisition as "floor PSD". The "floor PSD" must be compared with the PSD obtained from the noise measure. This to limit the frequency range to the range where the measured PSD is greater than the "floor PSD". In fact, when the measured PSD does not exceed the "floor PSD", it means that we are not acquiring the effective PSD of the PLC noise (cf. Fig. 1.7).

Therefore, the effect of the coupler is removed by subtracting (in dB scale) its frequency response to the effective PSD of the PLC noise.

If the noise acquisitions are performed using a DSO, the instrument must be auto-triggered, i.e., the instrument is not triggered by a threshold voltage. This to obtain randomly the noise acquisitions. The sampling rate, the time span and the memory depth of the DSO are fixed according to the desired frequency range and resolution.

1.4.2 Impulsive Noise Measurements

The objective is to obtain the statistics of the amplitude, the duration and the interarrival time of the bursts of impulsive noise. The setup is similar to that depicted in Fig. 1.6, except for the SA. In fact, due to the nature of the impulsive noise, the acquisitions can be performed only in the time domain, using a DSO. Now, the threshold voltage of the instrument is of key importance. The threshold voltage of the DSO must be set to an higher value w.r.t. the standard deviation of the background noise component. Therefore, the DSO is triggered in the normal mode, which enables the instrument to perform an acquisition only if the trigger event occurs. The sampling rate is fixed according to the bandwidth of

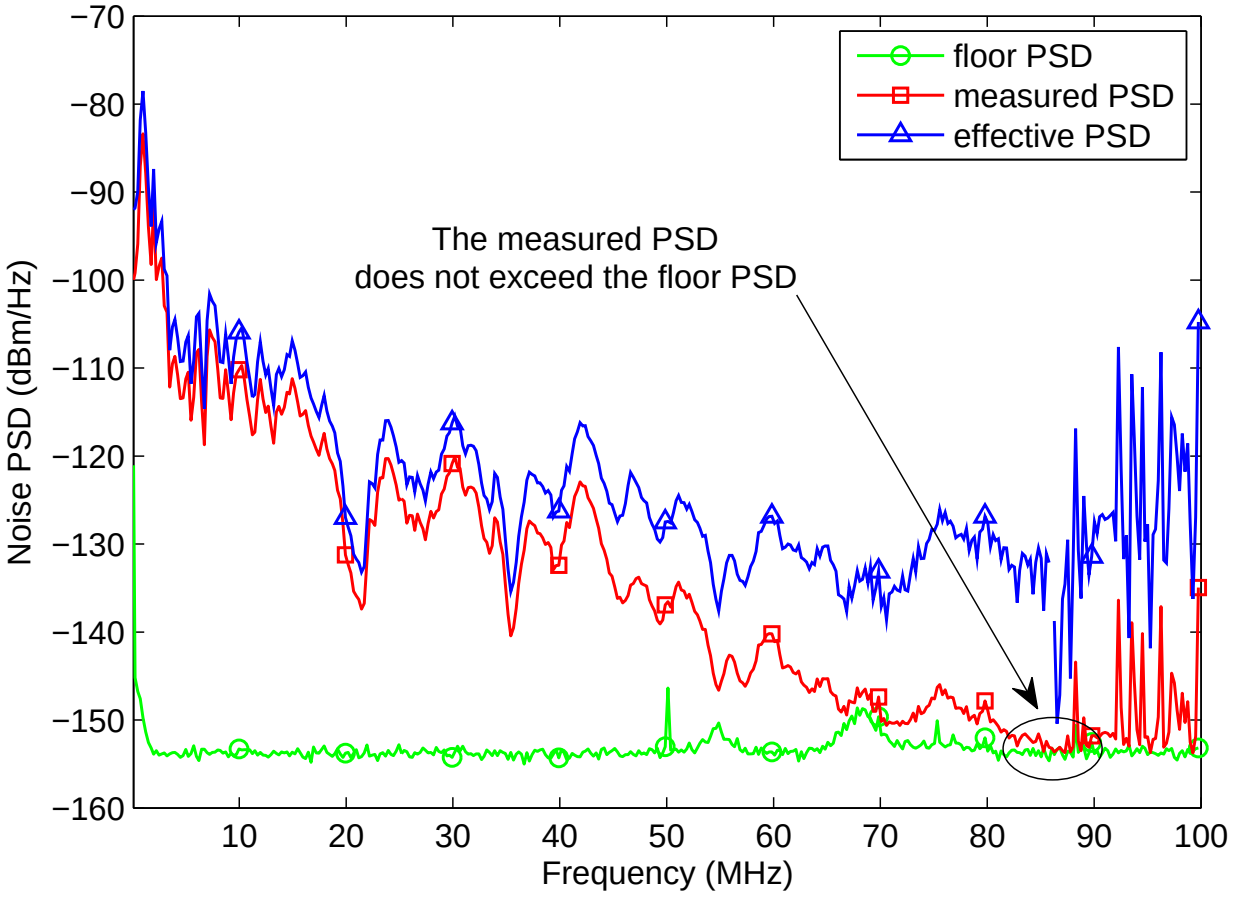

Figure 1.7: PLC background noise measurements approach. Explanation of Section 1.4.1.

interest while the memory depth of the DSO is set in order to acquire the longest time span.

1.4.3 Noise at the Source Measurements

The noise at the source measurements provide a full characterization of the loads in terms of the noise components that they inject into the network. As for the load impedance measurement setup, we refer to the in-home scenario. In fact, the electrical appliances are the main sources of noise in the in-home PLC. They contribute with both background noise and impulsive noise components. In Fig. 1.8, we depict the noise at the source measurement setup. Basically, the background noise and impulsive noise setups mentioned above are deployed, using a DSO in combination with a power line filter (PLF). The DSO is connected closed to the noise source, i.e., in order to acquire the maximum amplitude of the noise waveform. The PLF suppresses the noise incoming from the power grid. Thus, the DSO only acquires the contribute of noise generated by the load under test.

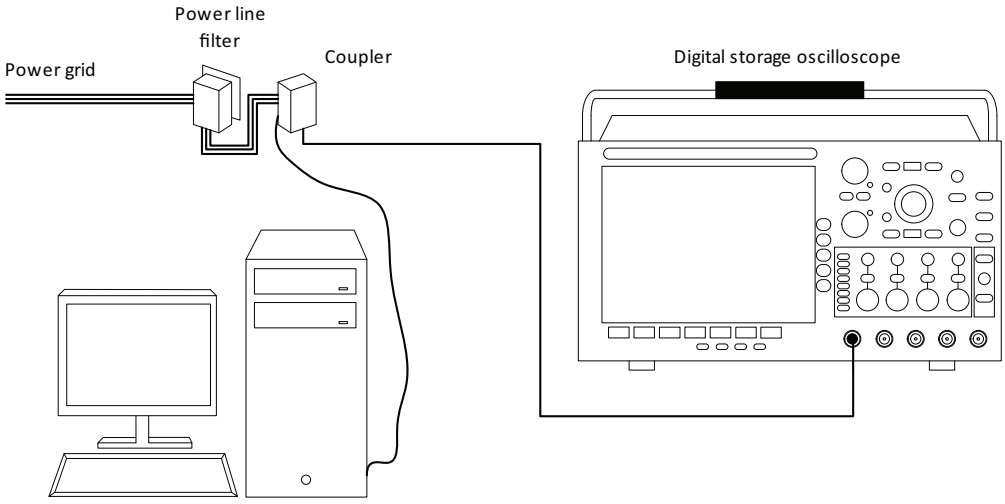

Figure 1.8: PLC noise at the source setup.

Chapter 2

Outdoor and Industrial PLC

In this chapter, we summarize the results of the experimental measurement campaign that we have carried out in the distribution network and protection laboratory (D-NAP) of the University of Strathclyde, Glasgow, UK. The D-NAP is a fully-customizable three-phase microgrid with multiple loads and generators and it can resemble either an O-LV power distribution network, or an industrial or marine power system.

The purpose of the experimental campaign has been to deeply investigate the feasibility of PLC solutions within the microgrid, in order to study the possibility to migrate to advanced remote control and monitoring SG applications in the outdoor and industrial scenarios.

2.1 Introduction

From a telecommunication point of view, the outdoor and industrial scenarios are similar. In both cases, there is a need to remotely command and control the various entities that are part of the power distribution grid at the generation, transmission (distribution) and consumption level. In recent years we have assisted to an increased interest toward the development of advanced technologies that allow bidirectional, reliable, short and long distance communications in such harsh environments. In this context, PLC is a suited technology.

For the design of the new generation of PLC devices, it is very important to perform an in-depth analysis of the grid characteristics in terms of propagation channel and disturbances [11–17]. This will allow for the understanding of the PLC channel properties, and consequently the analysis of the achievable performance and the design of transmission methods [18] that can overcome the attenuation, the frequency selectivity due to impedances mismatches and the noise sources that make the power line link a hostile media for communications.

In the literature, several papers focus on the potential of the PLC technology within the industrial environment. In [19], the special needs and requirements are considered, in comparison with those for other types of PLC application. In [20], the authors investigate the possibility to control and monitor an industrial motor through the feeder cable between

the motor itself and the inverter that controls it. Firstly, they used existing Home Plug PLC modems. They demonstrate that PLC modems developed for domestic applications may not be suitable for data transmission over feeder cables due to disturbances introduced by the inverter. Thus, they propose a PLC modem with convenient characteristics that fit for the industrial environment. Another paper that addresses the use of motor power cables for signaling is [21]. In [22] and [23], the impact of the noise in the industrial scenario (both in terms of impulsive and background components) is investigated. In [22], the analysis is in the frequency range below 2 MHz. In [23], the authors characterize and analyze the noise both in the time and frequency domain (up to 50 MHz), for three different configurations of inverter/motor on a test network.

In this respect, we have performed an experimental measurement campaign in an artificial distribution network that emulates the O-LV and the industrial scenario, i.e., the D-NAP of the University of Strathclyde, Glasgow, UK. Herein, we investigate the channel frequency response with particular emphasis on the effect of loads and the possibility of transmitting and receiving on different phases. We show the results for both the NB and BB frequency range. Thus, we address the analysis of the background noise within the NB frequency range, i.e., where we have experienced the highest noise levels mainly due to the presence of the loads. Furthermore, in the NB frequency range, we study the line impedance and the time variance of the channel. Finally, we investigate the performance of commercial devices. The purpose is twofold. On one hand, we aim to investigate the performance of the available commercial modems in scenarios for which they have not been explicitly designed, namely, the industrial and the O-LV. On the other hand, we aim to study whether the use of commercial devices is interesting for the facility by itself, namely, to demonstrate the possibility of substituting or providing redundancy to the today systems based on dedicated cables needed for digital communications among the different elements of the microgrid. We provide the measured data rate, and we compare it to the theoretical channel capacity. Furthermore, we investigate the performance of BB PLC, i.e., we report the results of the experimental test of HomePlug compliant devices in the D-NAP network.

The chapter is organized as follows. In Section 2.2 and 2.3, we describe the D-NAP network and the measurement setup, respectively. In Section 2.4, we describe the PLC channel, the line impedance and the noise from the results of the measurements. Then, in Section 2.5, we report the performance of the commercial devices. Finally, Section 2.6 summarizes the main findings.

2.2 Network Description

In Fig. 2.1, we show a schematic diagram of the D-NAP microgrid. Basically, it is a three-phase low voltage network that is fed by a dedicated medium-voltage to low-voltage (MV/LV) distribution transformer. The transformer is a 500 kVA transformer in a delta-star

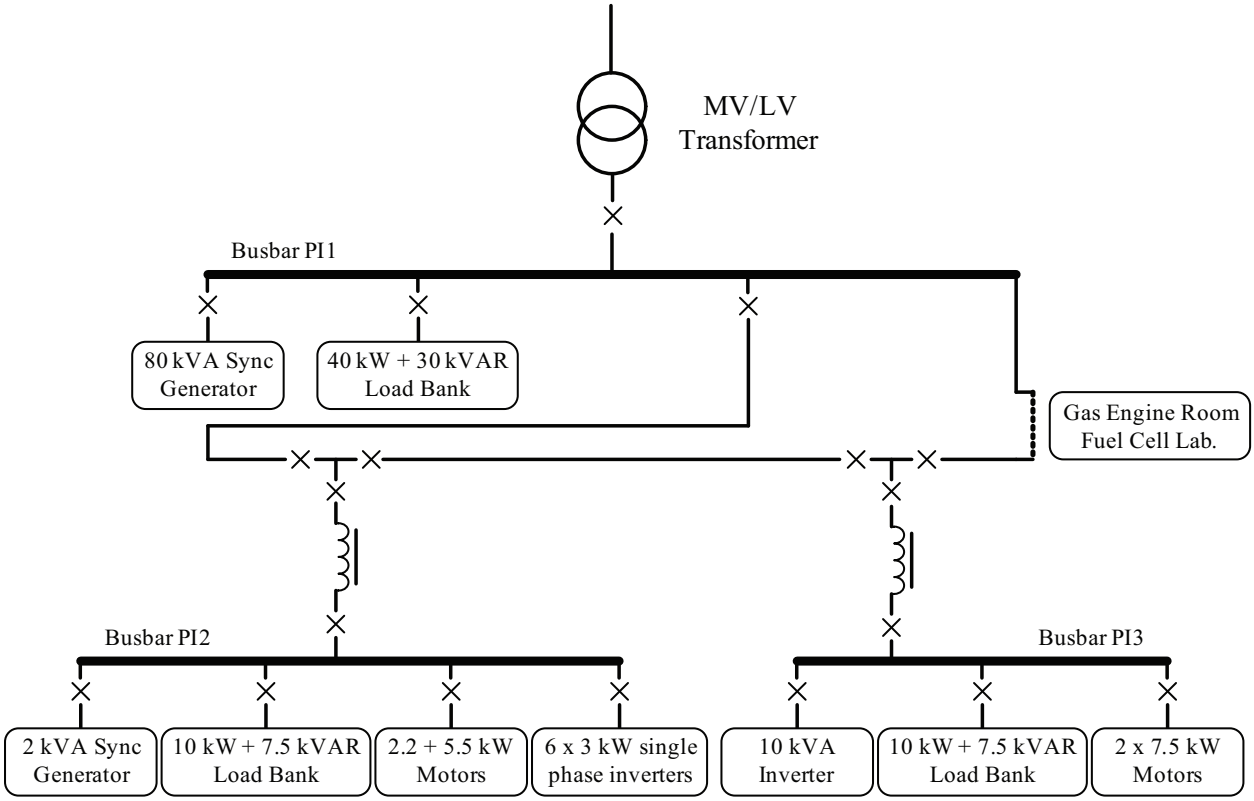

Figure 2.1: Schematic diagram of the D-NAP.

configuration, and it is connected to the 11 kV network that feeds the entire campus of the University of Strathclyde. On the low voltage side, the neutral conductor is provided, and it is connected to the center of the star structure of the transformer windings.

The D-NAP is ring-shaped, and it consists of three independent power islands (PIs) that can work separately or brought together as a single system. We follow the notation of Fig. 2.1. We denote the power island connected to the MV/LV transformer with PI1, and we refer to the other two power islands as PI2 and PI3. The PIs can be isolated or interconnected via remote-controlled switches, and the switches can be either normally open or close, as in the UK power distribution scenario. Furthermore, the D-NAP can be connected to the external gas engine room, and the fuel cell laboratory.

The power cables are short if compared to the ones of a typical O-LV scenario. In this respect, concentrated-parameter elements, i.e., resistances and inductances, simulate the effect of long power cables between the PIs. Furthermore, they can be used to simulate the presence of distribution-level transformers. Physically, they are placed on the power cables toward PI2 and PI3, but they can be bypassed if their contribution is not required.

The PIs are equipped with a busbar where several synchronous generators, inverters, and loads are connected to. The synchronous generators are two, and they are representative of high-power sources with variable production. The most powerful generator is a 80 kVA synchronous generator, and it is connected to the busbar of PI1. Before being installed in

the D-NAP network, the generator was deployed to supply electricity in a submarine. The second synchronous generator is similar to the previous one, but it is smaller, and it can produce up to 2 kVA. It is connected to the busbar of PI2. DC power motors provide the mechanical power to the synchronous generators. The motors are fed by AC/DC converters that are supplied externally from the D-NAP network. The motors are remotely controlled, and they can simulate a variable energy production.

Two types of inverters are connected to the microgrid. The first is a 10 kVA three-phase inverter that can simulate either a fuel cell resource or the aggregate effect of multiple distributed power plants. The behavior is determined by the DC power supply unit that feeds the inverter. The DC unit is programmable, and it can be remotely controlled. Further, it is supplied externally from the network. The inverter is connected to the busbar of PI3. The second inverter unit is representative of a wind power plant. Basically, it consists of a bank of single-phase inverters. On each phase, the bank comprises two 3 kW single phase inverters that are connected between the phase and the neutral. We note that the power output of a single inverter equals the consumption of a typical residential user. The inverters are fed by DC units. The DC units allow for the simulation of a variable energy production that corresponds to a specific wind intensity profile. The inverters are individually controllable, and one independent DC unit is provided for each inverter. The units are supplied externally from the network, while the inverter bank is connected to the busbar of PI2.

Now we describe the passive loads. The facility is equipped with 4 induction motors that are representative of typical industrial machines. Two are connected to the busbar in PI2 and the remaining two are connected to the busbar of PI3. The absorption power of the motors in PI2 is 2.2 and 5.5 kW. In PI3, the two motors are identical, and their absorption power is 7.5 kW. The motors are equipped with an inertia, and their torque is remotely controllable.

To simulate the impact of residential users, two banks of variable resistive and inductive loads are present. One is connected to the busbar of PI2, and the other one is connected to the busbar in PI3. We refer to them as static load banks. The static load bank consists of 64 groups of inductances and resistances that can be individually connected to the network in order to increase the absorption power of the bank. Therefore, a 64-step load is given. The maximum absorption power of the bank is 10 kW plus 7.5 kVAR.

The D-NAP is fully remote-controllable. A communication infrastructure and a software-based management application allow the user to control the facility and to capture data from the sensors. The control system is referred to as real time simulator (RTS). The RTS infrastructure consists of a large amount of dedicated cables that connect the switches, the appliances and the sensors to the control station. In this respect, we note that PLC may be suitable to substitute or even to provide redundancy to the existent dedicated wireline.

2.3 Measurement Setup

We aim to study the impact of the industrial loads and generators on the PLC transmission medium. To do so, we have configured the network as follows. We have interconnected the PIs together as a single system, and we have isolated the microgrid from the gas engine room and the fuel cell laboratory. The final layout is a tree-like structure. We have bypassed the concentrated-parameter elements on the power cables toward PI2 and PI3 because they are not realistic in the higher frequency range. Initially, we have studied the network when no loads were connected. Then, we have connected the appliances one by one, and we have studied their impact on the channel frequency response, the line impedance, and the noise.

In Table 2.1, we collect the information about the configurations. In the first column, we describe the configuration, namely, the load that we have connected to the network. In the second column, we describe the access port where we have connected the receiver. We have connected the receiver on the same busbar that feeds the load. We have discarded the synchronous generators because their DC supply units introduce high spikes of noise into the microgrid. The injection is due to coupling between the D-NAP network and the DC circuit, and this behavior is not common in real-life networks. Further, we have limited the analysis to the static load bank in PI3, and to one motor of 7.5 kW because we assume the other banks and the other motor of the same power to perform similarly.

We have placed the access points in barycentric positions inside the power islands PI2 and PI3. Furthermore, we have focused on single-phase PLC. To this aim, we have created single-phase access points that enable signaling between each of the three phases (denoted with R, S, and T) and the neutral conductor (N).

We have performed measurements both in the time and the frequency domain (see Sections 1.2, 1.3 and 1.4). To protect the equipment from the mains, we have designed and built the PLC couplers. We have deployed NB couplers for measurements in the 30 kHz - 2 MHz frequency range, and BB couplers for the measurements in the 2-100 MHz frequency range. We note that 30 kHz is lower than the start signaling frequency of most of commercial PLC devices.

2.4 Measurement Results

We aim to study the impact of the industrial loads in the NB frequency range, i.e., the range of frequencies dedicated to communications for command and control applications [2–6]. In this section, we present the results of the measurement activity, i.e., we investigate the channel frequency response, the line impedance and the background noise.

Table 2.1: List of the considered loads.

Description	Receiver PI	Configuration Index
All loads switched off	PI2	0
All loads switched off	PI3	1
7.5 kW motor	PI3	2
Static load bank	PI3	3
10 kVA 3-phase inverter	PI3	4
2.2 kW motor	PI2	5
5.5 kW motor	PI2	6
Single-phase inverters	PI2	7

2.4.1 Channel Frequency Response and Line Impedance

As mentioned in Section 1.1.1, we model the D-NAP between the access points of busbars PI2 and PI3 as a two-port network, and we characterize the two-port network in terms of its CTF and line impedance. Furthermore, we model the PLC channel as a LTI system. As it will be clarified in Section 2.4.2, the LTI assumption is valid in the case of the D-NAP network.

We limit the results to the CTF between PI3 and PI2, and we study the channel when the transmitter and the receiver are connected to either the same phase and the neutral wire, or different phases and the neutral wire. We refer to the first case as direct channel, or single-phase channel, and to the second case as coupled channel, or cross-phase channel. To include the single/cross phase information, and the configuration of the load that we consider, we use the notation $H^{(k)}_{(TX,RX)}(f)$ to indicate the CTF, where $TX, RX \in \{RN, SN, TN\}$, and $k = 0, 1, \ldots, 7$. Basically, the subscript (TX, RX) refers to the phases (and to the neutral wire) to which the transmitter and the receiver are connected to, and the superscript k is the configuration index. Again, in Table 2.1, we report the configuration, the busbar where we connect the receiver port, and the correspondent configuration index. For $k > 1$, we assume the receiver to be connected on the same busbar that feeds the load.

We focus on the NB frequency range, and we investigate three features of the channel frequency response, namely, the interchangeability of the phases, the difference between the direct and the coupled channel, and the impact of the loads. Firstly, we focus on the interchangeability. The network is a three-phase network. Therefore, between two access points, three direct channels are given. Now, the phases are interchangeable if the channel frequency response is not a function of the specific phase where the modems are connected to. We limit the study to the path loss (PL) that is defined as $PL(f) = |H(f)|^2$ where $H(f) = H^{(k)}_{(TX,RX)}(f)$ is the CTF mentioned above. We compute its version in dB as $PL_{|dB}(f) = 10 \log_{10}(PL(f))$.

As an example, in Fig. 2.2-(a), we show the single-phase path losses of configuration

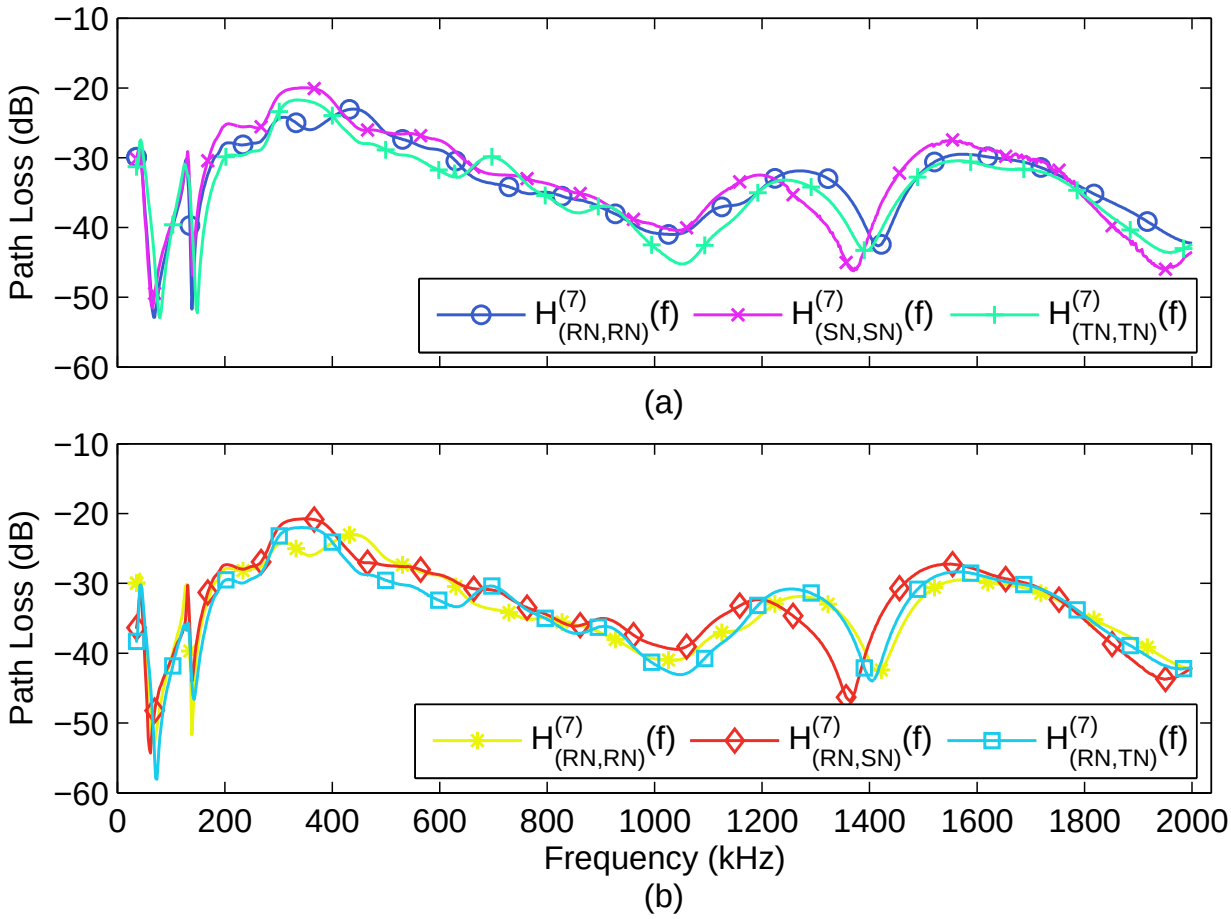

Figure 2.2: NB channel frequency responses (path losses) in configuration $k = 7$. (a): Comparison between direct channel frequency responses. (b): Comparison between the coupled channels and the direct channel of phase R.

$k = 7$. The channels are almost identical and thus the phases are interchangeable with good approximation. Similar results were obtained with different configurations. Therefore, in the NB frequency range, we experience the same channel when we signal on phase R, S or T.

We aim to study the feasibility of cross-phase communications. In a three phase circuit, it may happen that the transmitter and the receiver are connected to different phases. The signal propagation is ensured by coupling because the wires are closely arranged inside the same dielectric cap. Typically, coupling is more pronounced in the higher frequency range. In Fig. 2.2-(b), we compare the direct channel (RN, RN) to the coupled channels (RN, SN) and (RN, TN) in configuration $k = 7$. Interestingly, cross-phase communications are possible, and the coupled channels are quite similar to the direct one. However, the coupled channels exhibit a higher attenuation, namely, of up to 10 dB, in the range of frequencies below 100 kHz. NB commercial devices operate in the Cenelec A band, namely, below 100 kHz, and thus they face on higher attenuation when they signal on coupled channels.

To study the impact of the loads on the channel frequency response, we focus on the

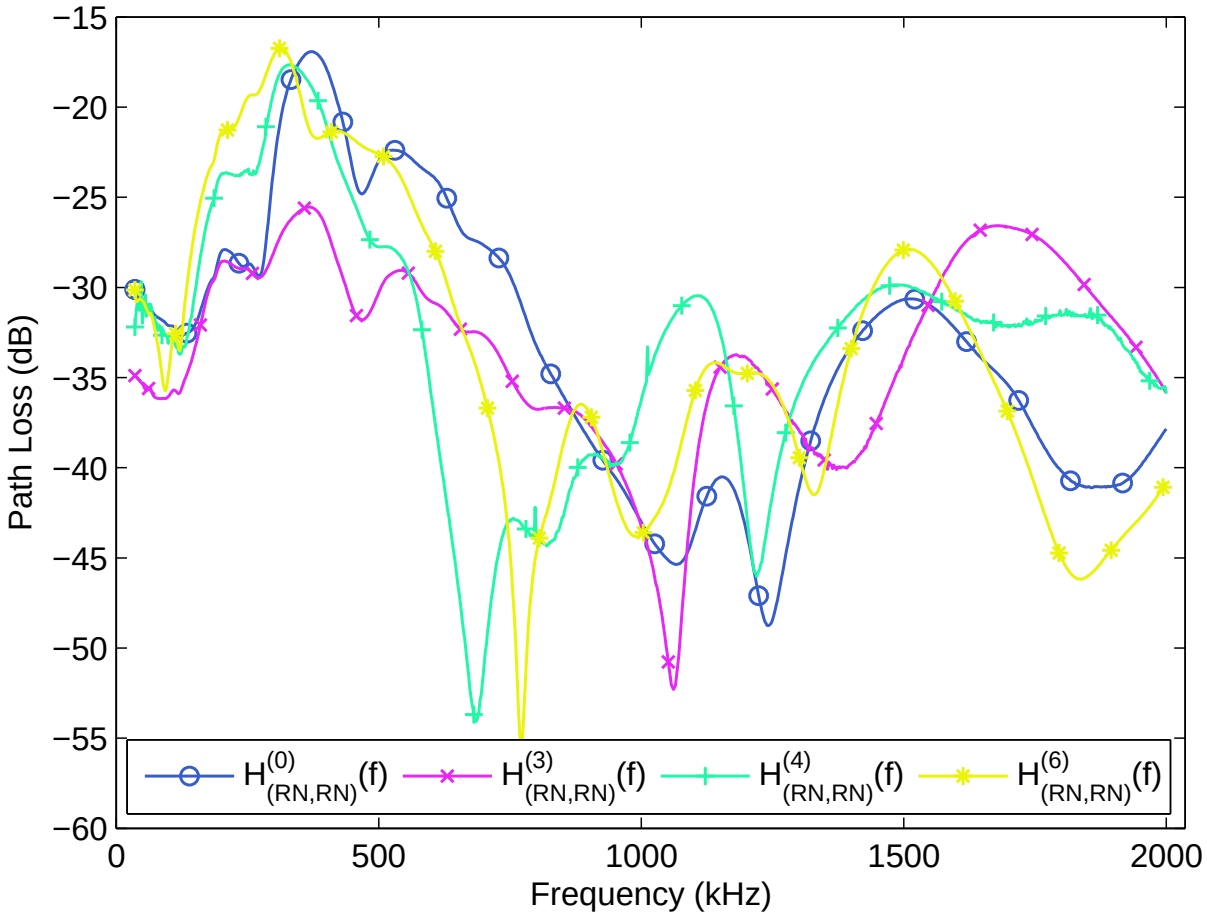

Figure 2.3: Direct channel frequency responses for different load configurations.

subset of cases $k = 0, 3, 4, 6$. In Fig. 2.3, we show the results. We focus on the direct channel (RN, RN). We experience variations in the channel frequency profile when different loads are connected. In particular, we note that the presence of loads may turn into less attenuated channel responses.

Now, we focus on the line impedance. We investigate the variations on the line impedance that are due to different load configurations. To this aim, we introduce the extended notation $Z^{(k)}(f)$, where $k = 0, 1, \ldots, 7$ is the configuration index. We limit the study to the configurations and the ports of Table 2.1, and we focus on the line impedance of one phase, namely, phase R. When no loads are connected, we show the line impedance of both the ports. For $k > 1$, we focus on one appliance and we show the line impedance of the port that is the closest to the appliance, namely, the receiver port of Table 2.1. We remark that we do not show the load impedance. In fact, the load impedance is not equal to the line impedance because the latter is given by the parallel of the load with the rest of the network.

In Fig. 2.4, we plot the real and the imaginary part of the line impedance for different load configurations. Firstly, we consider the line impedance of both the ports when no loads are connected. As shown in Fig. 2.4, the ports exhibit the same impedance in the range of

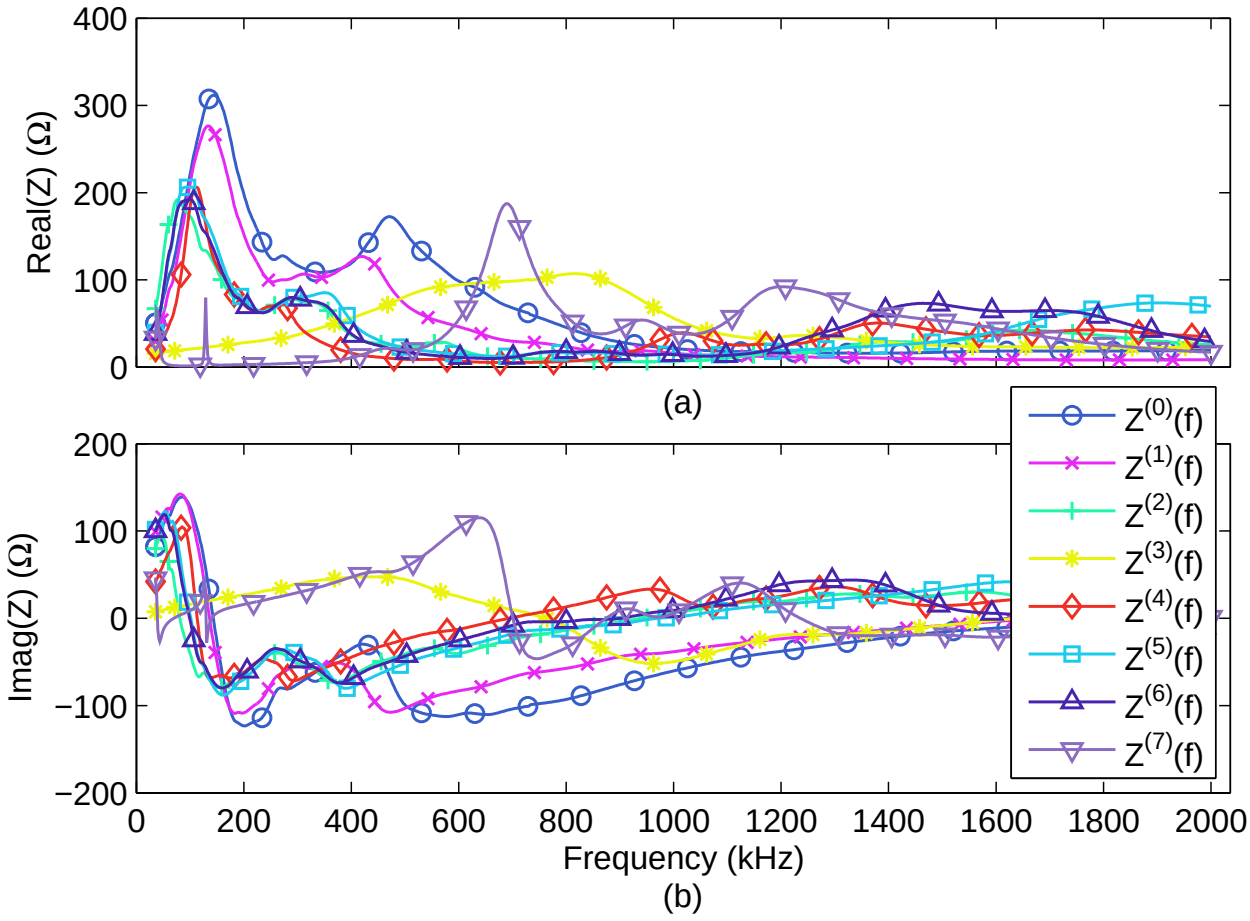

Figure 2.4: NB line impedance for different load configurations.

frequencies below 100 kHz. Above 100 kHz, the profiles are similar, though the magnitude is different. Then, we study the effect of the loads, and we point out two interesting results. First, the impedance of the motors is not a function of the absorption power of the appliance operating mode. In $k = 2$, we connect the 7.5 kW motor to the busbar PI3. In $k = 5$ and $k = 6$, we connect the 2.2 and the 5.5 kW motor to busbar PI2, respectively. The line impedance of the three configurations is similar below 500 kHz, regardless the absorption power and the access port. Second, the load bank and the single-phase inverters exhibit an inductive behavior below 500 kHz that forces the real part of the line impedance to very low values. Strictly, we note that the minimum value of the real part of the line impedance for $k = 7$ is equal to 1.2 Ω.

Now, we study the mean and the minimum value of the access impedance in different transmission bands. We focus on Cenelec bands A, B, and C. For each band, we compute

Table 2.2: Mean and minimum values of the real line impedance.

Cenelec Band	$B_{1,b}$ (kHz)	$B_{2,b}$ (kHz)	$\overline{Z}(b)$ (Ω)	$Z_{min}(b)$ (Ω)
A	35.938[1]	95	87.4	≈ 1 (f=89.3 kHz; k=7)
B	95	125	154.8	≈ 1 (f=97.2 kHz; k=7)
C	125	140	137.5	≈ 5 (f=136.8 kHz; k=7)

the mean and the minimum value of the real part of the line impedance as

$$\overline{Z}(b) = \frac{1}{B_{2,b} - B_{1,b}} \int_{B_{1,b}}^{B_{2,b}} \frac{1}{8} \sum_{k=0}^{7} \mathrm{Re}\left\{ Z^{(k)}(f) \right\} df, \tag{2.1}$$

$$Z_{min}(b) = \min_{\substack{k=0,\ldots,7, \\ B_{1,b} \leq f \leq B_{2,b}}} \left\{ \mathrm{Re}\left\{ Z^{(k)}(f) \right\} \right\}, \tag{2.2}$$

respectively. In (2.1)-(2.2), we denote with $b \in \{A, B, C\}$, $B_{1,b}$, and $B_{2,b}$, the Cenelec band, and the start and the stop frequency of the Cenelec band b. In Table 2.2, we report the values of $B_{1,b}$[1] and $B_{2,b}$, and we show the results. We note that the mean value is equal to 87 Ω in the Cenelec A and greater than 150 Ω in the other two Cenelec bands, though the minimum value is close to zero in all the bands. In all cases, the low values are due to the presence of the the single-phase inverters, i.e., $k = 7$.

2.4.2 Time Variance

Now, we investigate the time variance of the PLC channel in the O-LV and industrial or marine scenarios emulated by the D-NAP network due to the non-linearities of the loads. In fact, the presence of loads whose behavior is not linear, determined by the 50 Hz sinusoidal power waveform, implies that power line channel characteristics are variant in time. In [24], it has been demonstrated that the cause of this time variant behavior is simply due to the front-end circuitry of the power switching supplies of the appliances connected to the grid. The variations are generally encountered at the peaks of the magnitude of the mains waveform, thus in a single-phase system two variations of the channel can be found in 20 ms.

To this aim, we have synchronized the VNA to the mains cycle, and we have performed time-frequency acquisitions of the scattering parameters of the network. In Fig. 2.5, we report the frequency response of the most time variant channel that we have found, i.e., the direct channel (RN, RN) in configuration $k = 2$, i.e., when the network is fed and only the 10 kW/7.5 kVAR controllable static load bank of the PI3 is switched on. Note that the 0 ms time-reference of the figure corresponds to the zero-crossing of the mains signal on phase

[1]For the Cenelec A, we report the value of the start signaling frequency of commercial PLC devices.

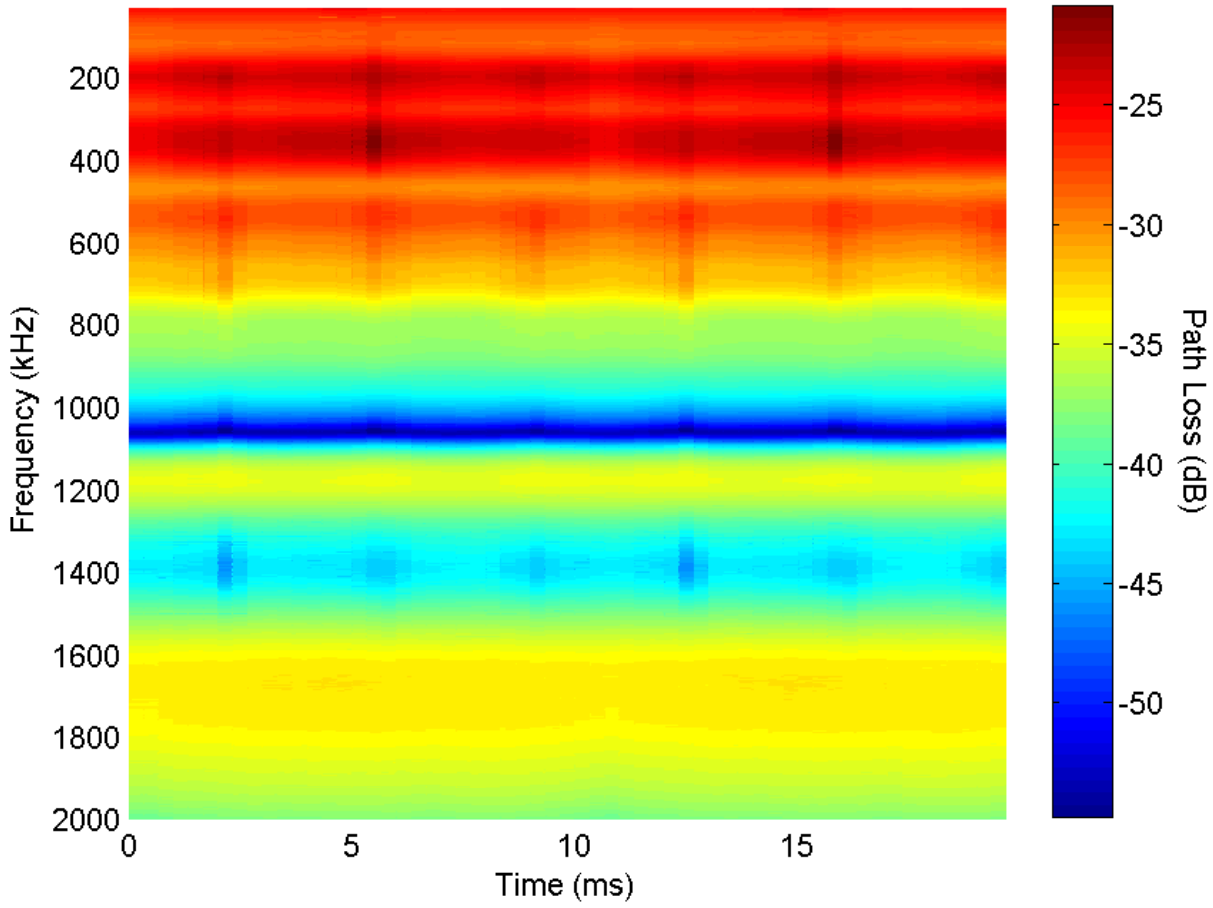

Figure 2.5: Time variant frequency response of one single-phase channel when only the 10 kW/7.5 kVAR controllable static load bank is switched on. It is possible to notice six variations at the peaks of the magnitude of the three mains waveforms of the three-phase system.

R. It is possible to notice six deviations w.r.t. the channel state at the time instant 0 ms. The amount of variation is more pronounced (4 dB) at 5 and 15 ms, i.e., at the peaks of the magnitude of the mains signal as mentioned above. Other smaller variations (2 dB) can be found and are amenable to the cross-talk effects of the power switching of the mains in the other two phases, $2/3\pi$ and $4/3\pi$ out of phase w.r.t. the phase R.

Nevertheless, the amount of variations is so small that the power line channel of the D-NAP microgrid can be considered time invariant and no channel adaptation is required.

2.4.3 Background Noise

From the measures, we characterize the PSD of the background noise. We have performed the noise measures in the time domain with a DSO in combination with extension cables and NB couplers. Measurements are reliable below 2 MHz. In the higher frequency range, where the noise PSD is low, the measurements approach the noise floor level of the DSO.

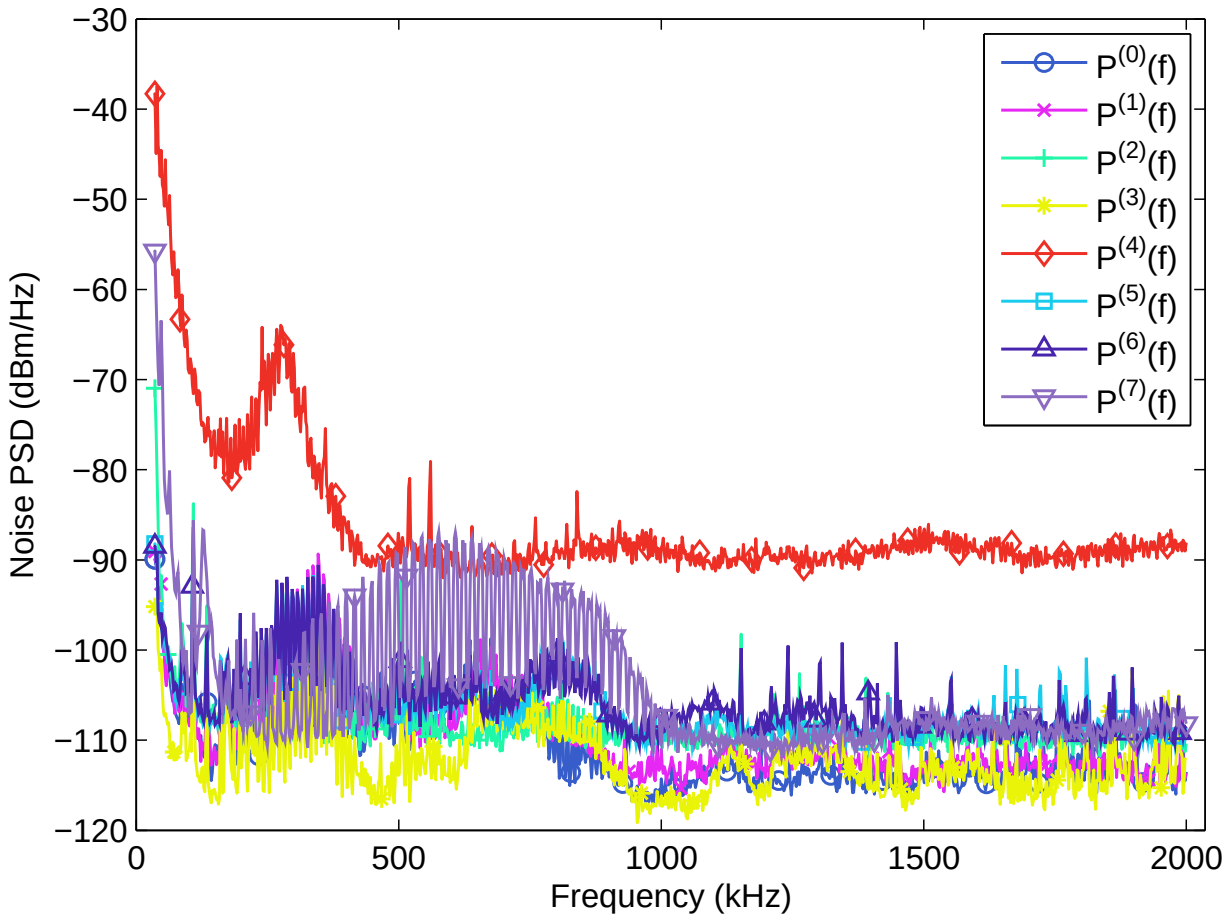

Figure 2.6: Background noise PSD experienced at the ports 1 and 2.

In the following, we use a notation that is similar to the one that we have introduced for the line impedance. Basically, we denote with $P^{(k)}(f)$ the measured noise PSD of the configuration and the receiver port identified by index k. Again, we refer to Table 2.1 for the configuration details. We focus on one phase, and we provide the noise of the port that is the closest to the load. For $k > 1$, the measures do not address the pure noise of the appliance. In fact, the measure is the result of the superposition of the noise when no appliances are connected and the noise due to the appliance.

We focus on the PSD of the noise. To this aim, we compute the periodogram of the measured noise samples, and, in Fig. 2.6, we show the results. As expected, when $k = 0, 1$, the noise exhibits the lowest PSD values. Concerning the loads, we highlight that the inverters are the noisiest devices. In detail, we distinguish three distinct PSD behaviors. Regarding the worst case, the noisiest appliance is the 10 kVA three-phase inverter, i.e., the configuration $k = 4$. The appliance increases the network noise of port PI3 of about 20 dB on average. The second noise profile is associated to the three single phase inverters, namely, configuration $k = 7$. The appliance introduces spike harmonics that are multiple of the fundamental frequency of 16 kHz. In all other configurations, namely, 6 cases over

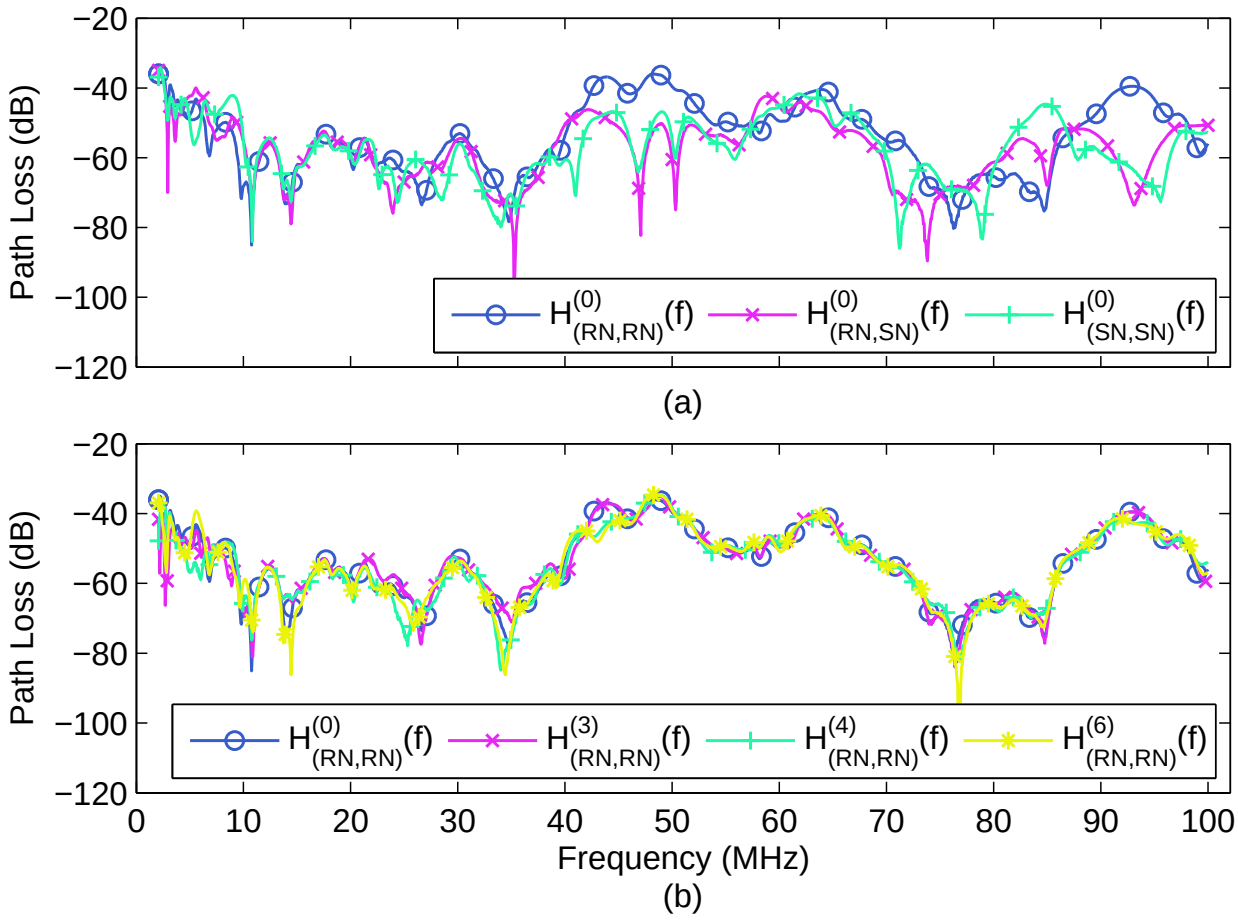

Figure 2.7: (a): BB channel frequency responses (path losses) for $k = 0$. Direct and coupled channels are shown. (b): Direct channels for different load configurations.

8 measures, the noise PSD exhibits a similar behavior that is close to the one of the cases $k = 0, 1$. We fit the measures with the following model

$$P(f) = \alpha f^{\beta} + \gamma \quad [dBm/Hz]. \tag{2.3}$$

For the three representative behaviors that we have described above, the best fit is as follows. For case $k = 4$, $\{\alpha, \beta, \gamma\}$=$\{-8.297, 0.09596, -73.36\}$.
For case $k = 7$, $\{\alpha, \beta, \gamma\}$=$\{8.531e6, -1.163, -106.5\}$. Finally, for all the other cases, we fit the average profile (averaged among the noise measures of cases $k = 0, 1, 2, 5, 6$) to obtain $\{\alpha, \beta, \gamma\}$=$\{2980, -0.4942, -74.23\}$.

When no inverters are present, we propose to model the noise of the industrial scenario in the NB frequency range according to (2.3) and the latter set of parameters.

2.4.4 BB Frequency Range

We aim to evaluate the possibility of using BB PLC in the O-LV scenario. In this respect, we provide a first insight of the BB PLC channel. We overview the channel characteristics that we have presented for the NB scenario. In the BB frequency range, the interchangeability holds true, though the channels exhibit slight differences. In Fig. 2.7-(a), we compare direct and coupled channels. All the results refer to configuration $k = 0$. Concerning the direct channels, we note that above 5 MHz, the profiles show deviations that are due to small differences in the length of the connection cables or in the geometry of the circuit. Since, these deviations are negligible for communication purposes, we conclude that the channels are interchangeable. Furthermore, we note that coupled and direct channels are impaired by similar fading and attenuation effects. Hence, BB PLC perform similarly if the transmitter and the receiver are connected either on the same phase or on different phases. It follows that BB PLC are suitable for communications in multi-phase networks where not all the three phases are available on each access point. Similar results for the naval scenario will be presented in Chapter 5.

We further investigate the effect of loads. We measure the PLC channel between PI3 and PI2 for the configurations $k = 0, 3, 4, 6$. We show the results in Fig. 2.7-(b). As can be noted, the profiles are quite similar. It can be explained as follows. The loads are connected to the D-NAP through a remotely-controlled switch. When the switch is left open, the contacts are close enough to allow coupling. Furthermore, coupling is enforced by the proximity of the cables on both the sides of the switch. It follows that the switches do not block the signal in the higher frequency range. Thus, the channel is not a function of the load configuration.

2.5 Test of Commercial Devices

We have tested several commercial PLC devices in the D-NAP network. This study is motivated by the following reasons. First, we aim to address the performance of the commercial devices in the industrial scenario. In this respect, the facility is representative because it gathers several motors and resistive loads in a small area. Second, we aim to investigate the impact of the inverters on PLC. In real life scenarios, the distributed generators are connected to the O-LV network through the inverters. The inverters introduce high levels of background noise, as shown in Section 2.4.3.

We have connected the communication devices close to the inverters of the facility, i.e., where we have experienced the highest levels of background noise. It follows that the D-NAP network is representative of the worst case scenario. Finally, the use of commercial PLC devices may be of some interest for the D-NAP network by itself. The network is fully remote-controllable and a large amount of dedicated cables have been deployed to interconnect the switches, the appliances and the sensors to the control station. PLC may

Table 2.3: OFDM system parameters for G3.

Parameter	Cenelec A	Cenelec B	Cenelec C
$1/T$ (kHz)	200	200	200
M	128	128	128
Cyclic prefix length (μs)	75	75	75
Cardinality of $\mathbb{K}_{on}$	36	16	7
Start frequency $f_{s,b}$ (kHz)	35.938	98.4375	128.125
Stop frequency (kHz)	90.625	121.875	137.500

Table 2.4: Experimental (Meas.) and theoretical (Theo.) data rates of G3-PLC.

	Cenelec A		Cenelec B		Cenelec C	
Config.	Meas. (kbps)	Theo. (kbps)	Meas. (kbps)	Theo. (kbps)	Meas. (kbps)	Theo. (kbps)
$k=0$	23.55	666.55	9.35	325.02	7.51	150.15
$k=1$	23.56	591.22	9.37	309.34	7.5	140.73
$k=2$	23.53	831.38	9.34	374.64	7.53	175.04
$k=3$	0	22.02	8.73	62.67	3.42	44.78

substitute the existent wirings, or it can provide a new communication channel that could be used to improve the reliability of the transmission and to increase the data rate.

Firstly, we have focused on NB PLC, and we have tested commercial devices that are based on the G3-PLC standard [2,4–6]. We have tested the G3-PLC modems in the Cenelec A, B, and C bands, and we have compared the experimental performance to the maximum attainable ones. From theory, the maximum achievable rate of an OFDM transmission that deploys CP reads as follows

$$C_b^{(k)} = \frac{1}{(M+\mu)T} \sum_{m=0}^{M-1} \log_2 \left(1 + \frac{|H_{11}^{(k)}(f_m)|^2 P_{tx}(f_m)}{P_w^{(k)}(f_m)} \right) \quad [bps], \tag{2.4}$$

where b, T, μ, M, $P_{tx}(f_m)$, and $P_w(f_m)$ are the index of the Cenelec band, the sampling factor, the number of CP samples, the number of active sub-carriers, and the PSD of the transmitted signal and the noise, respectively. Furthermore, we denote with $f_m = m/MT + f_{s,b}$ the frequency of the m-th subcarrier, where $f_{s,b}$ is the start transmission frequency in the band b and $b \in \{A, B, C\}$. To compute (2.4), we approximate $P_{tx}(f)$ as constant and equal to -30 dBm/Hz, we assume the transmitted signal to be normally distributed, and we model the noise as additive stationary coloured Gaussian noise. For all the other parameters in (2.4), we refer to Table 2.3.

In Table 2.4, we report the results. We consider several load configurations, namely $k = 0, 1, 2, 3$ and we focus on the direct channel (RN, RN). We provide average throughput

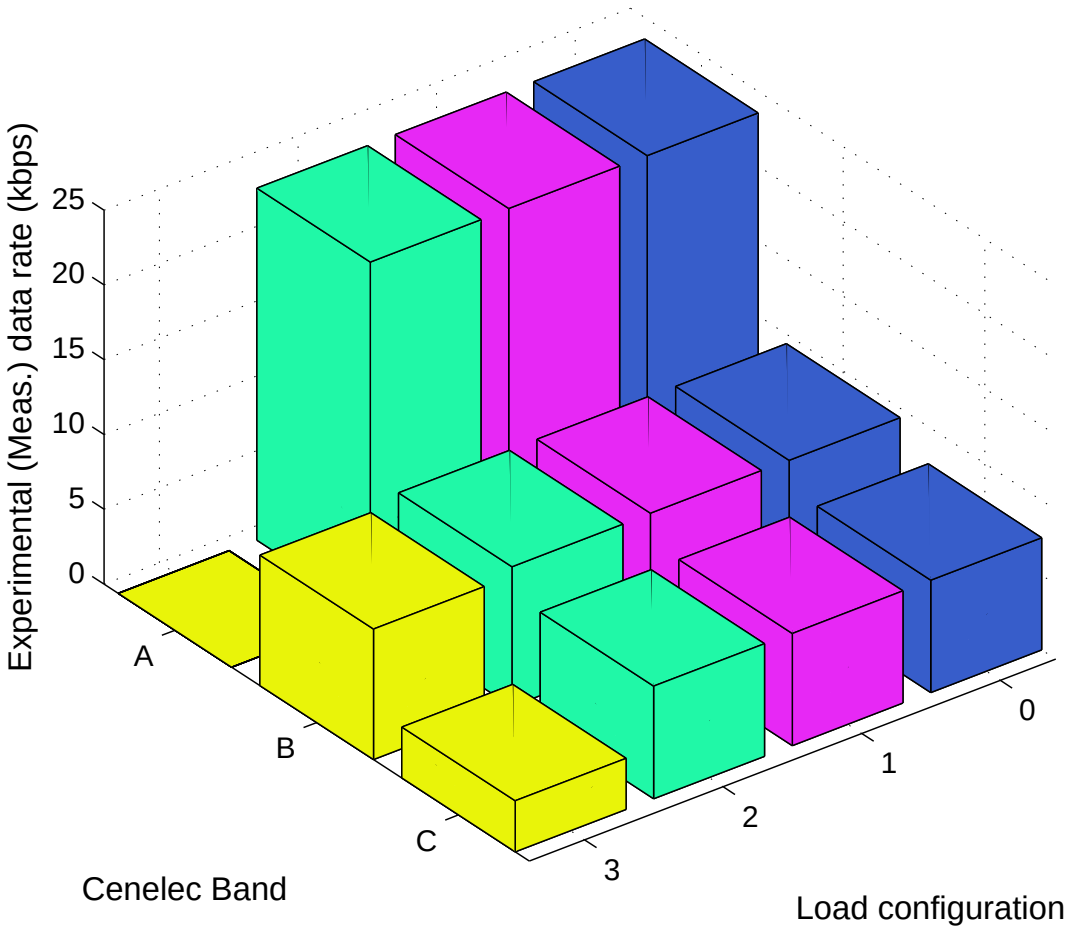

Figure 2.8: Experimental (Meas.) data rates of G3-PLC.

(over 20 seconds) that we have measured at the physical layer. As expected, the performance collapse for $k = 3$ because the 10 kVA 3-phase inverter increases the background noise of up to 20 dB in the NB frequency range (see Fig. 2.6). Furthermore, we note the large gap between the experimental data rates and the maximum achievable values. Thus, significant improvements can be still achieved by further optimizing the physical layer of the next generation of PLC devices.

2.5.1 BB PLC Test

As we have previously discussed, BB PLC were initially intended for the in-home scenario, where they allow for high-speed communications of up to 200 Mbps. In the industrial scenario, BB PLC are suitable because they exploit coupling to signal over coupled channels. Furthermore, BB PLC signal in the higher frequency range, and thus they experience lower levels of background noise w.r.t. NB PLC.

We have deployed commercial devices that are compliant with the Homeplug AV standard [7]. We have tested commercial devices by establishing a file transfer between two computers

through the D-NAP network. The PCs have been connected to busbar PI2 and PI3. On direct channels, the average data rate is 130 Mbps. Further, on the cross channel, the performance decreases by only 3 % in terms of data rate. This result validates the use of BB PLC for cross-phase PLC communications.

2.6 Main Findings

We have presented the results of the experimental measurement campaign that we have performed in the three-phase distribution network laboratory of the University of Strathclyde, Glasgow, UK. We have focused on the channel frequency response, the line impedance and the background noise. Furthermore, we have addressed both the NB and the BB frequency range.

Firstly, we have focused on the NB frequency range. From the analysis of the channel frequency response, we have found the followings. First, the phases are interchangeable because the channel frequency response seems to be not a function of the specific phase. Second, when the transmitter and the receiver are connected to different phases, NB PLC solutions are not suited due to the high attenuation of the channel in the lower frequency range. Third, the presence of loads may turn into less attenuated channels. Finally, the measured channels exhibit a low time-variation. Thus, we can model the NB CTF as time-invariant. From the analysis of the line impedance, we have pointed out the differences due to the loads, and the lowest and the mean impedance values that we have measured in the Cenelec bands A, B and C. Finally, from the analysis of the measured background noise, we have found that the inverters are responsible for the highest noise values and we have provided an analytical expression to model the highest, mean and lowest power spectral density profile.

In the BB frequency range, we have limited the study to the channel frequency response. We have found that the interchangeability of the phases holds true and, further, the channel frequency response is similar regardless the loads and the phase where transmitter and receiver are connected to.

Finally, we have tested commercial PLC devices that operate in the NB and BB frequency range. We have considered several configurations, and we have found that the presence of inverters close to the communication nodes compromises NB transmissions. Indeed, BB PLC ensure high speeds even for communications across phases. Therefore, BB PLC are a suitable candidate for PLC in the industrial scenario.

Chapter 3

Characterization of Load Impedances

The characterization of the load impedances in the home/office power grid is the topic of this chapter. We have deeply investigated the behavior in the time and frequency domain of a broad set of devices that we can find in a house or office.

This is motivated by the fact that the PLC medium is strongly affected by the presence of unmatched and time variant loads. Thus, the knowledge of their time/frequency characteristics allows to predict their impact on the channel response.

3.1 Introduction

Some early work on modeling the characteristics of the in-home power line transmission medium at high frequencies (up to 30 MHz) has been done in [25–27]. It has been recognized that the channel response is deeply affected by the electrical device (load) impedances [28–31]. The knowledge of the load impedances allows the application of a bottom-up channel modeling approach through the use of transmission line (TL) theory as it is done for instance in [32–34].

In this chapter, we study the frequency behavior of such devices in terms of the voltage-to-current relation between the two feeding conductors, i.e., the line (hot) and the neutral wires. We consider the 2-30 MHz band that is used by broad band PLC systems. In most of the devices, the relation between voltage and current is linear and time invariant, i.e., the devices can be modeled as LTI loads characterized by their own frequency dependent impedance $Z(f)$. However, there exist some devices whose behavior is not linear and is determined by the sinusoidal mains signal. In [31], these devices are modeled as LPTV loads characterized by a time variant impedance $Z(t, f)$ that changes periodically and synchronously with the mains cycle. Two classes of LPTV devices have been identified. The first group of devices is characterized by two distinct states of impedance that vary within the mains cycle with a repetition rate of 100 Hz. The devices of the second group are instead characterized by less pronounced variations between the two states of impedance with a repetition rate of 50 Hz.

To get more insight, we have performed a measurement campaign on a large set of devices

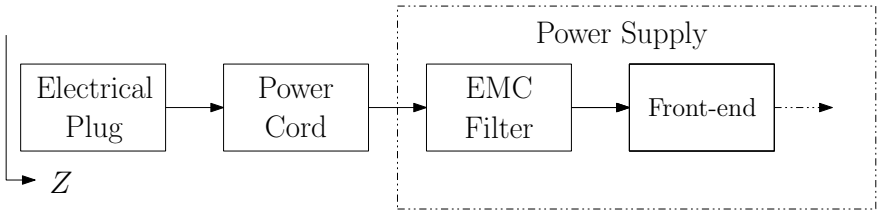

Figure 3.1: Block diagram of the input stage of a typical electrical device.

that can be found in a typical house or office, i.e., home appliances, office equipment and lighting system components. The devices have been collected in Italy where the mains signal has amplitude 230 V (r.m.s) and frequency 50 Hz. In particular, we have investigated the time variant behavior of the devices digging into the cause of it. Our measurement campaign has shown that the cause of the time variant behavior of these devices is the rectifier of the front-end circuitry of their power supply unit which may include uncontrolled rectifiers. However, since in our campaign we have found that only few devices are actually time variant, we show that the time variant behavior is significantly reduced by the presence of an electromagnetic interference (EMI) filter [35] that has to be deployed to fulfill with electromagnetic compatibility norms. Furthermore, most of the devices that we can find in a house or office are equipped with a power cord which has a dominant effect on the overall impedance profile.

Based on the measurement results, we propose a classification of devices according to their time/frequency impedance characteristics.

This chapter is organized as follows. In Section 3.2, we analyze the characteristics of the impedance of the electrical devices. Sections 3.3 and 3.4 deeply investigate the effect of the aforementioned EMI filter and power cord on the behavior of the load impedance. In Section 3.5, we propose a classification of the measured devices. Finally, the main findings are summarized.

3.2 Analysis of Load Impedance Behavior

In general, typical electrical devices that we can find in a house or office can be divided in two groups. Devices that are substantially ohmic loads, e.g., a toaster or a steam iron, and devices with a more complex behavior because they deploy a power supply unit. Usually, the devices are equipped with an electrical plug and with a power cord. The power cord is sometimes omitted, e.g., in the case of mobile phone chargers. For the devices belonging to the second group, we can depict the input stage as in Fig. 3.1. The power supply unit is often equipped with noise suppression capacitors or more complex EMI filters.

We have investigated the behavior of a broad set of devices, i.e., a number of PC power supplies, bluetooth and mobile phone chargers, halogen lamps with electronic ballasts, a

compact fluorescent lamp, a desk lamp, a vacuum cleaner, a coffee machine, a refrigerator, a microwave oven, an electrical steam cooker, a cooking mixer, an hairdryer, a DVD player, a CD player, an audio amplifier and a drill.

We have carried out measurements in the frequency domain (cf. Section 1.3.2). We have exploited the zero-span mode of the VNA. We have fixed the time span equal to the mains period, i.e., 20 ms, thus we have investigated the time variant behavior of the devices under test (DUTs) assuming the loads to be periodically time variant with a repetition frequency integer multiple of the mains frequency. The acquisition has been triggered on the 50 Hz mains signal and it has been done in the frequency band 2-30 MHz. A capacitive coupler has been used to protect the equipment from the mains voltage. The effect of the coupler as well as the effect of the power grid that supplies the DUTs have been compensated, as explained in Section 1.3.2.

Interestingly, we have found a limited number of devices characterized by a strong time variant behavior, namely, time variant loads. In addition, all the above time variant loads, except one (a bluetooth headset charger), have exhibited two states of impedance with a rate of 100 Hz. As it will be explained in the following analysis, the limited number of time variant devices is due to the fact that most of the modern power supplies are designed in such a way to minimize the generation of unwanted harmonics on the input current waveform through the use of noise suppression capacitors or more complex EMI filters. The scarcity of time variant devices with a rate of 50 Hz is instead due to the deployment of full-wave rectifiers instead of inefficient half-wave rectifiers that have limited usage in the modern power supplies.

In the next section, we will describe in detail the front-end block of the power supply unit. In particular, we analyze the power supply unit equipped with uncontrolled diode rectifiers.

3.2.1 Front-end of the Power Supply Unit

Basically, the front-end of most of the power supply units consists of an uncontrolled diode rectifier circuit and a “bulk” capacitor [35] that converts the input sinusoidal signal to a DC voltage. The process of continuously charging and discharging the “bulk” capacitor causes abrupt pulses of current when the instantaneous rectified voltage is higher than the DC voltage across the capacitor, which forwards biases the rectifier circuit [35]. Depending on the particular configuration of the rectifier circuit, the pulse of current appears twice or once during a mains period of 20 ms (Fig. 3.2). In full-wave uncontrolled rectifiers that use a diode bridge, the pulse of current appears every half mains cycle when two of the four diodes of the bridge are forward biased. In half-wave uncontrolled rectifiers that use a single diode, the pulse of current appears once during the positive cycle of the mains signal, when the single diode is forward biased. Therefore, the relation between voltage and current is not

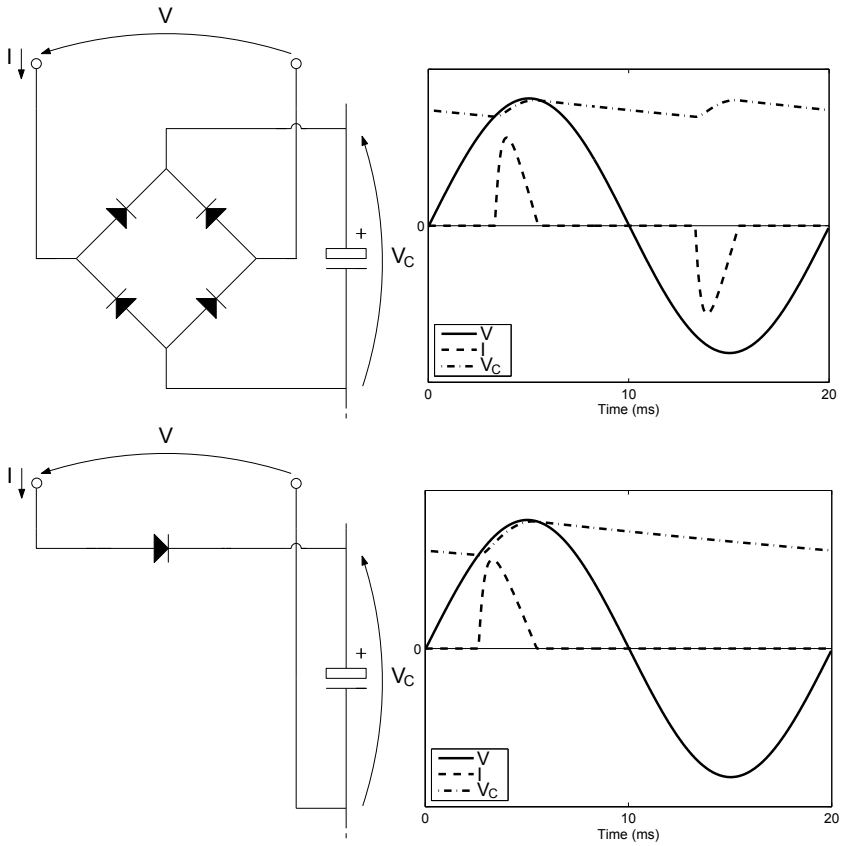

Figure 3.2: Example of diode rectifier circuits and waveforms of the voltage and of the current between the two feeding conductors and of the voltage across the capacitor.

linear. However, two states of the impedance can be distinguished allowing us to model the load as having a periodically time variant impedance [31]. The impedance variation between states has periodicity of 10 or 20 ms depending on the aforementioned uncontrolled rectifier circuitry, respectively a rate of 100 Hz or 50 Hz.

To substantiate our argument that the cause of the time variant behavior of some devices is simply the uncontrolled rectifier of the front-end circuitry of the power supply unit and it is not amenable to DIAC, TRIAC or SCR diodes of the internal circuitry, i.e., DIAC, TRIAC or SCR diodes as speculated in [31], we have proceeded as follows. We have identified two devices (a mobile phone charger and a compact fluorescent lamp (CFL)) inside which the electronic components just mentioned are present. As shown in Fig. 3.3, the impedance variations have been encountered at the peaks of the magnitude of the mains waveform, i.e., when the instantaneous rectified voltage is higher than the DC voltage across the internal "bulk" capacitor of the front-end circuitry of the power supply unit. Thus, we have applied different AC voltages to the DUTs by a test network and we have characterized their behavior under different conditions. We have applied a very low voltage (such that the diodes of the uncontrolled rectifier circuit are not forward biased) and a higher voltage (such that the diodes of the uncontrolled rectifier circuit are forward biased but not enough to switch ON

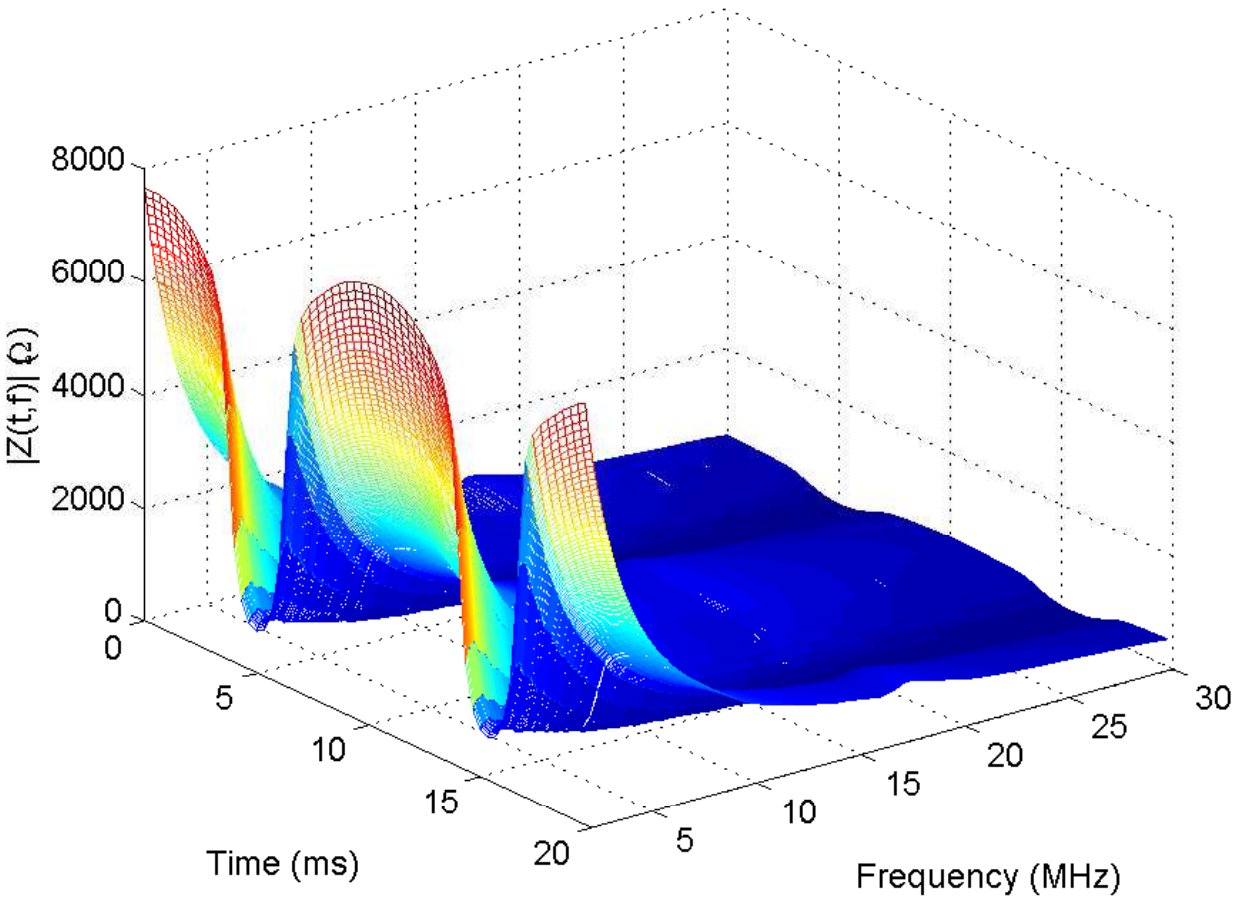

Figure 3.3: Magnitude of the impedance of a highly time variant mobile phone charger under test, during a time span equal to the mains period. The time instant 0 ms corresponds to the zero-crossing of the mains waveform (rising edge).

the internal driver circuit of the device). In the first case, we have noted the absence of a time variant behavior of the DUTs, while in the second case we have noticed a behavior identical to the case when the DUTs are supplied by the mains voltage. Therefore, we have concluded that the time variant behavior is simply due to the generation of current pulses by the front-end circuitry of the power supply unit.

Despite the fact that the front-end of the power supply unit exhibits a time variant impedance, the presence of an EMI filter significantly reduces it, as we will discuss in the following section.

3.3 Effect of the EMI Filter

We have focused on the mobile phone charger in Fig. 3.3 and we have identified a similar device from a different manufacturer, with different time/frequency characteristics. This device exhibited a time invariant behavior whose magnitude of the impedance is monotonically

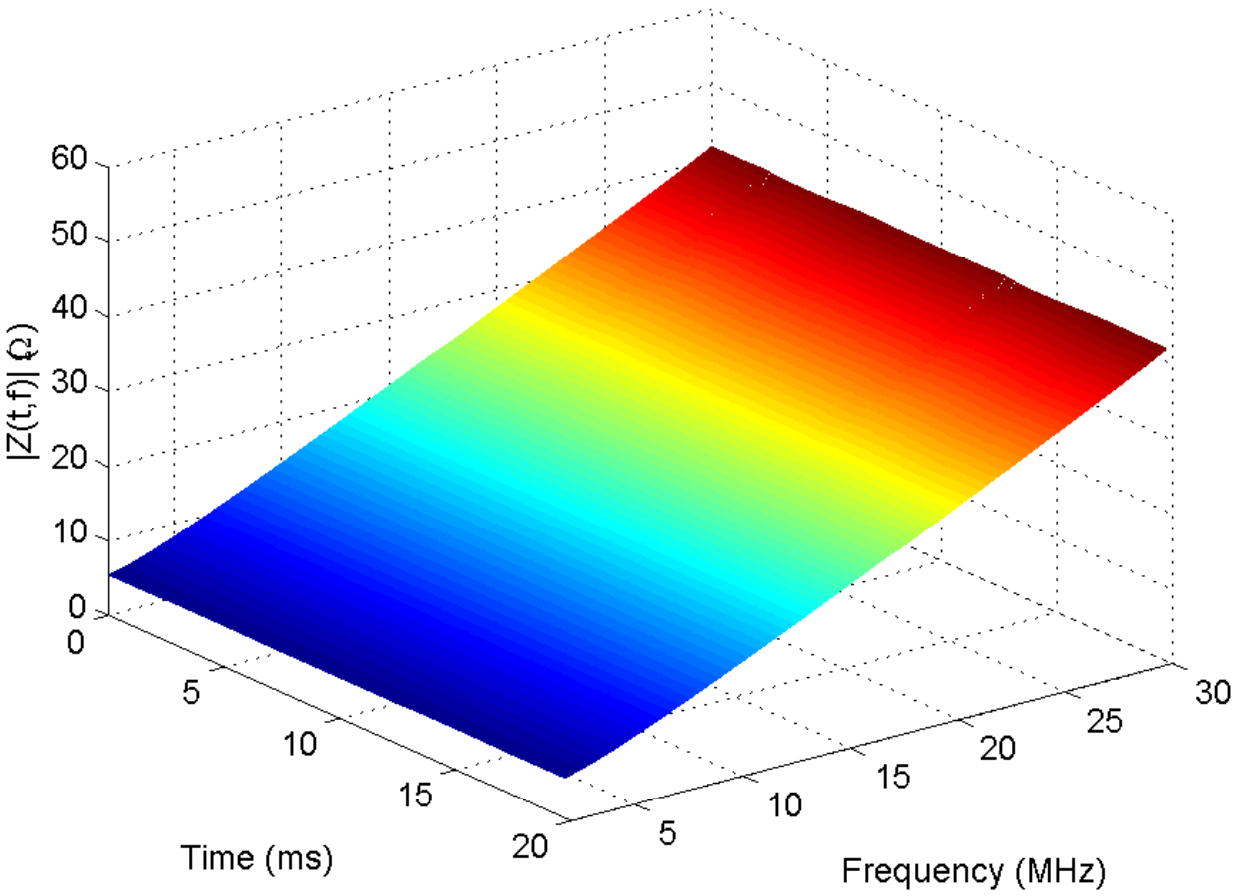

Figure 3.4: Magnitude of the impedance of a time invariant mobile phone charger, during a time span equal to the mains period.

increasing up to 50 Ω within the frequency band 2-30 MHz (Fig. 3.4).

The internal circuitry of the two DUTs has been analyzed and it has been found that the rectifier circuit of both devices is a full-wave uncontrolled rectifier, but the second mobile phone charger is equipped with a noise suppression capacitor between the line and the neutral terminals on the input stage of the power supply unit. Thus, we have searched for other devices whose magnitude of the impedance is time invariant and monotonically increasing. Electronic ballasts for halogen lamps and PC power supplies belong to this class of devices. It has been found that all of them deploy an EMI filter or a noise suppression capacitor between the line and the neutral terminals. Although there exist several types of EMI filters, they all use at least one line-to-line capacitor, also known as X-cap [35], whose goal is to suppress differential mode currents that flow along the line (hot) conductor and return through the neutral one. More details are given in the Appendix B. The magnitude of the impedance of the line-to-line capacitor is relatively small compared to the impedance of the device without the noise suppression capacitor within the frequency band 2-30 MHz. As a consequence, it imposes a low impedance to the input of the circuit and it reduces any impedance variation.

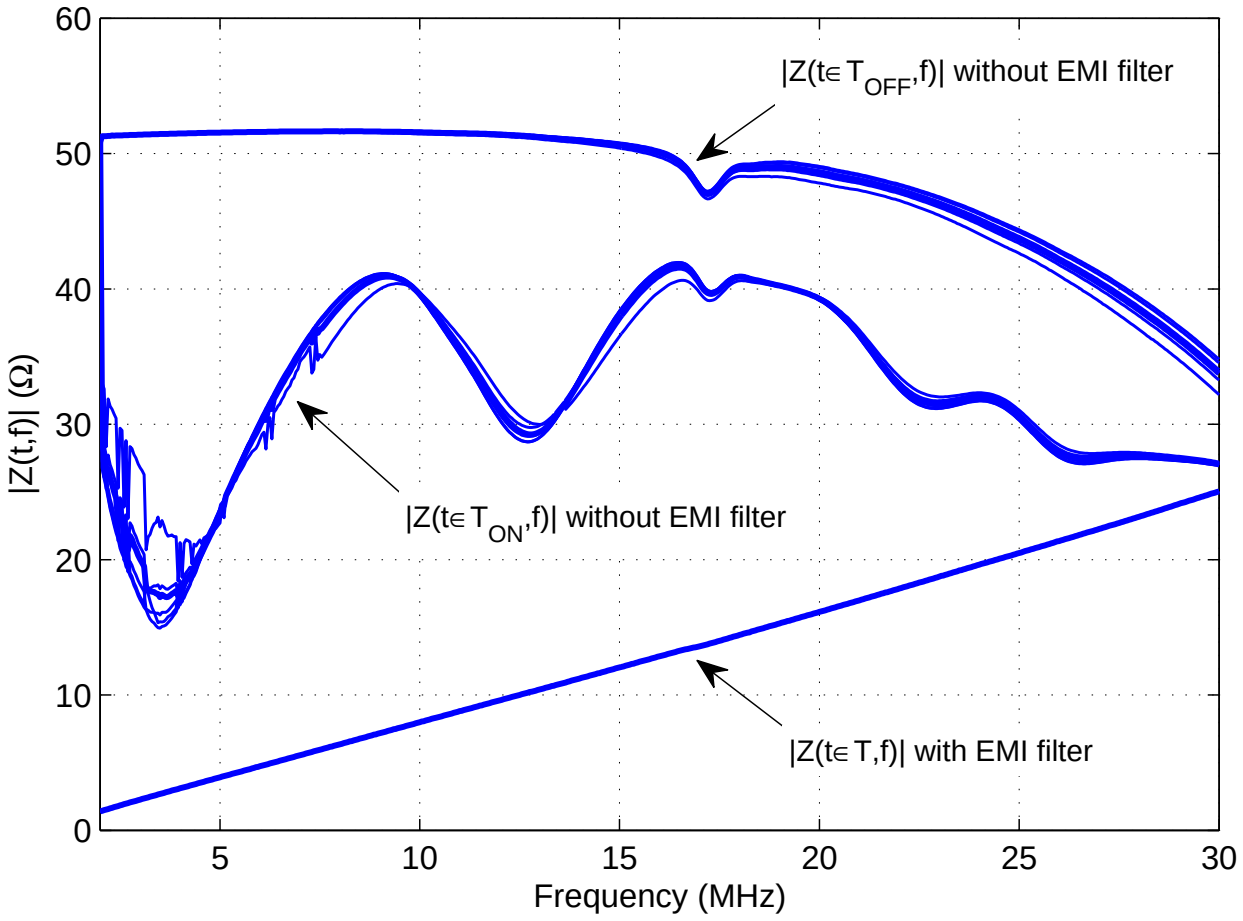

Figure 3.5: Magnitude of the impedance of the PC power supply under test for different time instants within a period of the mains signal, with and without EMI filter circuitry. T is the period of the mains waveform, T_{ON} and T_{OFF} are the time intervals when the diodes of the uncontrolled rectifier circuit are respectively forward biased or not.

To experimentally prove that the EMI filter reduces the devices impedance time variations, we have selected a PC power supply and physically removed all the electronic components composing the EMI filter. Then, we have performed a new measurement. As expected, we have found that with this configuration the time variant behavior is exhibited. In Fig. 3.5, we show the magnitude of the impedance of the PC power supply under test for different time instants within a period T of the mains waveform, with and without the EMI filter circuitry. We denote with T_{ON} and T_{OFF} as the time intervals when the diodes of the uncontrolled rectifier circuit are respectively forward biased or not. The figure shows that the magnitude of the impedance of the device without the EMI filter is higher than the impedance of the device with the EMI filter and variations are exhibited only without the EMI filter. Furthermore, in Fig. 3.6-(a) we show that the impedance of the PC power supply under test is equal to the impedance of the X-cap in the frequency range 2-30 MHz.

Now, we prove that the low values and the monotonically increasing profile of the magnitude of the impedance are due to the parasitic inductance of the lead wires of the X-cap.

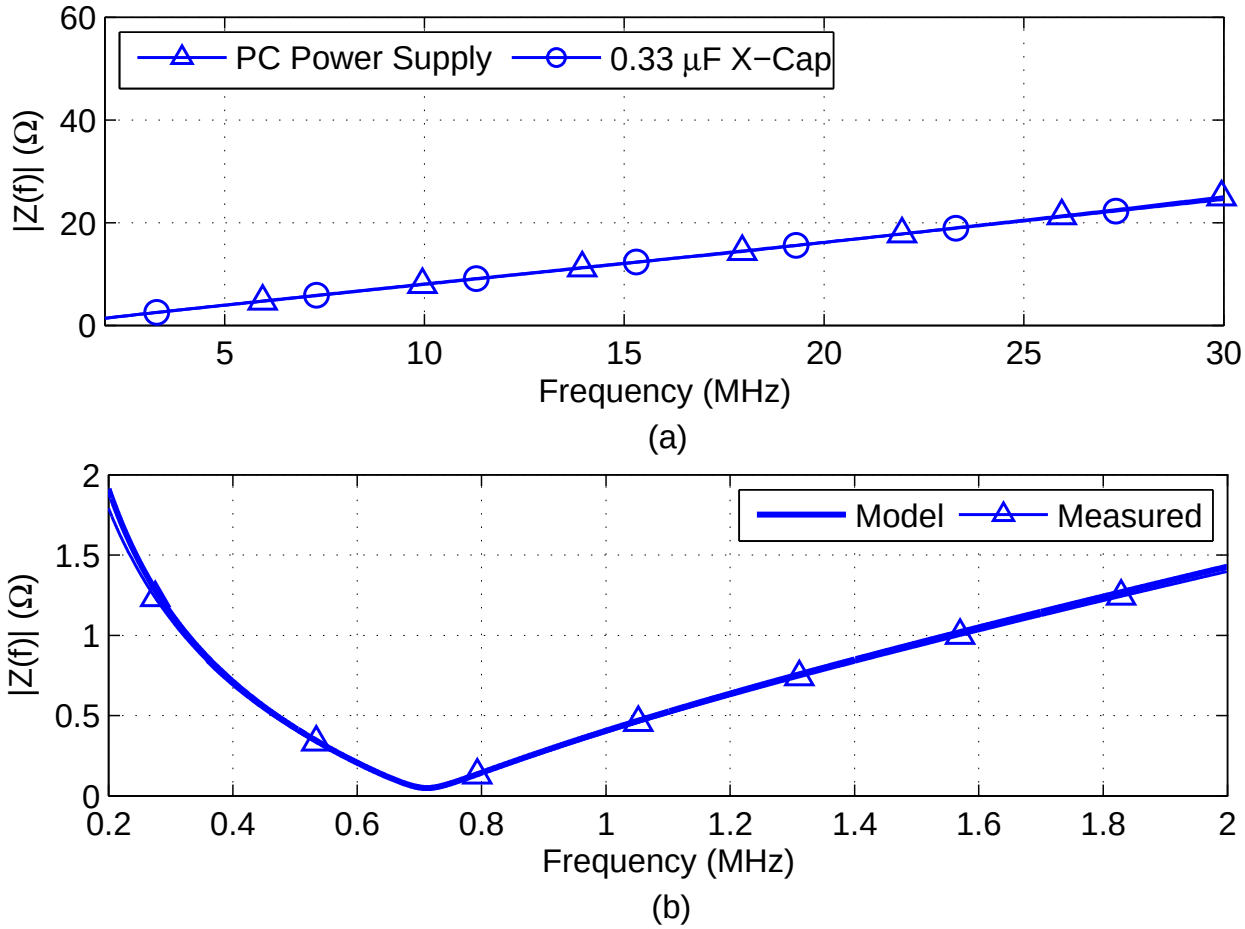

Figure 3.6: (a) Magnitude of the impedance of the PC power supply under test and of the X-cap of its EMI filter and (b) comparison between the magnitude of the impedance of the X-cap and of the lumped circuit model, within an extended frequency range (200 kHz-2 MHz).

We have measured the impedance of the X-cap within an extended frequency range. The lumped circuit model that yields considerable insight into the non-ideal behavior of a real capacitor is the series combination of an ideal capacitance C, a certain inductance due to the component attachment leads L_l and an equivalent series resistance (ESR) R_{ESR} [35]. As shown in Fig. 3.6-(b), at low frequencies, the impedance of the capacitor is dominant and the magnitude of the impedance of the real capacitor is $|Z_C(f)| \approx 1/(2\pi f C)$ which decreases with frequency. As frequency increases, the effect of the parasitic inductance becomes not negligible, as its impedance reads $|Z_{L_l}(f)| \approx 2\pi f L_l$. At the self-resonant frequency of the capacitor $f_0 = 1/2\pi\sqrt{L_l C}$ [35], the impedances of the ideal capacitor and of the parasitic inductance are the same and equal to the ESR resistance [35]. In Fig. 3.6-(b), the self-resonant frequency of the 0.33 μF noise suppression capacitor is at about 700 kHz. After this frequency, the impedance of the real capacitor is dominated by the parasitic inductor and it increases linearly with frequency.

It should be noted that the above considerations are valid for frequencies above 2 MHz, since the self-resonance frequency of the common noise suppression capacitors is always smaller than 2 MHz.

3.4 On the Power Cord Effect

So far, we have considered devices without a power cord. Our measurement campaign has shown that the power cord has a significant effect on the resulting impedance of the devices. Most of the devices that we can find in a house or office have a power cord with length that ranges from tens of centimeters, e.g., for a laptop adapter, to meters, e.g., for a vacuum cleaner.

As it will be shown in the following, the magnitude of the impedance of these devices exhibits a series of damping peaks and nulls at regular intervals within the considered frequency band. At the frequencies where the peaks occur, the devices act as parallel resonant circuits and their behavior swaps from inductive to capacitive. Conversely, at the impedance nulls the devices behave as series resonant circuits, moving from a capacitive to an inductive behavior. At the parallel and series resonant frequencies, the phase of the impedance is always zero and the devices act respectively as a high or low purely resistive load.

We can explain such a behavior using TL theory concepts. The power cord acts as a transmission line of length L characterized by its characteristic impedance $Z_c(f)$ and its propagation constant $\gamma(f)$. The propagation constant is defined as $\gamma(f) = \alpha(f) + j\beta(f)$, where $\alpha(f)$ and $\beta(f)$ are the attenuation and phase constants, respectively, and j is the imaginary unit. In Fig. 3.7, we show the profiles of the aforementioned constitutive parameters of a typical 3-wires power cable (3x1.5 mm^2 *H05VV-F* flexible cable, insulated and outer sheathed in PVC), obtained via measurements. The resonant behavior is due to the impedance mismatch between the line characteristic impedance and the impedance of the load at the end of the power cord. The decreasing profile of the amplitude of the peaks with frequency is instead amenable to the resistive losses of the cable. The number of peaks and nulls within the considered frequency band is variable and it depends on the length of the cable and on its constitutive parameters.

In the following, we show that it is possible to predict the impedance of the devices equipped with a power cord. We assume such devices composed by a low losses transmission line terminated in a purely resistive load R_l. Therefore, the input impedance reads

$$Z(f) = Z_c(f)\frac{R_l + Z_c(f)\tanh(\gamma(f)L)}{Z_c(f) + R_l\tanh(\gamma(f)L)}. \tag{3.1}$$

The value of the purely resistive load that best fits the impedance profile of the measured devices is obviously a function of the constitutive parameters of the power cord and of its length. In the following, we derive an analytic expression of R_l. To proceed, it is useful to

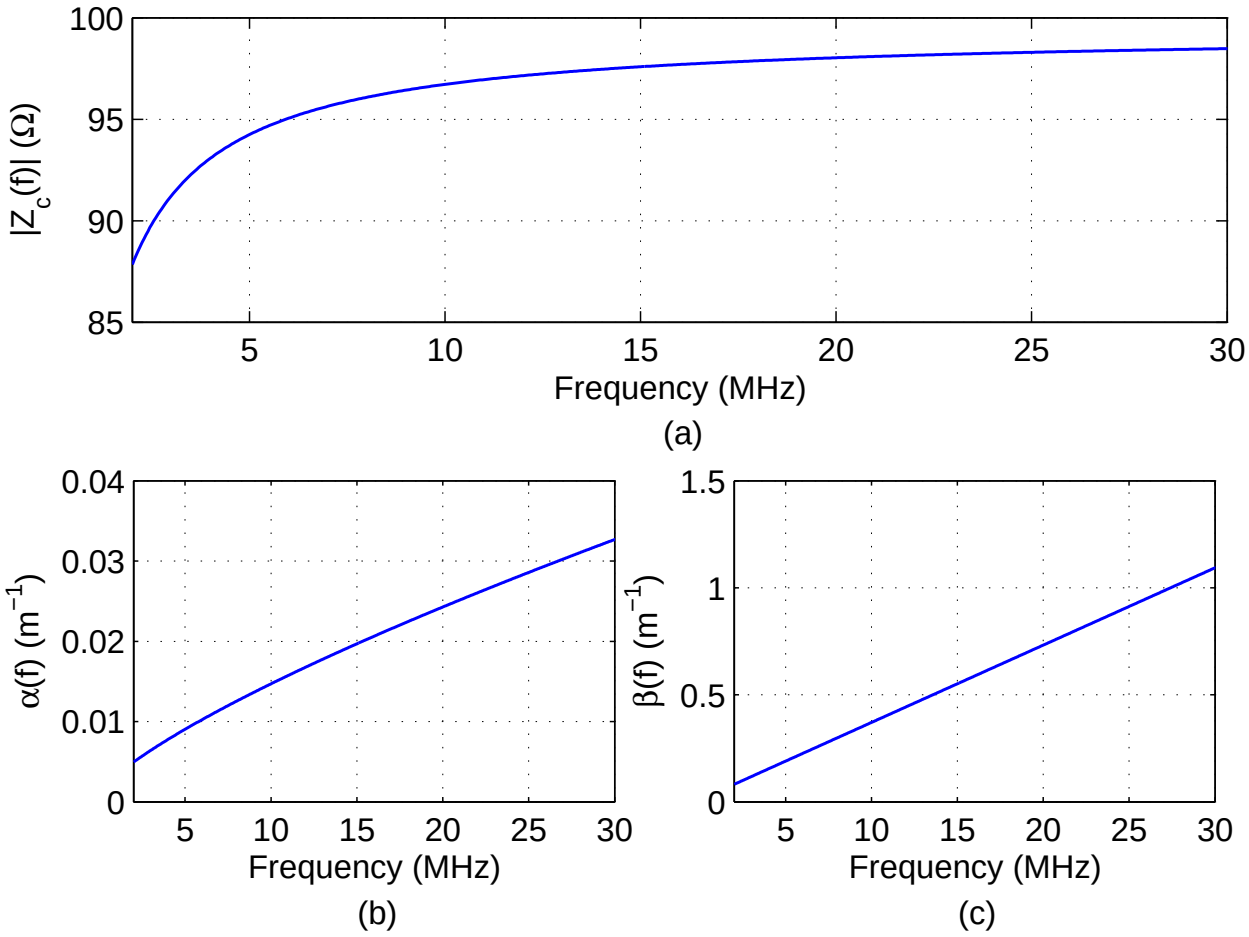

Figure 3.7: (a) Profile of the characteristic impedance $Z_c(f)$, (b) of the attenuation constant $\alpha(f)$, (c) of the phase constant $\beta(f)$ of a typical 3-wires power cable (3x1.5 mm^2 *H05VV-F* flexible cable, insulated and outer sheathed in PVC).

expand $\tanh(\gamma(f)L)$ in (3.1) as follows

$$\tanh(\gamma(f)L) = \frac{\tanh(\alpha(f)L) + j\tan(\beta(f)L)}{1 + j\tanh(\alpha(f)L)\tan(\beta(f)L)}. \tag{3.2}$$

The parallel and series resonant frequencies mentioned above are those at which the input impedance is purely real, i.e., when $\tan(\beta(f)L) = 0$ or $\tan(\beta(f)L) \to \infty$. Now, we focus on the analytic derivation of such frequencies. We proceed as follows. Via measurements, we have found that the dielectric constant in several common power cords can be expressed as

$$\epsilon(f) = \epsilon_0 \left[\frac{K}{f} + \epsilon_\infty\right], \tag{3.3}$$

where ϵ_0 is the vacuum dielectric constant, K is a weighting factor and ϵ_∞ is the asymptotic relative dielectric constant. Via measurements and TL theory, we obtain the per-unit-length (p.u.l.) constitutive parameters of some common 2-wires and 3-wires power cables, i.e., the

p.u.l. resistance $r(f)$ (Ω/m), conductance g (S/m), capacitance $c(f)$ (F/m) and inductance l (H/m). We emphasize the frequency dependence of the p.u.l. resistance and capacitance. The p.u.l. resistance increases at a rate proportional to $\sqrt{f}$ due to the skin effect [35], while the p.u.l. capacitance decreases as the dielectric constant. Thus, under the assumption of low losses transmission line [35], we can calculate the characteristic impedance and the propagation constant as

$$Z_c(f) \approx \sqrt{\frac{l}{c(f)}}, \tag{3.4}$$

$$\gamma(f) \approx \frac{r(f)}{2Z_c(f)} + j2\pi f\sqrt{lc(f)}. \tag{3.5}$$

Without any loss of generality, we also make the assumption that the p.u.l. resistance does not affect the phase constant. According to [36], if the medium that surrounds the conductors is homogeneous and is characterized by a magnetic permeability equal to the vacuum permeability μ_0 and has dielectric constant $\epsilon(f)$, the p.u.l. inductance and the dielectric constant are related as $lc(f) = \mu_0\epsilon(f)$. Therefore, from (3.5), $\beta(f) = 2\pi f\sqrt{lc(f)} = 2\pi f\sqrt{\mu_0\epsilon(f)}$. As a consequence, the frequencies at which $\tan(\beta(f)L) = 0$ or $\tan(\beta(f)L) \to \infty$ read

$$f_0^{(m)} = \frac{-K + \sqrt{K^2 + 4\epsilon_\infty \left(\frac{m\nu_0}{2L}\right)^2}}{2\epsilon_\infty}. \tag{3.6}$$

where $\nu_0 = 1/\sqrt{\mu_0\epsilon_0}$ is the vacuum light speed and

$$m = \begin{cases} 0, 1, \ldots & \text{such that } \tan(\beta(f)L) = 0 \\ 1/2, 3/2, \ldots & \text{such that } \tan(\beta(f)L) \to \infty\,. \end{cases}$$

The first resonant frequency greater than 0 is $\hat{f}_0 = f_0^{(1/2)}$. Given $\hat{f}_0$ and the measured impedance value of the DUT at that frequency, namely $\widehat{Z}$, the purely resistive load R_l that allows an excellent fit with the measured impedances is obtainable from (3.1) as

$$R_l = Z_c(\hat{f}_0)\frac{\widehat{Z}\tanh(\alpha(\hat{f}_0)L) - Z_c(\hat{f}_0)}{Z_c(\hat{f}_0)\tanh(\alpha(\hat{f}_0)L) - \widehat{Z}}. \tag{3.7}$$

The desired input impedance $\widehat{Z}$ at $\hat{f}_0$ can assume values in prefixed ranges to obtain real positive vales of R_l, i.e.,

$$\begin{cases} \text{peak at } \hat{f}_0 & \widehat{Z} >> Z_c(\hat{f}_0) \wedge \widehat{Z} < \frac{Z_c(\hat{f}_0)}{\tanh(\alpha(\hat{f}_0)L)} \\ \text{null at } \hat{f}_0 & \widehat{Z} > Z_c(\hat{f}_0)\tanh(\alpha(\hat{f}_0)L) \wedge \widehat{Z} << Z_c(\hat{f}_0). \end{cases}$$

All of the measured devices satisfy this constraint. From (3.7), if the impedance of the device exhibits a peak at $\hat{f}_0$, the value of the purely resistive load R_l of the model will be

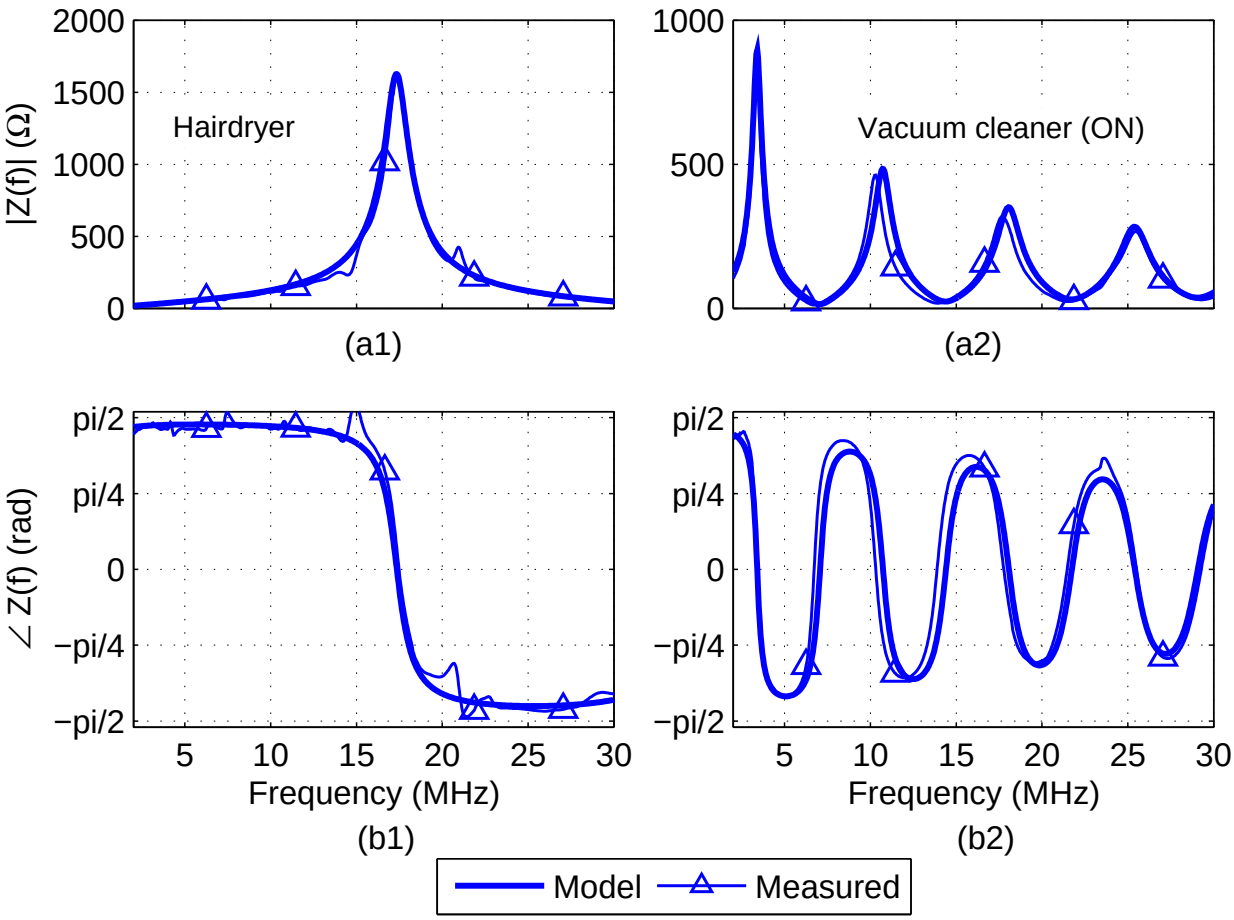

Figure 3.8: (a1)-(a2) Magnitude and (b1)-(b2) phase of measured and modeled impedance of two devices under test equipped with a power cord whose behavior at low frequencies (before the first resonant frequency) is inductive.

low. Conversely, if the impedance exhibits a null, R_l will be high.

An excellent agreement is found between the model in (3.1) and the measured impedances. In detail, in Fig. 3.8 we show the comparison of the magnitude and the phase of the impedance of two devices equipped with a power cord whose behavior at low frequencies (before the first resonant frequency) is inductive, i.e., an hairdryer (Figs. 3.8-(a1),(b1)) and a switched ON vacuum cleaner (Figs. 3.8-(a2),(b2)). In Fig. 3.9, we compare the results of two different devices equipped with a power cord whose behavior at low frequencies (before the first resonant frequency) is capacitive, i.e., a desk lamp (Figs. 3.9-(a1),(b1)) and the same vacuum cleaner of Fig. 3.8, but switched OFF (Figs. 3.9-(a2),(b2)) This distinction will be discussed in the following section. Furthermore, it should be noted that herein we have considered time invariant loads but the effect of the power cord is essentially the same in LPTV loads.

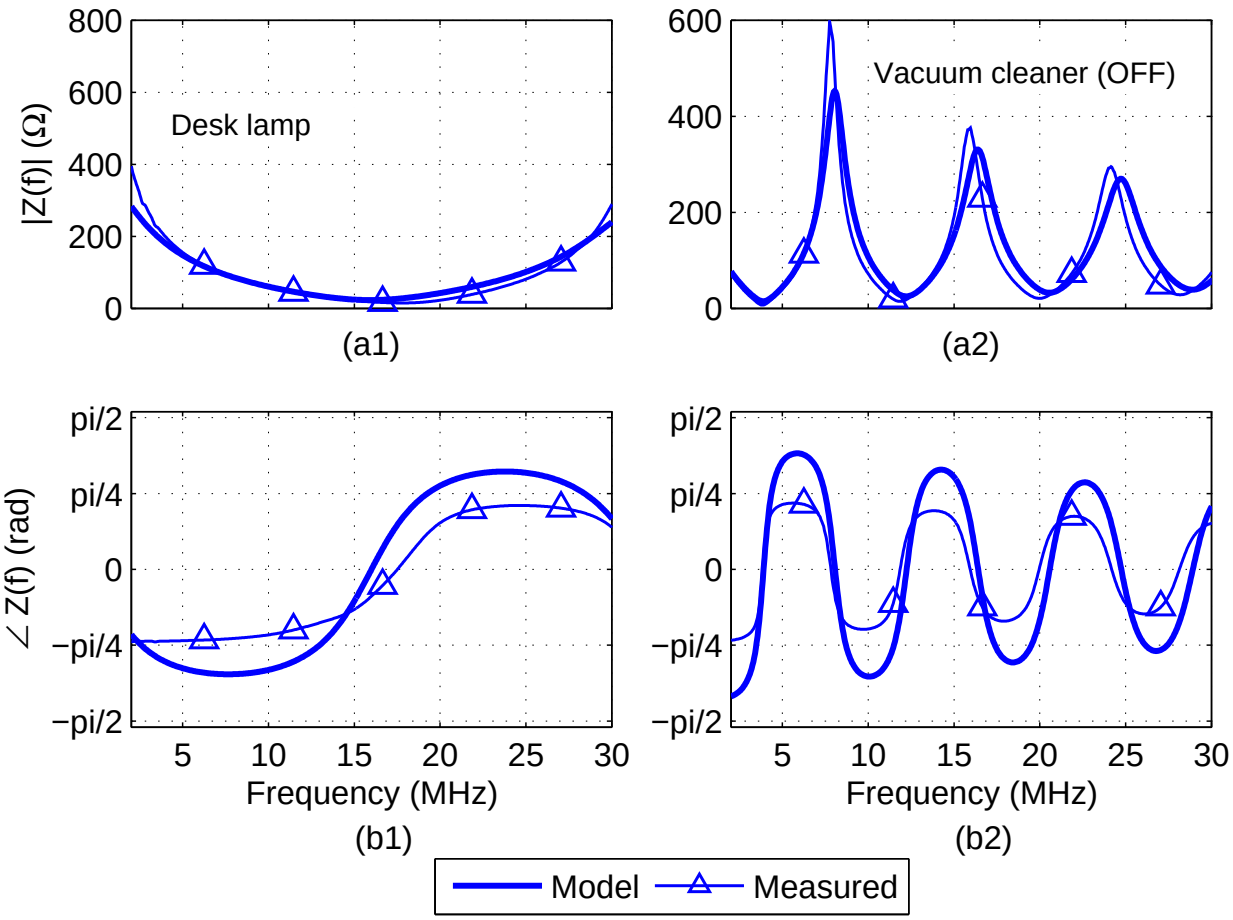

Figure 3.9: (a1)-(a2) Magnitude and (b1)-(b2) phase of measured and modeled impedance of two devices under test equipped with a power cord whose behavior at low frequencies (before the first resonant frequency) is capacitive.

3.5 Classification of the Measured Devices

As discussed, we can divide the measured devices between those characterized by a time variant or a time invariant impedance. It should be noted that a distinction between time variant and time invariant loads by type of device is not always possible since similar devices from different manufactures may have different characteristics, e.g., they may be equipped with different power supplies or circuitry for the noise and the electromagnetic interference suppression.

First of all, we focus on the database of the time invariant loads and we propose three classes, as discussed in the following.

A first macro classification can be made according to the profile of the magnitude of the impedance. If it is monotonically increasing, as for the devices without a power cord and equipped with an X-cap between the two feeding conductors, the load can be included in Class A. If it exhibits the damping peaks and nulls within the considered frequency band, as for the devices with a power cord, the load can be included in Class B.

Table 3.1: Class A - Time invariant devices without power cord.

Device Under Test	Operating state
PC power supply (Fig. 3.6-(a))	ON/OFF
Halogen lamp with electronic ballast	ON/OFF
Mobile phone charger (Fig. 3.4)	ON/OFF

Table 3.2: Class B-1 - Time invariant devices with power cord.

Device Under Test	Operating state	Cable length L [m]
Vacuum cleaner	ON	10
Drill	ON	1
Vending coffee machine	ON	3
Refrigerator	ON	3
Hairdryer	ON/OFF	1.80
Microwave oven	ON/OFF	2
DVD Player	ON/OFF	2
Cooking mixer	ON/OFF	1.5

Class A includes the devices listed in Table 3.1. In Fig. 3.10, we show the magnitude and phase of their impedance. We highlight the fact that these devices belong to this macro class whatever the operating state is (switched ON or OFF).

The devices of Class B are further classified into two subclasses according to their behavior at low frequencies (before the first resonant frequency), i.e., if it is inductive (Class B-1) or capacitive (Class B-2). This is equivalent to discriminate whether the profile of the impedance exhibits a peak or a null at the first resonant frequency. In Table 3.2 and Table 3.3, we list the aforementioned devices and, in Fig. 3.11 and Fig. 3.12, we show the magnitude and phase of the impedance of three representative devices. Some devices may be included in both subclasses, according to their operating state (switched ON or OFF). These devices essentially consist of an electrical motor.

The devices belonging to Class B-1, regardless of what their operating state is (switched ON or OFF), are characterized by a low impedance at the end of the power cord. These devices are certainly equipped with an X-cap between the two feeding conductors that imposes a low impedance value as discussed in the previous section. From these considerations, some of the devices belonging to the Class A, i.e., the halogen lamps with electronic ballasts and the PC power supplies, can be included into this subclass when they are supplied using a power cord whose length is not negligible.

Conversely, the devices belonging to Class B-2, regardless of what their operating state is, are characterized by an high impedance at the end of the power cord. This devices are equipped with a particular power supply unit whose input stage is a power transformer

Table 3.3: Class B-2 - Time invariant devices with power cord.

Device Under Test	Operating state	Cable length L [m]
Vacuum cleaner	OFF	10
Drill	OFF	1
Vending coffee machine	OFF	3
Refrigerator	OFF	3
Desk lamp	ON/OFF	1.80
CD Player	ON/OFF	2
Electrical steam cooker	ON/OFF	1
Audio amplifier	ON/OFF	1

Table 3.4: Class C - Time variant devices without power cord.

Device Under Test	TV Rate [Hz]
Compact fluorescent lamp	100
Mobile phone charger (Fig. 3.3)	100
Bluetooth headset charger	50

followed by an EMI filter that induces a time invariant behavior.

In Tables 3.2 and 3.3, we have included the length of the power cord. We remark that the number of peaks and nulls within the considered frequency band is variable and it depends on the constitutive parameters of the cable and on its length. In particular, as shown by (3.6), the longer the cable, the larger the number of peaks and nulls is.

Given the rarity of devices characterized by strong time variant behavior, we propose a single macro class for them, i.e., Class C. In Table 3.4, we list the measured devices belonging to this class and we report the time variation rate (TV rate). In Fig. 3.13, we show the magnitude and the phase of the two impedance states for one representative device of Class C, i.e., the compact fluorescent lamp. It should also be noted that if the time-variant device is equipped with a power cord with non-negligible length, considerations similar to those made for Class B-1 and B-2 can be made. That is, the profile of each of the two impedance states will be similar to that in Class B-1 or Class B-2.

3.6 Main Findings

In this chapter, we have dealt with the analysis of the load impedances that are present in home power grids. The analysis is motivated by the fact that such loads significantly affect the power line communication channel. We have performed a measurement campaign on a large set of devices that can be found in a typical house or office, i.e., a number of home appliances, office equipment and lightning system components. We have investigated the

frequency behavior of such devices in terms of voltage-to-current relation between the two feeding conductor, i.e., the line and the neutral wires, in the frequency range 2-30 MHz. Due to the fact that some devices exhibit a periodically time variant impedance with repetition frequency that is an integer multiple of the mains frequency. Interestingly, we have found a limited number of devices characterized by a strong time variant behavior. We have found that the cause of the impedance time variations is simply due to the front-end circuitry of the power supply unit of these devices. In fact, the generation of current pulses when the diodes of the uncontrolled rectifier circuits are forward biased, leads to a nonlinear relation between voltage and current. Nevertheless, a two states linear relation can be defined. Furthermore, the deployment of EMI filters or noise suppression capacitors between the line and the neutral terminals significantly reduces the time variations. We have both experimentally and theoretically proved the above considerations. Our measurement campaign has also considered the effect of the power cord on the resulting impedance of the devices. Finally, we have proposed a classification of the measured devices according to their time/frequency characteristics.

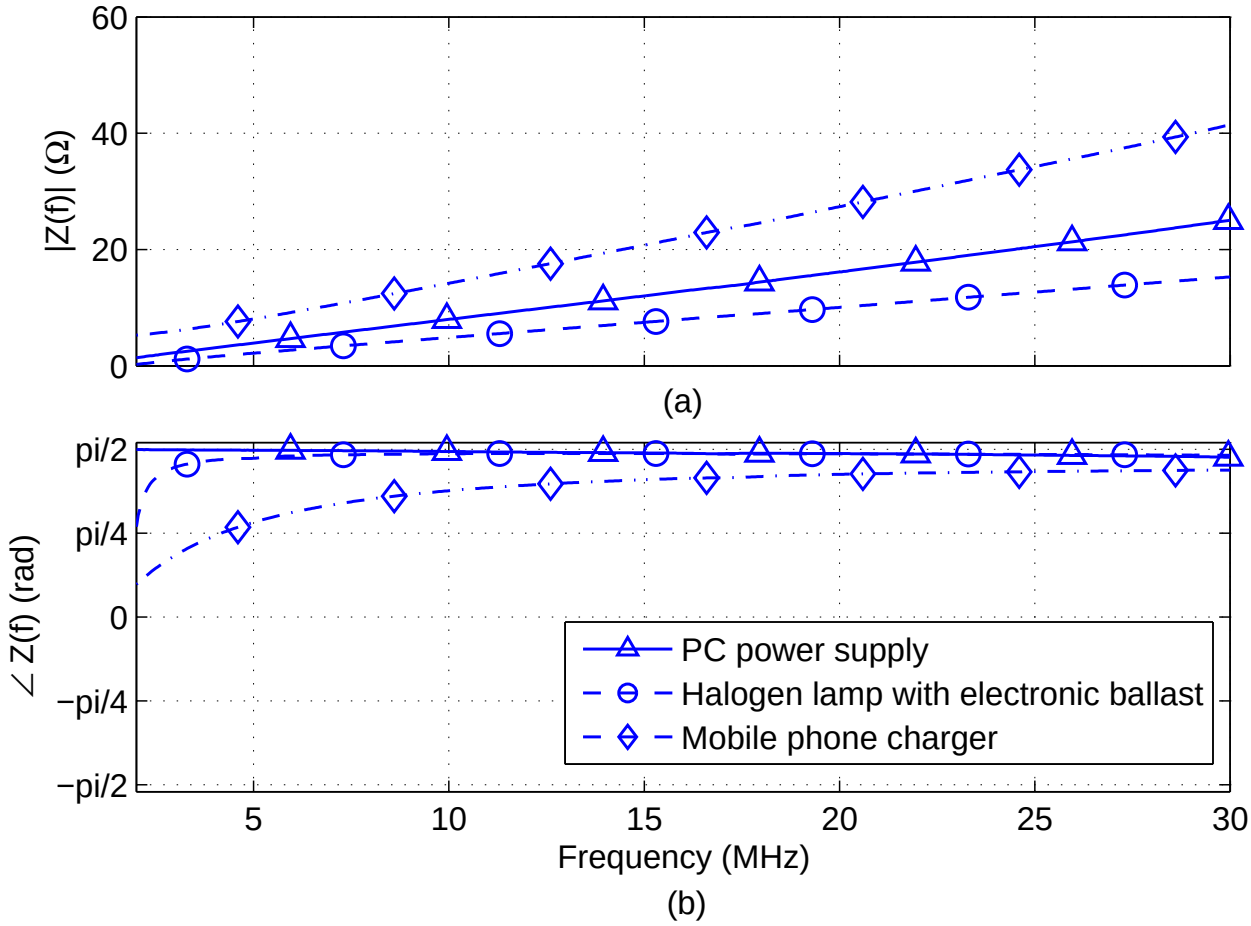

Figure 3.10: (a) Magnitude and (b) phase of the impedance of three representative devices of Class A.

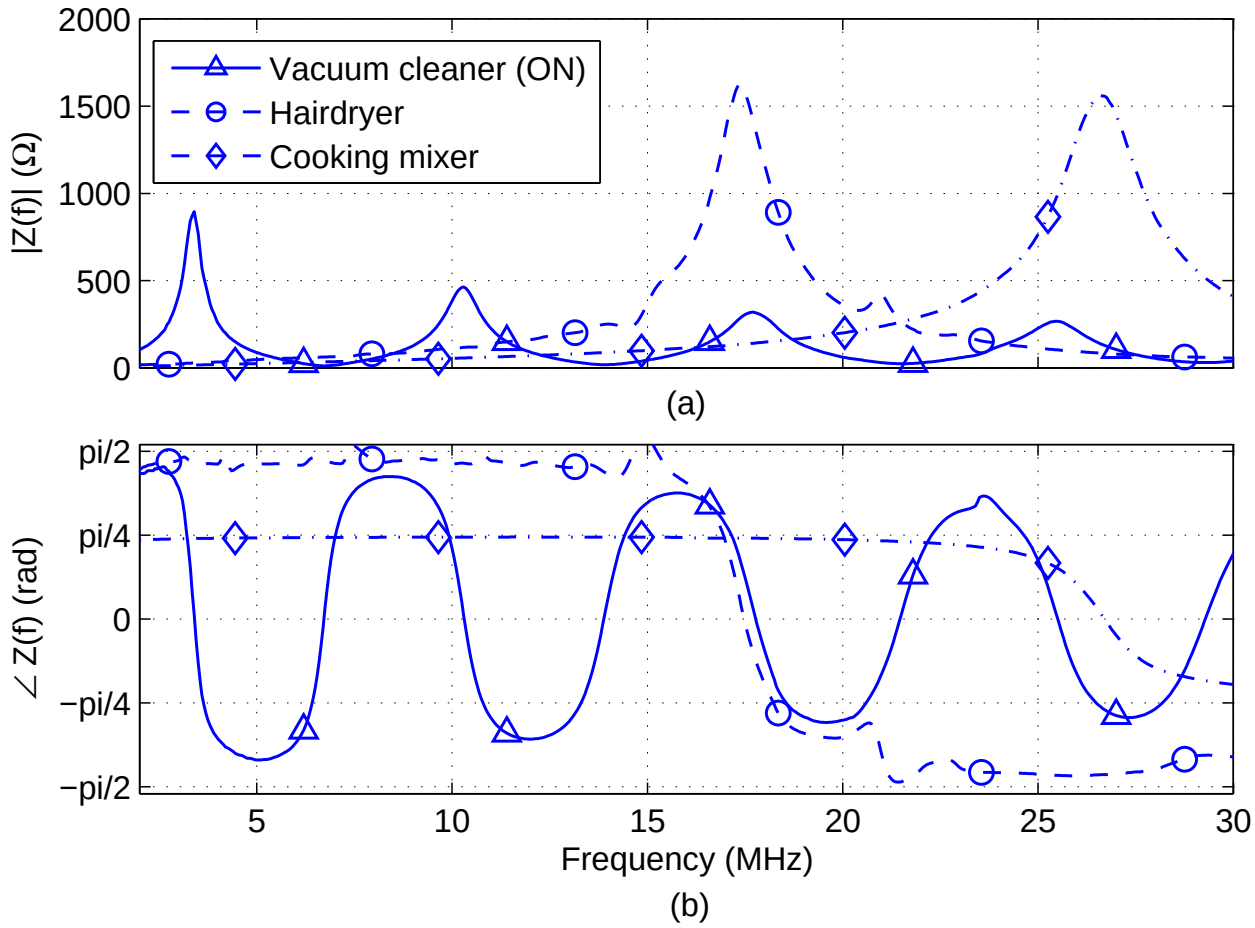

Figure 3.11: (a) Magnitude and (b) phase of the impedance of three representative devices of Class B-1.

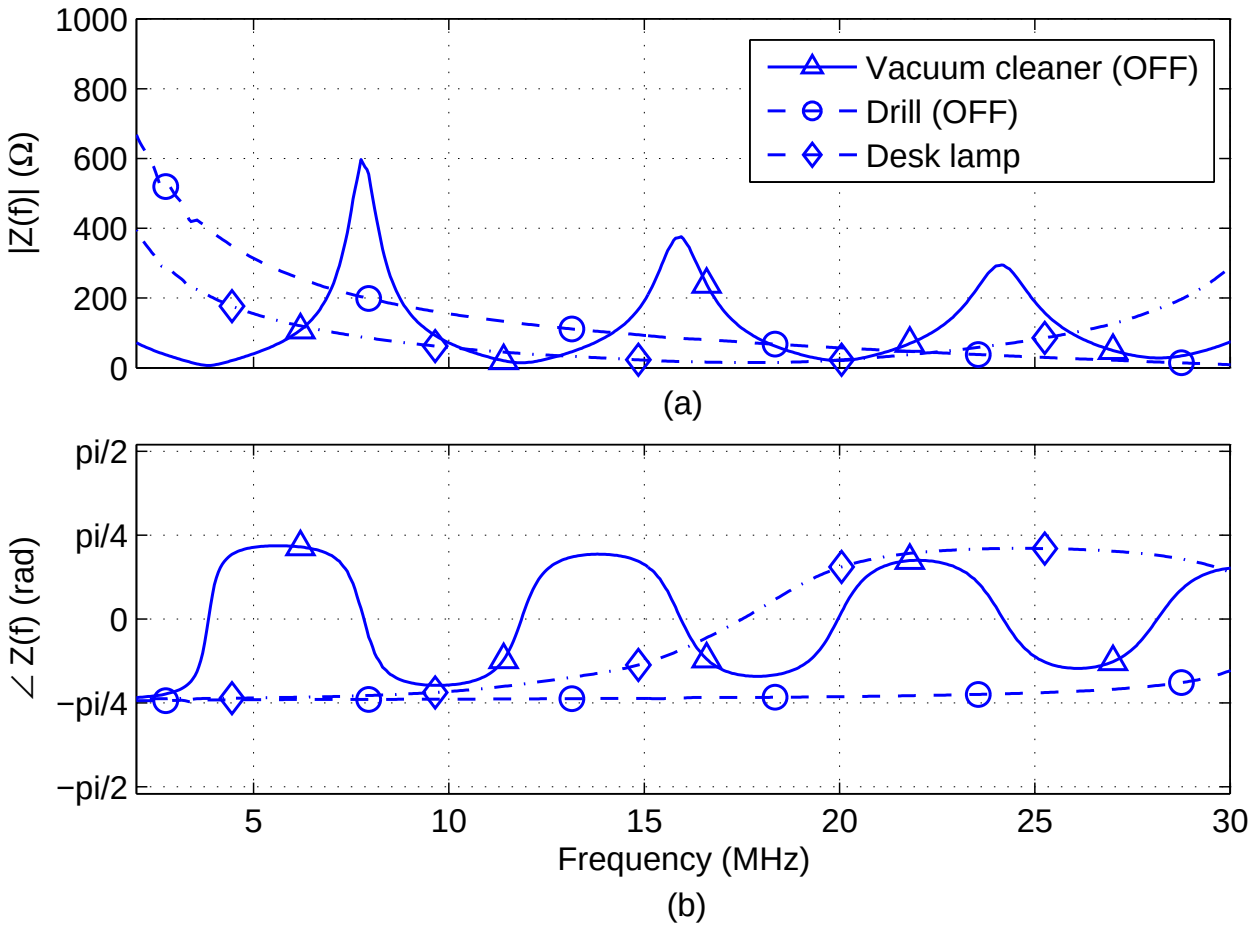

Figure 3.12: (a) Magnitude and (b) phase of the impedance of three representative devices of Class B-2.

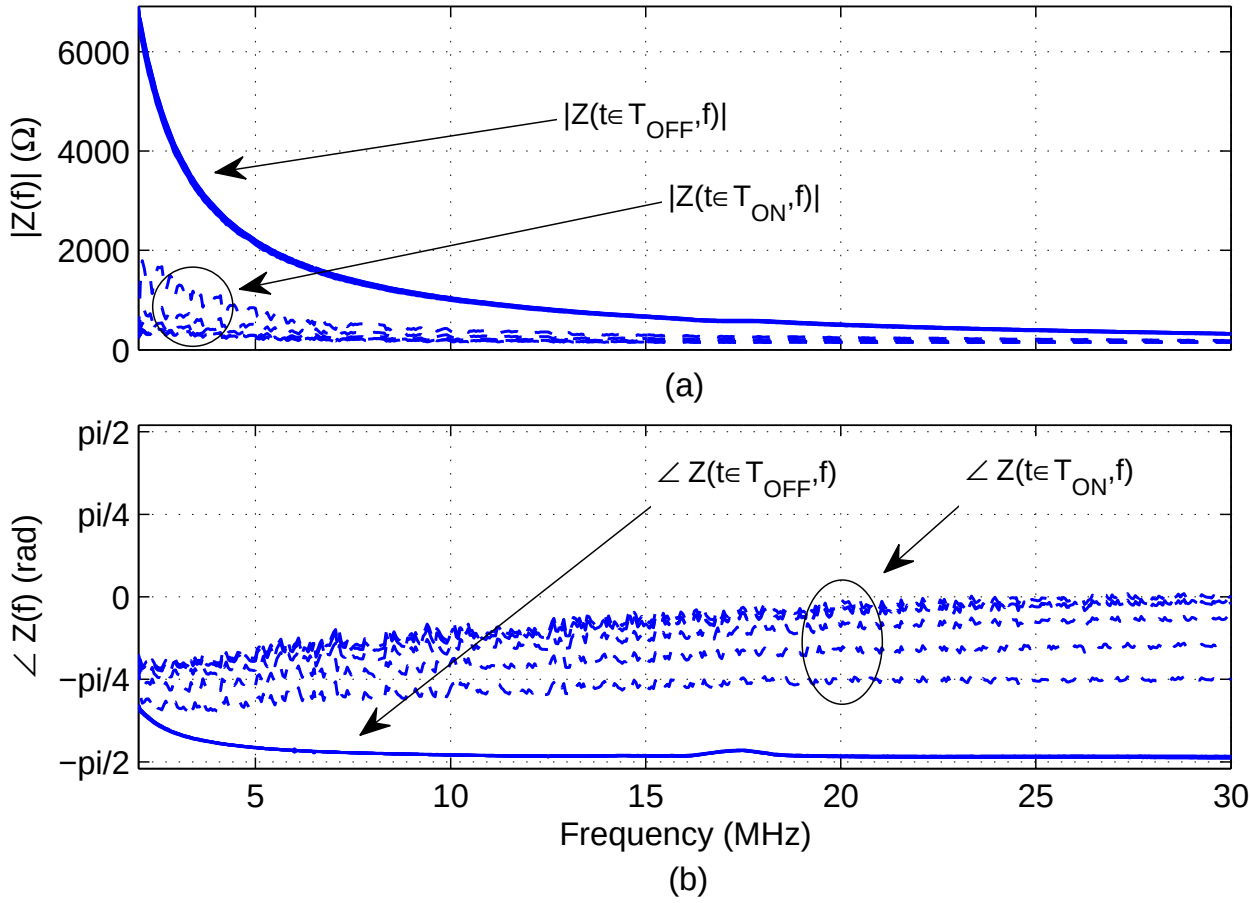

Figure 3.13: (a) Magnitude and (b) phase of the impedance of the compact fluorescent lamp belonging to Class C.

Chapter 4

Noise at the Source

In this chapter, we characterize the loads connected to the home/office power grid in terms of the impulsive noise components that they inject into the network. In fact, the electrical appliances are the main sources of noise in the in-home PLC.

We have performed noise at the source measurements in order to deeply characterize the noise injected by any single appliance.

4.1 Introduction

The PLC noise consists of background and impulsive noise contributions [18].

The background noise is caused by the activity of the household appliances that are connected to the power network and by the external broadcast radio narrow band interferences that are captured by wirings. As explained in Section 1.4.1, the PLC background noise is modeled as stationary, additive colored Gaussian noise, and several models were presented to describe its PSD [32], [37].

The impulsive noise comprises periodic impulsive noise components synchronous with the mains, asynchronous with the mains and asynchronous impulsive noise. The periodic impulsive noise synchronous with the mains is cyclostationary, with a repetition rate equal to or double that of the mains signal, and it is originated typically by the SCRs of the power switching supplies of the appliances connected to the grid. The periodic impulsive noise asynchronous with the mains is cyclostationary as well, but it exhibits repetition rates between 50 and 200 kHz [18]. The asynchronous impulsive noise is the most unpredictable component and it is due to the plugging in/out, switching ON/OFF of the electrical appliances.

Accurate models of the PLC impulsive noise parameters are fundamental for the design of both the protection circuitry against the high aperiodic spikes, and the communication algorithms to cope with the cyclostationary nature of the periodic impulsive noise components. In the literature, the impulsive noise is studied either in real-life scenarios, or at the source, i.e., by isolating an appliance and studying the noise that it generates (cf. Section 1.4.3). In [38], the first approach is followed and the main focus is on the aperiodic noise

components for which the statistics of the amplitude, duration and inter-arrival time is provided. The statistics of the duration and the interarrival time is based on measurements in the time domain, that are performed by means of a DSO in peak detector mode. In [39], the authors deeply analyze the components of the BB power line noise. A time/frequency methodology to extract the periodic noise components is presented and validated with experimental measurements. A comprehensive model of the impulsive noise is also reported in [40].

Real-life measurement campaigns target the overall noise environment and they do not provide information about the noise generated by the specific device. In this respect, noise measurements at the source are required. In [41], the maximum value of the aperiodic noise amplitude is investigated for different devices. Interestingly, noise spikes of up to thousands of volts are experienced by switching ON/OFF the device. In [42], the same events lead to smaller amplitude, i.e., in the order of tens of Volts.

More recently, in [43], the periodic noise components is studied and modeled by means of deseasonalized autoregressive moving average, but no information is provided about the aperiodic noise components. Further analysis of the probability density function (PDF) of the amplitude are reported in [32] and [44] from measurements up to 30 MHz.

In this chapter, we characterize a broad set of devices that can be found in a house or office in terms of the impulsive noise components that they inject into the network. As for the characterization of the load impedances, we have investigated the behavior of common electrical appliances, i.e., a microwave oven, a desk lamp, a vacuum cleaner, a light dimmer, a number of desktop and laptop PCs, a flat monitor, a satellite TV decoder and a inject printer. Firstly, we focus on the periodic impulsive noise, both the asynchronous and the synchronous with the mains components. We follow the time/frequency domain approach in [39] and we apply the proposed methodology to the noise at the source measures that we have carried out. We aim to investigate the frequency range 2-100 MHz. Therefore, we study the asynchronous impulsive noise.

This chapter is organized as follows. In Section 4.2, we analyze the periodic impulsive noise, i.e., in terms of time variant PSD. Therefore, we distinguish the periodic impulsive noise components into asynchronous and synchronous with the mains contributions. Then, in Section 4.3, we characterize the maximum amplitude, the duration and the power of the asynchronous impulsive noise that is generated by the plugging in/out or ON/OFF switching activity of the devices under test. Finally, Section 4.4 summarizes the main findings.

4.2 Periodic Impulsive Noise

The noise acquisitions have been performed in the time domain. We have exploited the noise at the source setup explained in Section 1.4.3. In detail, we have connected the DSO closed to the DUT, i.e., the noise source, in combination with a PLF to suppress the noise

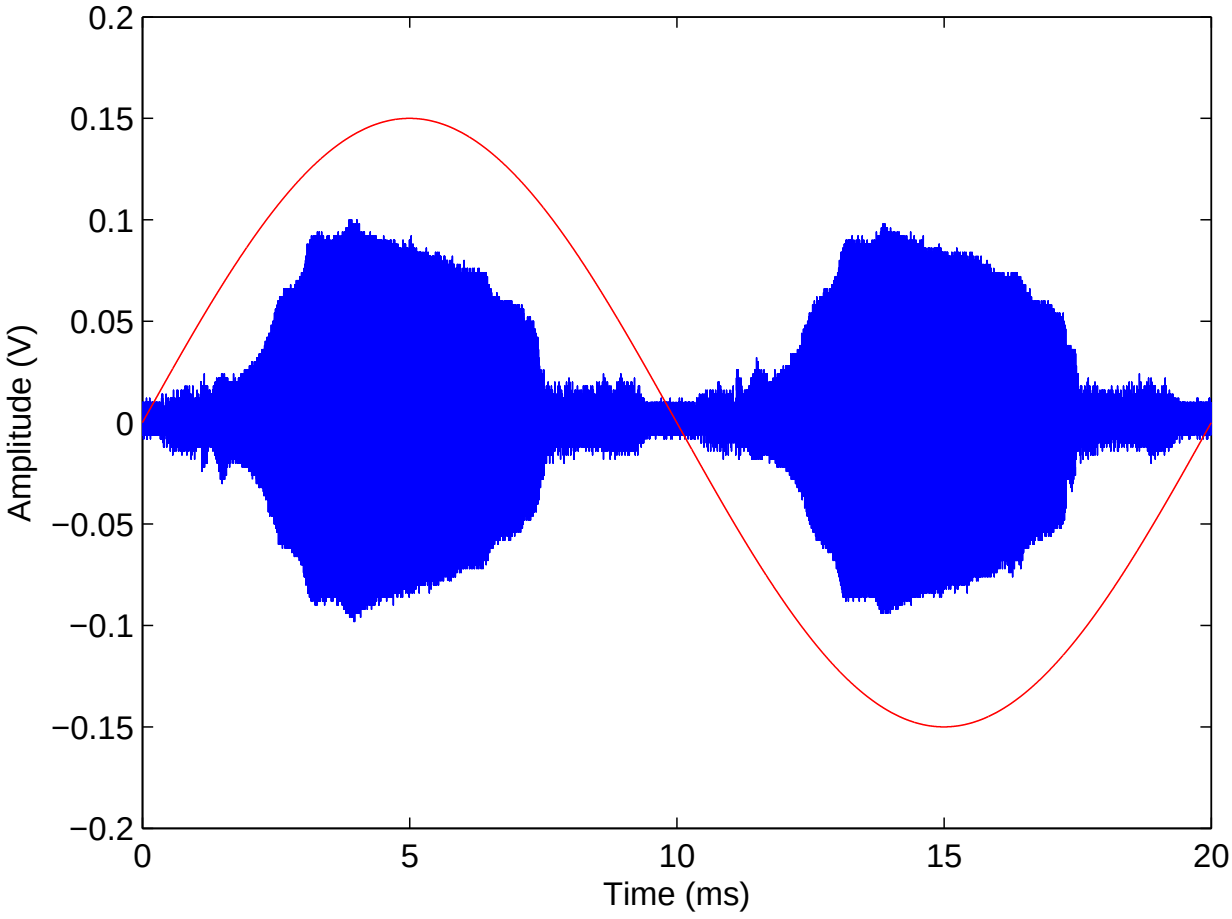

Figure 4.1: Acquisition of the noise of a desktop PC under test.

incoming from the power grid. The DSO has been provided with a 50 Ω input impedance adapter. We have triggered the DSO to the 50 Hz mains signal and we have fixed the time acquisition window equal to the mains period. Due to the time/frequency constraints of the DSO, we have set the number of measurement points equal to $K = 10^7$ in order to obtain a sampling frequency higher than 200 MHz, i.e., 500 MSa/s.

In Fig. 4.1, we show an acquisition of the noise of a desktop PC under test. We also plot the mains (scaled in amplitude) cycle to highlight the time variant behavior of the noise.

In the following, we describe the approach that we have used to analyze the noise in terms of time variant PSD, as in [39]. For each DUT, we have performed $C = 200$ subsequent measures. Thus, we have divided each noise acquisition into $I = 20$ intervals of duration $T_i = T_0/I$, where $T_0 = 20$ ms is the time acquisition window equal to the mains period. We have computed the periodogram of the measured noise in the i-th interval, for $i = 1, \ldots, I$, and we have averaged the C subsequent acquisition to obtain the PSD of the noise in the i-th interval. We have removed the effect of the coupler by subtracting (in dB scale) its frequency response to the PSD of the PLC noise.

For each DUT, we have adjusted the vertical setting of the DSO in order to avoid the

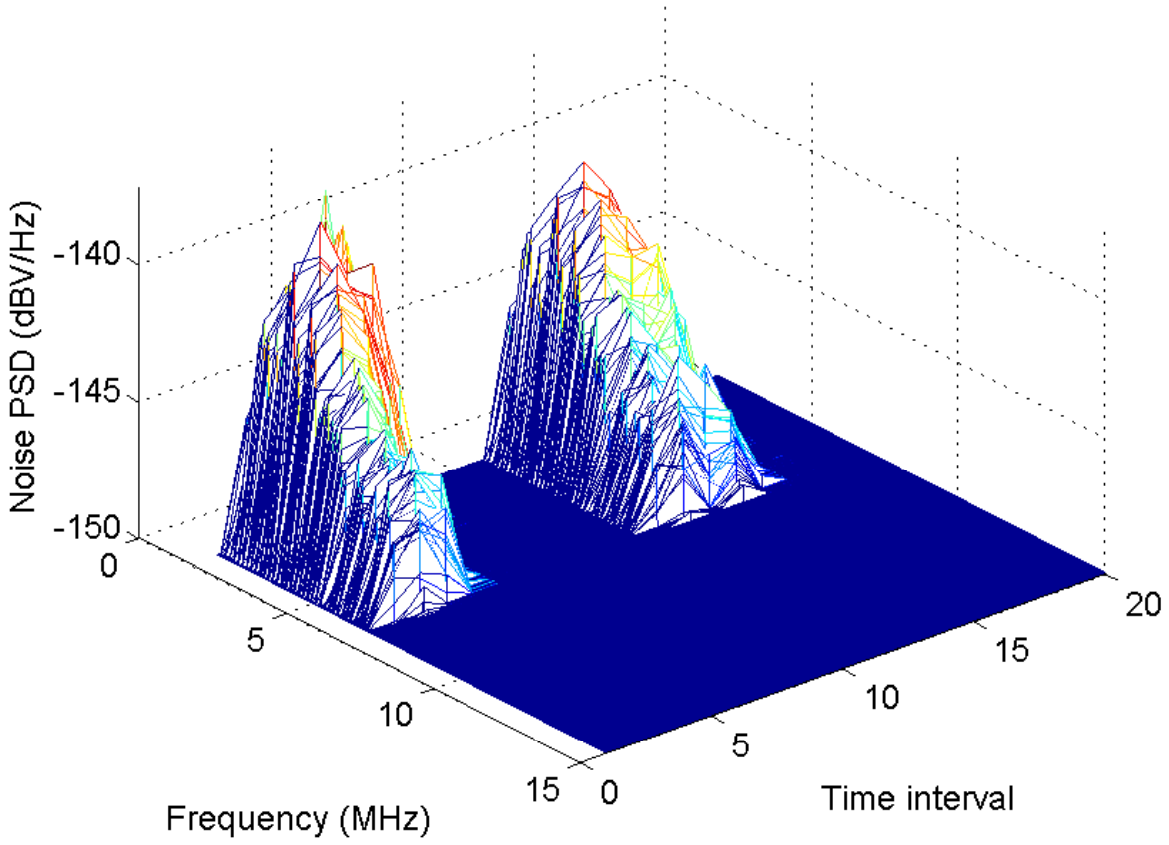

Figure 4.2: Time variant PSD of the printer under test.

clipping of the acquired noise waveform. Thus, we have measured the noise floor of the DSO and the contribute due to the power grid when the DUT was not connected. The effective PSD of the noise of the DUT has been obtained by subtracting the contribute due to the power grid and by bounding the resultant PSD to the noise floor of the DSO.

In Fig. 4.2, we show the time variant PSD of a printer. We limit the analysis on the band up to 15 MHz. In fact, we have experienced that the PSD exceeds the noise floor of the PSD below 15 MHz for all the DUTs. It follows that the main noise contributions interest the frequency range below 15 MHz. From Fig. 4.2, we observe that the peaks of the PSD occur with periodicity of 10 ms, i.e., 100 Hz.

Analyzing the time variant PSD of the DUTs, we have noted the following major aspects. First, the noisiet device, i.e., the devices that injects the highest levels of noise is a desktop PC, namely, an old desktop PC from different manufacturer w.r.t. the desktop PC of Fig 4.1. In fact, from Fig. 4.3-(a), we observe that the PSD achieves -110 dBV/Hz. Second, the desk lamp under test does not introduce noise above 2 MHz (Fig. 4.3-(b)).

Finally, we investigate the time variant PSD of the light dimmer under test. The PSD of the dimmer depends on its regulation. From Figs. 4.3-(c) and 4.3-(d), we note that

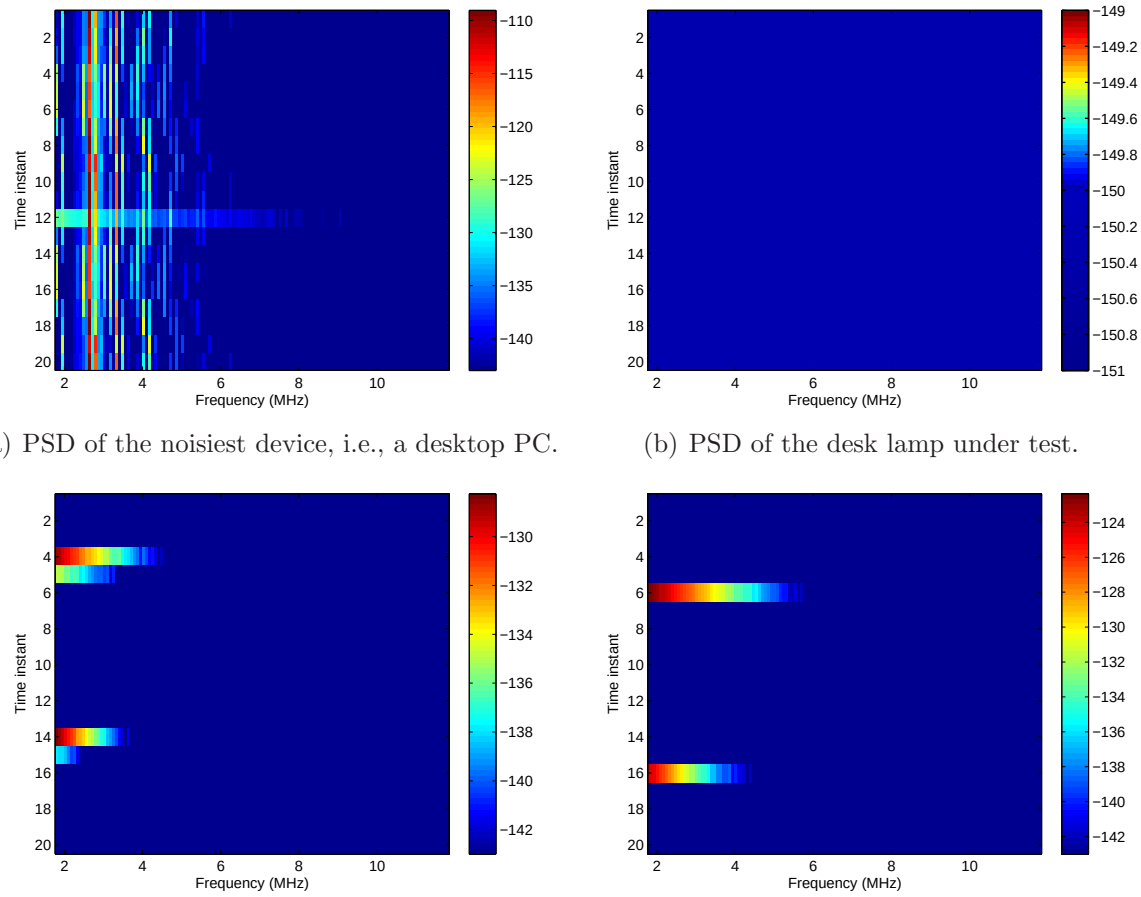

(a) PSD of the noisiest device, i.e., a desktop PC.

(b) PSD of the desk lamp under test.

(c) PSD of the dimmer under test (1/2 power).

(d) PSD of the dimmer under test (1/4 power).

Figure 4.3: PSD of three representative devices, i.e., a desktop PC, a desk lamp and a light dimmer.

the peaks of the PSD moves to different time-intervals, when the dimmer is configured to deliver half or a quarter of the total available power. Furthermore, the noise of the dimmer is concentrated in few time intervals and the maximum value is relatively low.

In the next sessions, we distinguish the noise components according to the classical classification reported in [39].

4.2.1 Periodic Impulsive Noise Asynchronous with the Mains

The periodic impulsive noise components asynchronous with the mains appear in the time variant PSD as frequency ripples and very narrow peaks [39]. The bandwidth of the peaks is determined by the specific window employed to compute the periodogram.

We process the measured PSD in order to identify such components. We identify the frequencies that correspond to the peaks of the noise PSD according an algorithm similar to the one that was firstly presented in [45]. In detail, for each time interval, we assume that a frequency sample is identified as a spectral peak if the PSD value at that frequency is

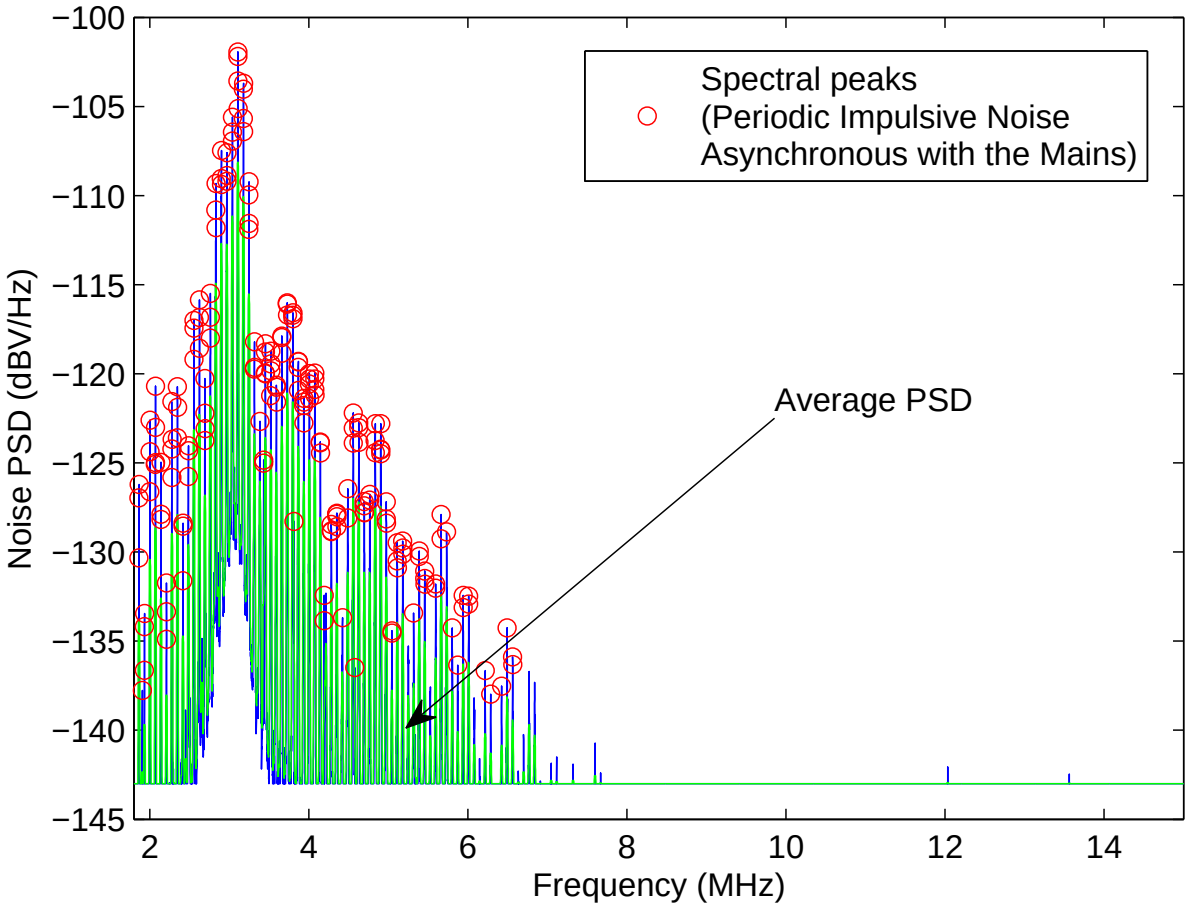

Figure 4.4: Noise PSD, average PSD and peaks associated to the periodic impulsive noise components asynchronous with the mains of the noisiest desktop PC at the time instant i=10.

two times greater than the average PSD in a narrow band around the considered frequency. In Fig. 4.4, we show the measured PSD of the noisiest device, i.e., the desktop PC of Fig. 4.3-(a), and the peaks identified by the aforementioned algorithm.

We have performed the mentioned analysis for all the devices. Thus, we have studied the probability function of the frequency samples that correspond to periodic impulsive noise asynchronous with the mains components. In Fig. 4.5, we show the PDF as a function of the frequency and the time interval. We note that the time-dependence of the PDF is negligible. Therefore, the components are concentrated below 6 MHz and they do not dependent on the time instant. Furthermore, the highest values are below 4 MHz.

4.2.2 Periodic Impulsive Noise Synchronous with the Mains

We start from the frequencies that correspond to the peaks of the periodic impulsive noise asynchronous with the mains. In the sub-bands where the peaks occur, the PSD value is substituted with the linear interpolation of the values of the PSD at the borders of the sub-

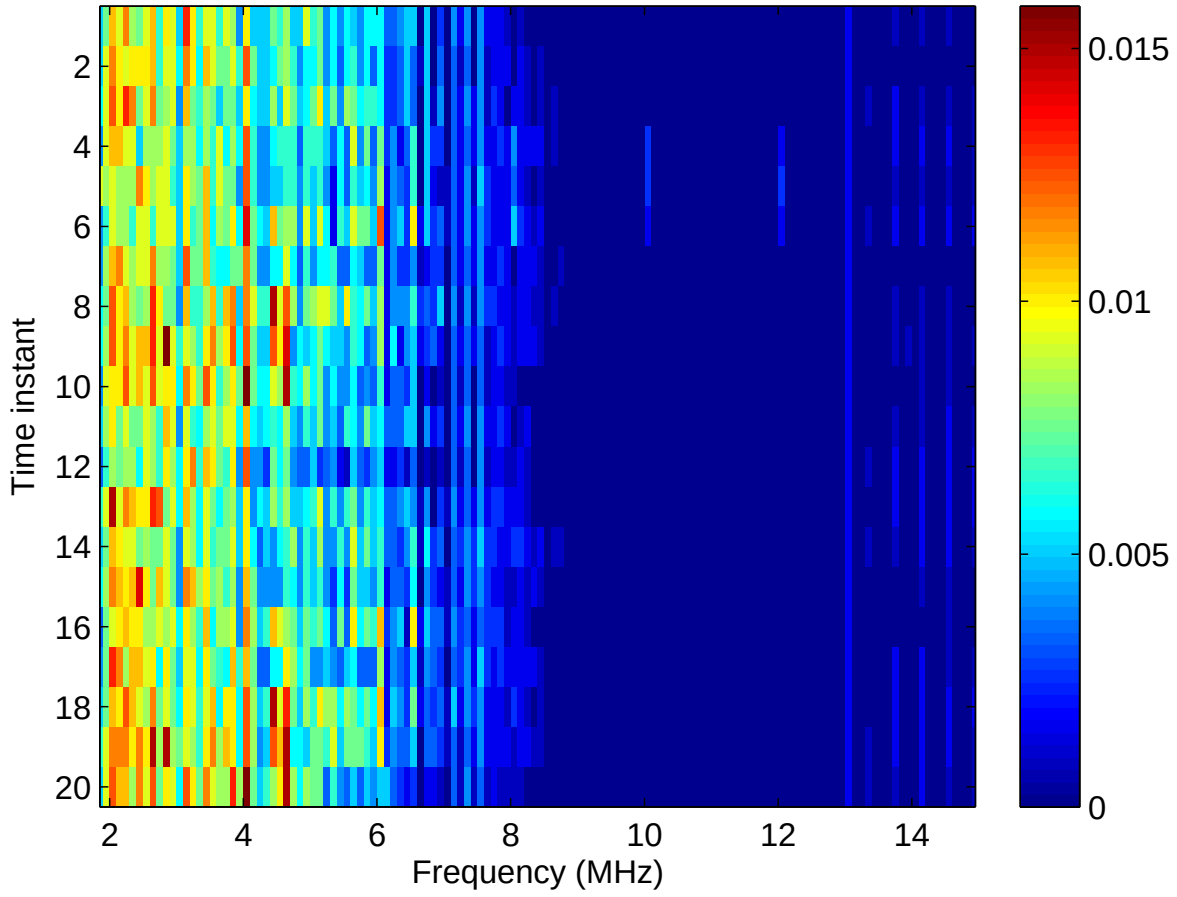

Figure 4.5: PDF of the frequency samples that correspond to periodic impulsive noise asynchronous with the mains components.

bands. In Fig. 4.6, we show the PSD and the "smoothed" PSD of the noisiest desktop PC under test, at the time interval i=3. We magnify the PSD in the 2-10 MHz frequency range, i.e., where the periodic impulsive asynchronous with the mains contribution is more evident.

Now, we focus on the time variations of the periodic impulsive noise synchronous with the mains component. From experimental observations, we note the following. First, the resultant PSD is not white and the highest values are concentrated in the lower frequency range. Second, it exhibits a clear time variant and periodic behavior with a repetition rate equal to 100 Hz, as expected. These findings apply to most of the measured devices.

To provide an overview of the measurements, we study the maximum value of the estimated PSD among the full set of measured devices. In Fig. 4.7, we show the results. We note that above 10 MHz, we do not experience cyclostationary noise. Furthermore, the maximum value is equal to -110 dBV/Hz, i.e., the noise injected by the desktop PC under test of Fig. 4.1 and Fig. 4.3-(a).

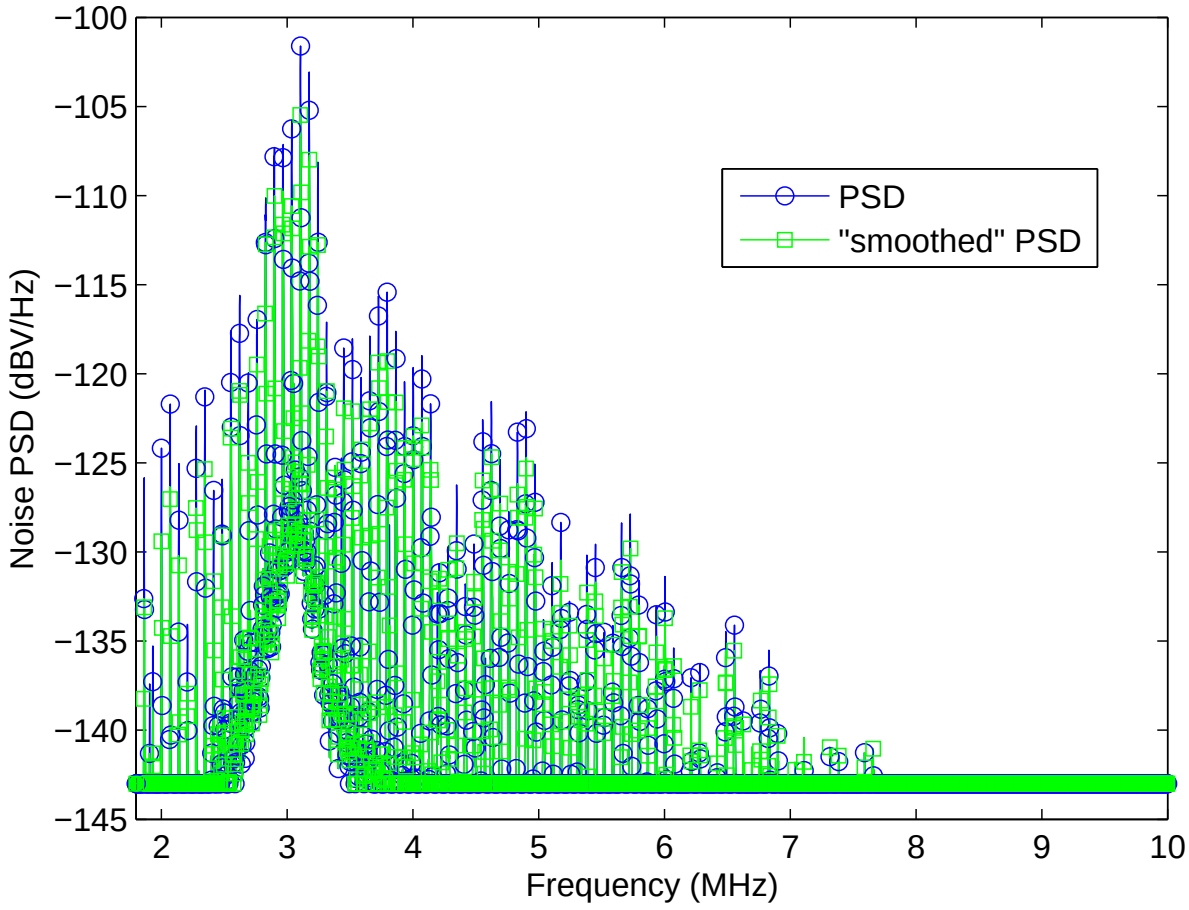

Figure 4.6: PSD and "smoothed" PSD of the noisiest desktop PC under test, at the time interval i=3.

4.3 Asynchronous Impulsive Noise

Plugging in/out or switching ON/OFF the devices may generate electric arcs that lead to noise spikes. In this section, we characterize the maximum amplitude, the duration and the power of the asynchronous impulsive noise that is generated by the devices mentioned above.

We have performed measurements in the time domain. We have triggered the DSO to the acquired signal, and we have set the trigger level to 200 mV. The trigger level has been chosen high enough to avoid acquiring the periodic impulsive noise. We have performed measurements with sampling frequency equal to 250 MHz and we have varied the number of measurement points K to obtain the shortest acquisition in time that contains the noise spikes due to the plugging in/out, switching ON/OFF of the DUTs. Furthermore, we have adjusted the vertical settings of the DSO to ensure the highest signal resolution in amplitude. In this respect, we have tolerated the clipping of the waveform when their amplitude exceeded slightly the maximum amplitude that the DSO was able to acquire according to the configuration.

In Table 4.1, we summarize the main characteristics of the measured asynchronous im-

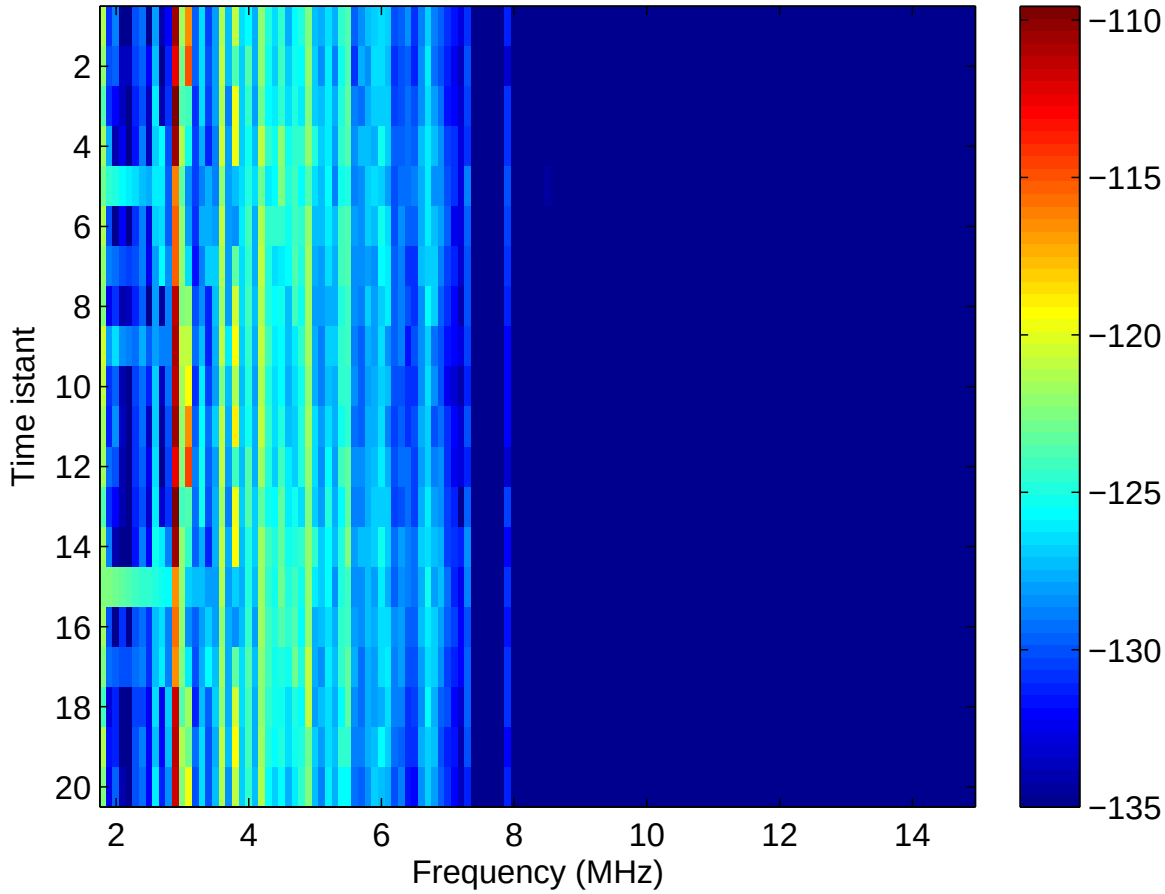

Figure 4.7: Maximum value of the estimated PSD among the full set of measured devices.

pulsive noise.

The maximum amplitude ranges from 2 V to 50 V[1] and the noisiest event is the plug in. In fact, all devices generate noise spikes greater than the threshold and that may even exceed 50 V. Conversely, only few devices generate noise spikes for a plug out event. Therefore, the ON/OFF switching activity is particularly noisy for the desk lamp and the vacuum cleaner under test. They inject high noise spikes, as depicted in Fig. 4.8 and Fig. 4.9. Also the light dimmer generates noise on switch ON, but with lower values, namely, 6 V. All other devices do not exceed the trigger threshold.

The duration of the noise spikes is defined as the time distance between the first time instant and the last time instant for which the absolute value of the noise exceeds ϵ times the maximum. We used $\epsilon = 1/\sqrt{10}$. Thus, in Table 4.1, we report the range of values of the minimum, mean and maximum duration of the noise spiked, for all the devices and events. From measures, we have found that the duration varies significantly, even for noise waveforms generated by the same device and there is no clear indication about its behavior.

Finally, we provide a description of the intensity of the asynchronous impulsive noise

[1]Beyond 50 V, the acquisition is clipped.

Table 4.1: Main Characteristics of the Measured Asynchronous Impulsive Noise.

Parameter	Value
Noisiest event	Plug in
Maximum amplitude	from 2 V to 50 V[1]
Duration (min)	from 0.004 μs to 354 μs
(avg)	from 0.04 μs to 1.3 ms
(max)	from 2.1 μs to 3.4 ms
Power (min)	from 0.08 mW to 1.2 W
(avg)	from 0.44 mW to 6.7 W
(max)	from 0.9 mW to 250 W

spikes. Thus, we study the instantaneous power, i.e., the power of the noise spike of duration as defined before, delivered to a 50 Ω load. On average, the power can be significantly high. Nevertheless, it refers to noise spikes with very short duration in time, i.e., less than 0.2 μs.

4.4 Main Findings

In this chapter, we have characterized a broad set of electrical appliances connected to the home/office power grid in terms of the impulsive noise components that they inject into the network. We have performed noise at the source measurements in order to deeply characterize the noise injected by any single appliance.

We have found that, beyond 15 MHz, the devices do not inject noise. The periodic impulsive asynchronous with the mains components are concentrated below 6 MHz and they do not dependent on the time instant. Instead, the synchronous with the mains components cyclically vary with a repetition rate of 100 Hz.

Finally, we have targeted the asynchronous impulsive noise. We have measured noise spikes greater than 50 V that lasts up to 4 ms.

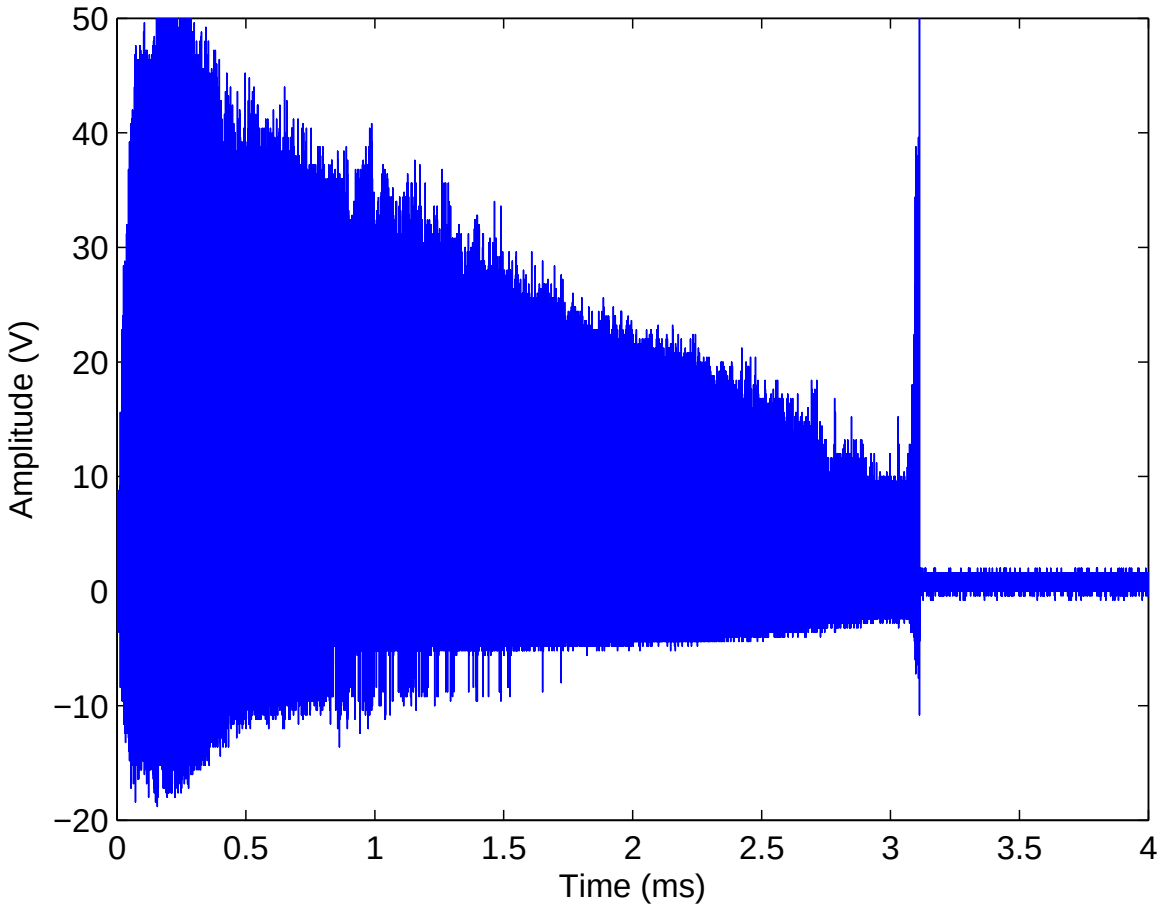

Figure 4.8: Aperiodic impulsive noise of the desk lamp during switch OFF.

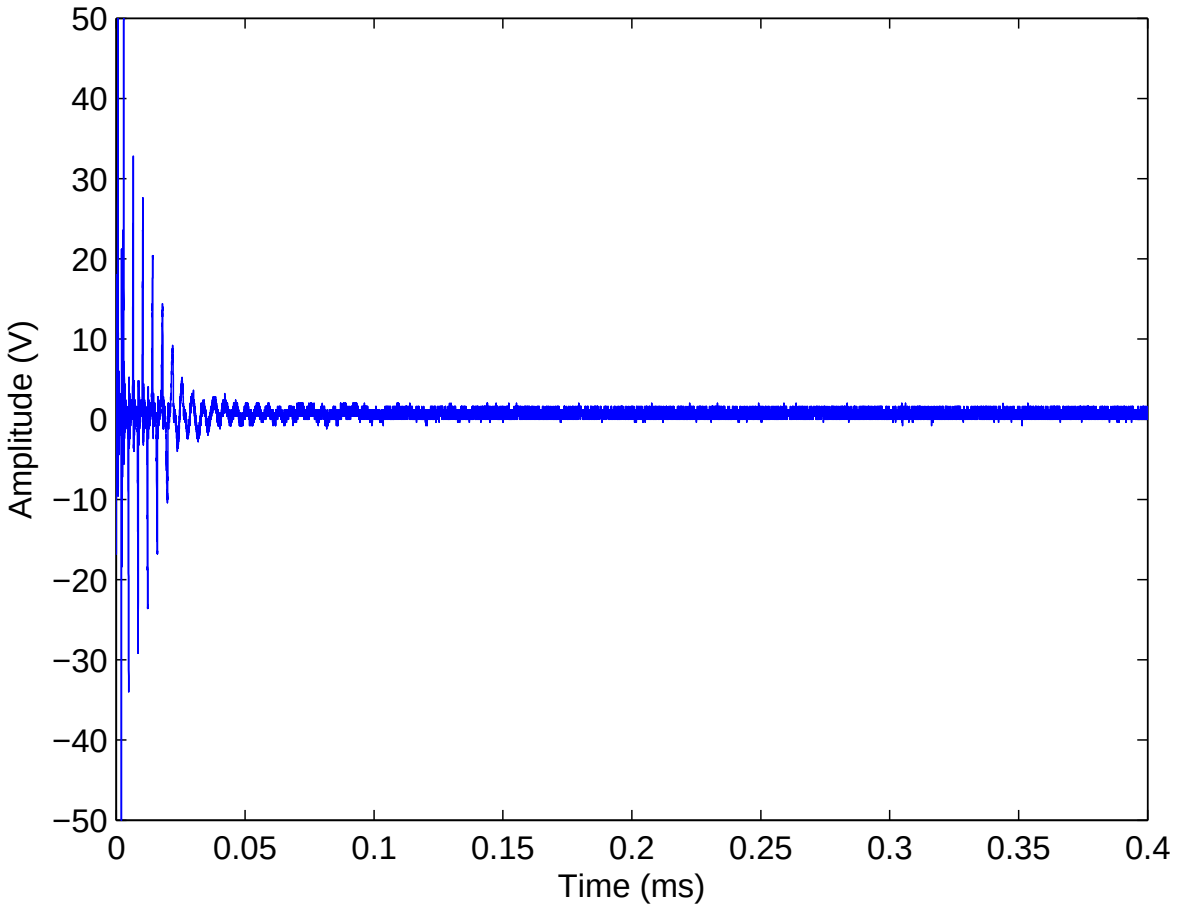

Figure 4.9: Aperiodic impulsive noise of the vacuum cleaner during switch ON.

Chapter 5

In-ship PLC

Power line channel measurements and analysis in a cruise ship is the topic of this chapter. Herein, we summarize the results of a channel measurement campaign that we have carried out in the LV distribution network of a large cruise ship.

Applications and benefits that the deployment of power line communication in a ship environment can bring, justify research initiatives targeting the study of channel characteristics.

5.1 Introduction

In this chapter, we consider in-ship PLC which can provide significant benefits as the delivery of high speed communication services and the support of low speed command and control application without the need of dedicated cabling. Thus, it has the potential of simplifying the design of the communication network and more importantly saving weight and cost. In a typical cruise ship, 23% of the weight of the electrical system (3900 tonnes) is due to at least 30000 cables, for an overall length of 2400 km. Since the cruise ship is intrinsically a hotel and entertainment structure for passengers, multimedia services are of great interest. PLC can exploit the existing power distribution infrastructure to deliver high speed services to every cabin or to every deck [46].

For the proper design of a power line communication system, good knowledge of the channel characteristics is required. Only few papers deal with the characterization of in-ship PLC channels. In [47], the authors present a theoretical and experimental analysis on the application of PLC on a cruise ship developing a model based on a theoretical approach (in the band 0-12.5 MHz). In [48], the transfer function of a 440 V power line network in a container ship was measured and modeled in the frequency range 2-30 MHz. The characterization of the channels in training ships was reported in [49], while the study of unintentional radiations by PLC in ships and shipboard cables characteristics were the subjects of [50, 51]. Testing of HomePlug 1.0 compatible PLC modems in a cruise ship was conducting in [52].

In this respect, we have carried out a channel measurement campaign in the LV power

distribution network of housing and public areas of a large cruise ship, in the band 0-50 MHz. The data have been used to study the statistics of the channel, and in particular, of the average channel gain (ACG), root mean square delay spread (RMS-DS), coherence bandwidth (BC). Furthermore, we address the analysis of theoretical capacity in the band 2-28 MHz (used by state-of-the art Homeplug AV compliant PLC technology [7]) and in the band 2-50 MHz. Furthermore, the presence of three phase power distribution allows the exploitation of multiple-input multiple-output (MIMO) transmission. Thus, the capacity of the 2x2 MIMO channel is also investigated.

The chapter is organized as follows. Section 5.2 describes the cruise ship under test and the power distribution system. Section 5.3 explains the measurement setup and scenario. In Section 5.4, we deal with the statistical analysis of the channel, providing results in terms of path loss, average channel gain, RMS delay spread, coherence bandwidth and link capacity. The effect of circuit breakers is briefly discussed in Section 5.5. Finally, Section 5.6 summarizes the main findings.

5.2 Ship Under Test and Power Distribution System

The measurement campaign has been done in a 116000 tonnes cruise ship built by Fincantieri Cantieri Navali S.p.A. (Fig. 5.1). The electrical power generation and distribution system has been developed to satisfy the power needs of the electrical engines, lighting, in addition to all systems that have to guarantee correct functioning of hotel and entertainment structures. The power generation is ensured by asynchronous alternators moved by diesel engines. The generated MV power (at 11 kV, 60 Hz) is first distributed to 9 MV/LV substations where it gets transformed in LV (690-440-220-115 V depending on the application). The LV electric power distribution system is a three-phase system with “insulated” and not distributed neutral.

As most of similar ships, our test ship is horizontally divided into two main areas: the engine areas located in lower decks, and housing and public areas that span 14 decks. Both areas are also vertically divided. In particular, the housing and public areas are divided in fire zones by fire-resistant bulkheads. Each fire zone owns a MV/LV substation located on a deck beyond the decks of the engine zone. Power is distributed vertically from the switchboard of the substation to all decks of the same fire-zone reaching a number of distribution boards. Each single phase armored power cable has variable section depending on the fact that it is used for the 220 V or the 115 V system. The cable properties are summarized in Table 5.1. Thus, each group of three armored power cables feeding each distribution board is outer sheathed in PVC.

Every distribution board is then connected by a bus-bar to a number of room service panels that serve a small number of rooms each.

Figure 5.1: Picture of the cruise ship under test.

5.3 Measurement Setup and Scenario

Channel measurements have been made in the time domain using a WG and a DSO with 50 Ω input impedance with sampling rate $F_s = 200$ Msamples/s. This realizes a single-input single-output (SISO) transmission since both the transmitter and the receiver are connected to test outlets between a pair of conductors. The capacitive coupler that we used has an almost flat frequency response up to about 50 MHz. The CTF up to 50 MHz has been obtained via DFT with a frequency step size of 100 kHz, i.e., processing channel responses of length 10 μs.

Giving the complexity and extension of the power line network in the test ship, we have divided the measurements in two sections as depicted in Fig. 5.2. The first section comprises the power line segment between a selected substation and a certain distribution board. The second section comprises the power line segment between the distribution board and a certain room service panel located in the same deck. We have selected one reference substation (among the 9 present in the test ship), that is located on deck n°4 and in fire-zone n°6. This substation is located in a barycentric position and it is representative of the others

Table 5.1: Measurement scenario cable properties.

Distribution board	Deck	Length [m]	Section [mm^2]
XD9000 (220 V)	8	83	70
XDB000 (220 V)	10	79	70
EP8000 (115 V)	10	84	50
XDE000 (220 V)	14	95	70

in terms of wirings and topology of the housing and public areas. The switchboard of the selected substation supplies 45 distribution boards of the 220 V system, and 15 distribution boards of the 115 V system. Among all distribution boards, we have selected one located on deck n°8, two on deck n°10 (one for the 220 V system and one for the 115 V system) and another one on deck n°14. Finally, for each distribution board, we have selected one room service panel. The connection of the distribution board with the room service panel is realized by a bus-bar.

Being the LV electric power distribution system a three-phase system with "insulated" and not distributed neutral, the direct and return channel have been realized by signaling on two phase wires. Since there are three available conductors (denoted with R, S, and T), two physical channels can be established. Thus, it is in principle possible to implement a 2x2 MIMO transmission. Consequently, we have measured both the direct channel and the coupled channel placing couplers both between the R and T conductors (RT) and between the S and T conductors (ST).

The substation switchboard, distribution boards and room service panels have a primary panel circuit breaker and a number of secondary circuit breakers equal to respectively the number of distribution boards, room service panels, and rooms connected to them. In the substation switchboard we have placed test points after the secondary circuit breakers (labeled with RT ST (2) in Fig. 5.2). In the distribution board, we have placed test points at the input of the the primary circuit breaker, at the output of it, and at the output of the secondary circuit breaker (labeled respectively with RT ST, RT ST (1) and RT ST (2) in Fig. 5.2). In the room panel we have placed the test point at the input of the primary circuit breaker.

5.4 Statistical Analysis

To ease the notation and for clarity, we denote with SS-DB the connection of the substation switchboard with the distribution boards, while with DB-RP the connection between the distribution boards and the room service panels. The statistical analysis of data is done in the band 0-50 MHz, unless differently specified.

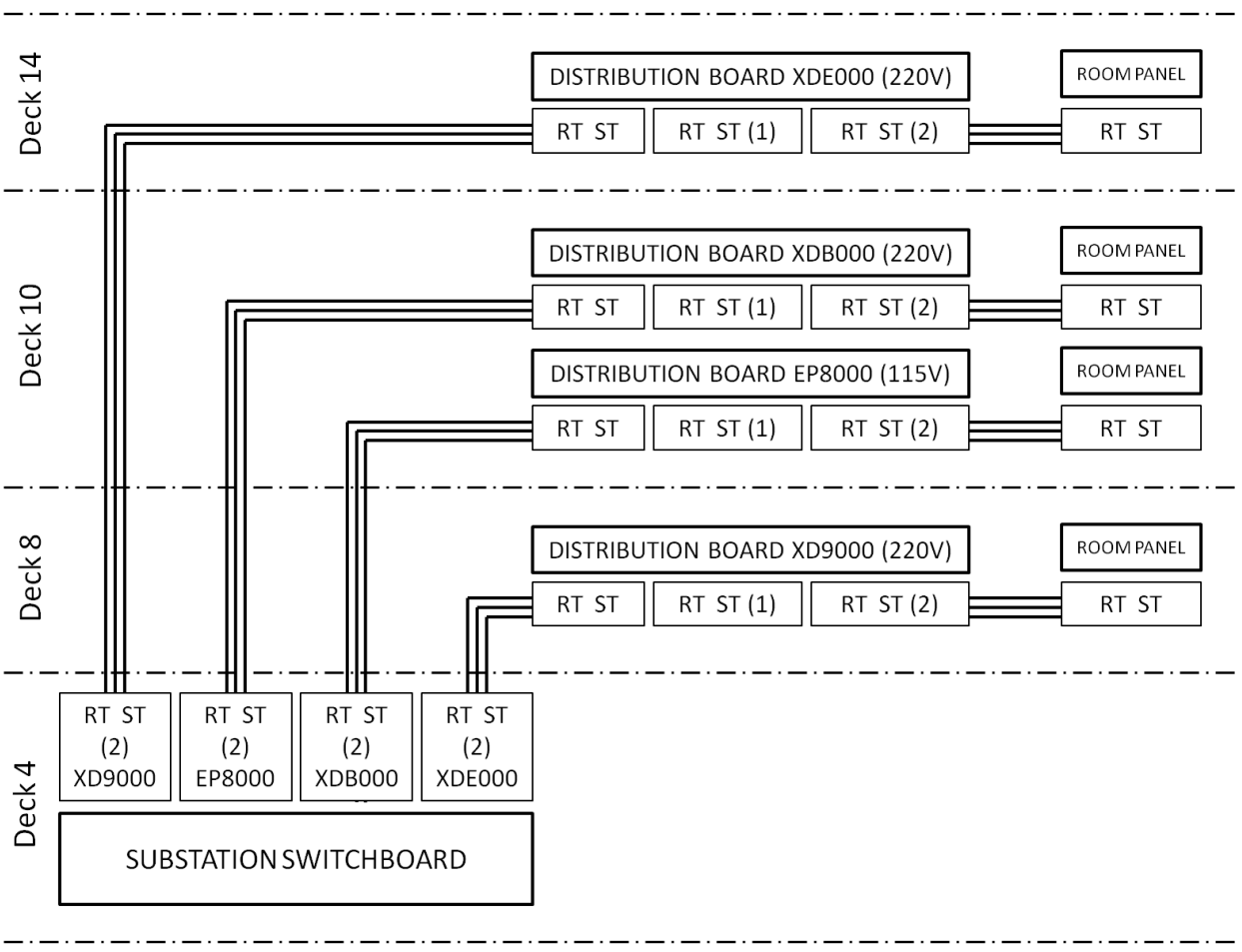

Figure 5.2: Measurement scenario. RT and ST denotes test points with a coupler connected to R and T phases or between S and T phases. RT ST, RT ST (1) and RT ST (2) denote respectively test points at the input of the primary circuit breaker, at the output of it, and at the output of the secondary circuit breaker, respectively.

5.4.1 Path Loss

We provide results firstly in terms of PL (see Section 2.4.1) that is defined as $PL(f) = |H(f)|^2$ and its version in dB as $PL_{|dB}(f) = 10\log_{10}(|H(f)|^2)$ where $H(f) = H_{(TX,RX)}(f)$ is the CTF between the transmitter TX and the receiver RX with $TX, RX \in \{RT, ST\}$ depending on the phases involved in the link.

In Fig. 5.3, we show the 50-th percentile of the PL in dB scale over all measured links as function of frequency. In subplot (a), we report results for the SS-DB links, while in subplot (b), for the DB-RP links. The direct channels, i.e., (RT, RT) or (ST, ST), are with solid lines, while the coupled channels, i.e., (RT, ST) or (ST, RT), are with dashed lines. The figure shows that the frequency dependence and attenuation is more significant for the DB-RP links due to larger presence of branches and discontinuities and related impedance mismatches. Furthermore, the PL of the direct and coupled channels for the DB-RP links are similar. We speculate that this behavior is due to the bus-bar system topology.

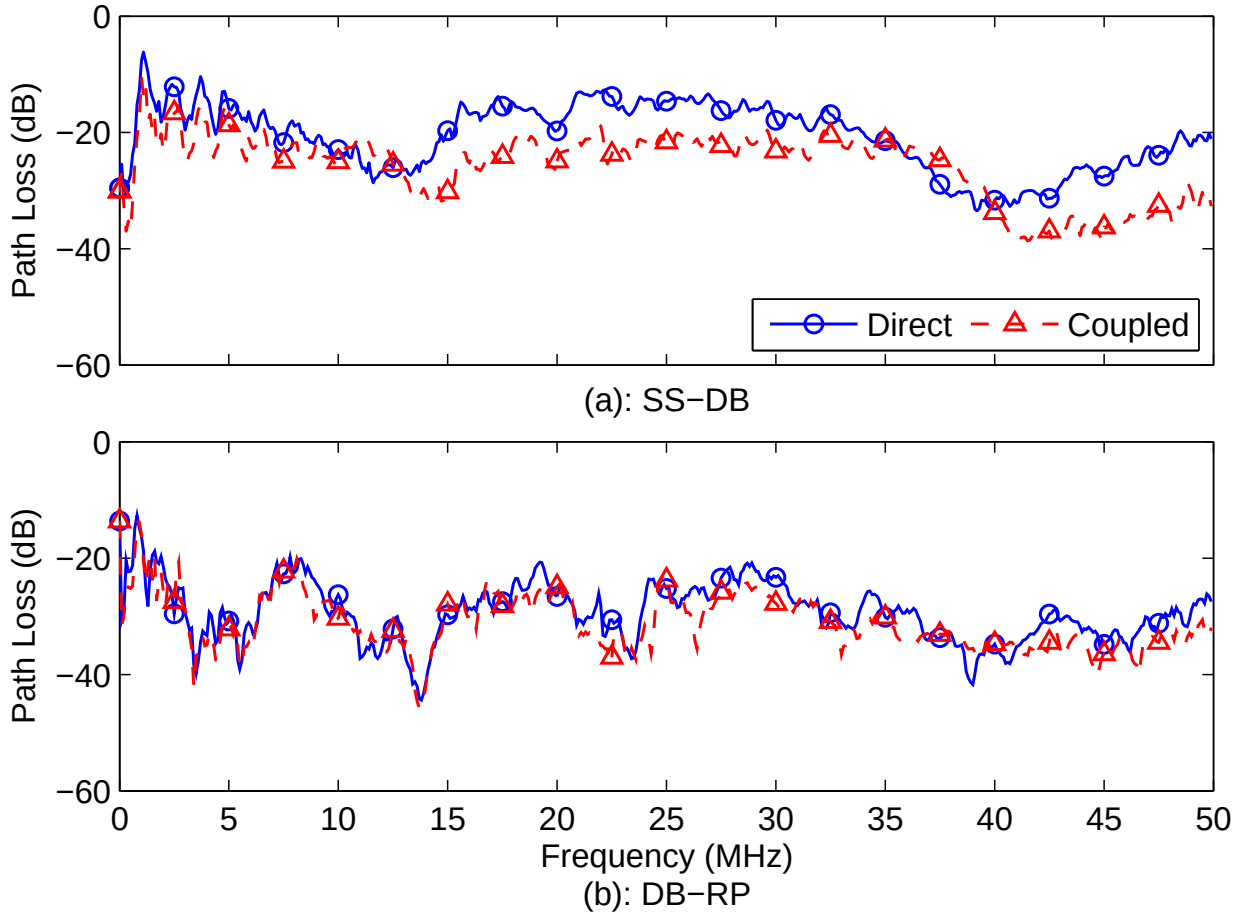

Figure 5.3: 50-th percentile of PL of the SS-DB links in subplot (a), and DB-RP in subplot (b). Solid curves refer to direct links, dashed curves to coupled ones.

5.4.2 Average Channel Gain

The ACG is computed by averaging the PL as follows

$$ACG = \frac{1}{N}\sum_{n=0}^{N-1}\left|H\left(\frac{n}{NT_s}\right)\right|^2 = \sum_{n=0}^{N-1}\left|h\left(nT_s\right)\right|^2 \tag{5.1}$$

where $H\left(n/NT_s\right)$ is the CTF obtained as the N-points DFT of the impulse response $h\left(nT_s\right)$ sampled at rate $F_s = 1/T_s = 200$ MHz, $T_s = 5$ ns is the sampling time resolution, and $N = 2000$ is the number of impulse response points. The ACG in dB scale is defined as $ACG_{|dB} = 10\log_{10}(ACG)$. In Table 5.2, we report the minimum value, the maximum value, the mean, and the standard deviation of the $ACG_{|dB}$ for the SS-DB links and for the DB-RP links (direct, coupled, and all together). In Fig. 5.4, we report the quantile-quantile plots of the $ACG_{|dB}$ for the SS-DB links (subplot (a1)) and for the DB-RP links (subplot (b1)), to test the normality of the distribution function of the $ACG_{|dB}$. These curves report the measured samples against a similar number of quantiles taken from a normal distribution.

Table 5.2: Statistical values of measured ACG in dB.

$ACG_{\|dB}$	Min	Max	Mean	Std deviation
SS-DB direct	-29.29	-13.99	-20.0116	4.50
SS-DB coupled	-31.31	-20.57	-25.06	3.54
SS-DB	-31.31	-13.95	**-22.54**	**4.74**
DB-RP direct	-36.88	-9.47	-24.80	6.84
DB-RP coupled	-39.65	-12.84	-27.54	6.56
DB-RP	-39.65	-9.48	**-26.17**	**6.78**

Table 5.3: Statistical values of measured RMS-DS in μs.

$\sigma_{\tau\|\mu s}$	Min	Max	Mean	Std deviation
SS-DB direct	0.22	0.97	0.54	0.21
SS-DB coupled	0.33	1.05	0.68	0.22
SS-DB	0.22	1.05	**0.61**	**0.22**
DB-RP direct	0.24	1.20	0.69	0.25
DB-RP coupled	0.43	1.55	0.83	0.33
DB-RP	0.24	1.55	**0.76**	**0.30**

If the samples are drawn from a normal distribution, the curve will be linear. The figure proves that the ACG in dB is normal.

In the subplots (a2) and (b2) of Fig. 5.4, we show the cumulative distribution function (CDF) of the $ACG_{|dB}$ for the SS-DB and DB-RP links (direct and coupled ones all together) compared to CDFs of two random variables normally distributed with mean and standard deviation reported in Table 5.2 (bold values).

It follows, that the ACG (in linear scale) is lognormally distributed with good approximation. The same distribution has been found in the analysis of PLC channels of the in-home scenario [34, 53, 54].

5.4.3 RMS Delay Spread

The RMS-DS is the square root of the second central moment of the power-delay profile, defined as follows

$$\sigma_\tau = \sqrt{\mu_\tau'' - \mu_\tau^2} \tag{5.2}$$

with

$$\mu_\tau = \frac{\sum_{n=0}^{N-1} nT_s \left|h\left(nT_s\right)\right|^2}{\sum_{n=0}^{N-1} \left|h\left(nT_s\right)\right|^2} \quad \mu_\tau'' = \frac{\sum_{n=0}^{N-1} (nT_s)^2 \left|h\left(nT_s\right)\right|^2}{\sum_{n=0}^{N-1} \left|h\left(nT_s\right)\right|^2}. \tag{5.3}$$

It is used to measure the multipath spread and characterize the effect of channel dispersion on a transceiver. In the following, we denote the RMS-DS in μs as $\sigma_{\tau|\mu s}$. In Table 5.3, we

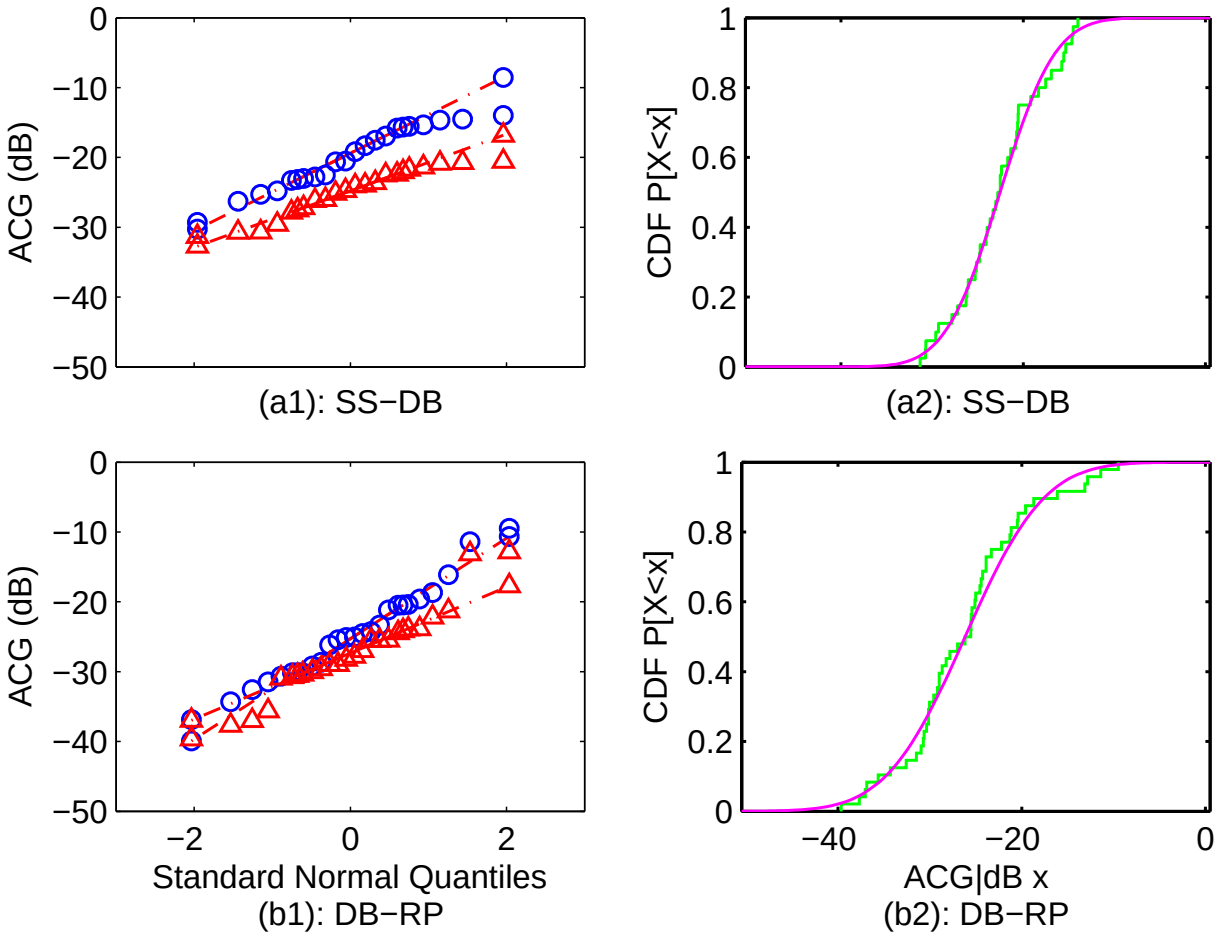

Figure 5.4: (a1), (b1): Quantile-quantile plots of $ACG_{|dB}$ of the SS-DB and DB-RP channels. Direct links with blue circled markers, coupled links with triangular red markers. (a2), (b2): CDF of $ACG_{|dB}$ of the SS-DB and DB-RP channels.

report the minimum value, the maximum value, the mean, and the standard deviation of $\sigma_{\tau|\mu s}$. The RMS-DS can be considered lognormal distributed with good approximation as the linear trend in the quantile-quantile plots of its logarithmic version in Fig. 5.5 (a1) and (b1) show.

The CDFs of the RMS-DS of SS-DB and DB-RP channels are reported in Fig. 5.5-(a2) and Fig. 5.5-(b2). They are compared to the CDFs of two lognormal distributed random variables with mean and standard deviation reported in Table 5.3 (bold values).

We now investigate the relationship between the RMS-DS and the ACG. The RMS-DS and the ACG are negatively correlated. Therefore, channels with large RMS delay spread are also characterized by small average channel gain (large attenuation) [53]. Fig. 5.6 shows a scatter plot of $\sigma_{\tau|\mu s}$ versus $ACG_{|dB}$, and the trend line evaluated by minimizing the mean square error between the trend line and the observed values.

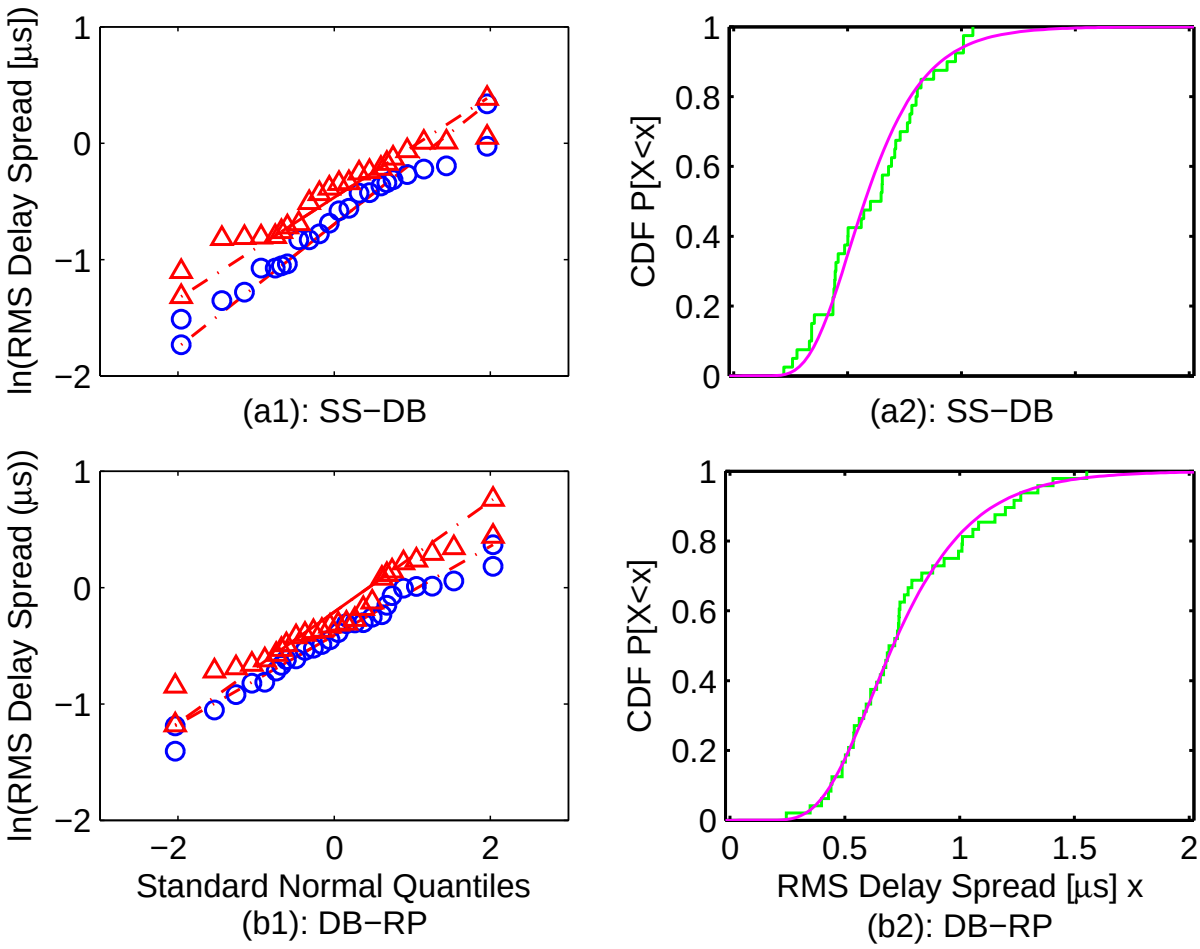

Figure 5.5: (a1), (b1): Quantile-quantile plots of $\ln(\sigma_{\tau|\mu s})$ of the SS-DB and DB-RP channels. Direct channels are marked with blue circles, while coupled channels with red triangles. (a2), (b2): CDFs of $\sigma_{\tau|\mu s}$ of SS-DB and DB-RP channels.

The relations of the trend line are

$$\sigma_{\tau|\mu s}^{(SS-DB)} = -0.0274\, ACG_{|dB}^{(SS-DB)} \tag{5.4}$$

$$\sigma_{\tau|\mu s}^{(DB-RP)} = -0.0287\, ACG_{|dB}^{(DB-RP)}. \tag{5.5}$$

Circled data points belong to the measurements of direct links, triangular ones belong to the coupled links. The scatter plot shows that SS-DB channels are characterized by $\sigma_{\tau|\mu s}$ and $ACG_{|dB}$ values concentrated around the mean values, while for DB-RP channels the values are more spread. The correlation coefficient between $\sigma_{\tau|\mu s}^{(SS-DB)}$ and $ACG_{|dB}^{(SS-DB)}$ is -0.64, while between $\sigma_{\tau|\mu s}^{(DB-RP)}$ and $ACG_{|dB}^{(DB-RP)}$ is - 0.51 .

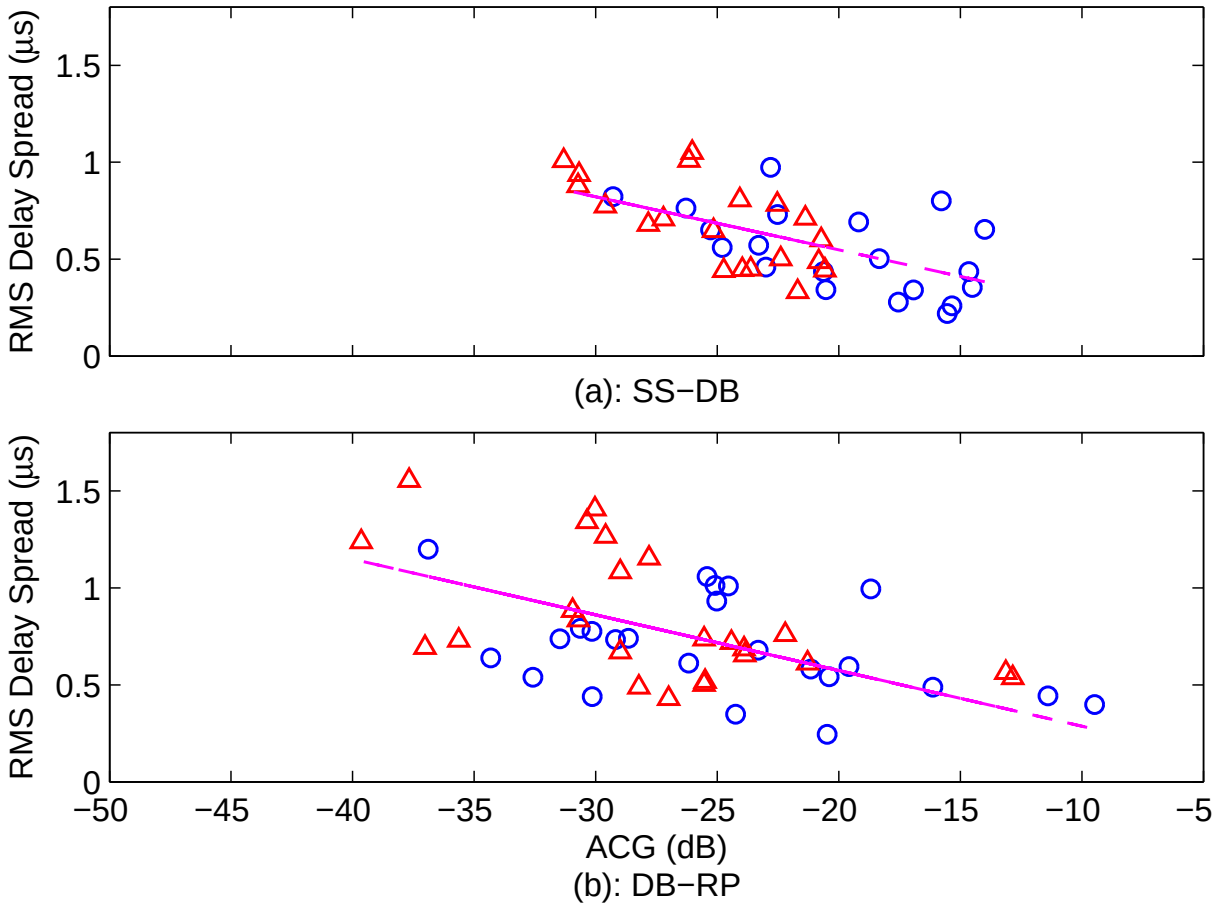

Figure 5.6: Scatter plot of $\sigma_{\tau|\mu s}$ versus $ACG_{|dB}$ and evaluated trend line for the SS-DB and DB-RP channels. Direct realizations are marked with blue circles, while coupled channels with red triangular markers.

5.4.4 Coherence Bandwidth

The frequency selective behavior of the channel can be analyzed in terms of the autocorrelation function (ACF) of the frequency response that is defined as

$$R(\Delta f) = \int_B H(f)H^*(f + \Delta f)df \tag{5.6}$$

where * denotes the complex conjugate, Δf is the frequency shift and $B = [0\ 50]$ MHz is the channel band.

The BC is a statistical measure of the range of frequencies over which two frequency components of the channel have a generally accepted value of correlation, e.g., equal to 0.9 and 0.7.

In Tables 5.4 and 5.5, we report the coherence bandwidth statistical values for all measured channels with a correlation index equal to 0.9 and 0.7. Quantities are in kHz scale.

In Fig. 5.7, we show the scatter plots of the RMS-DS versus the coherence bandwidth

Table 5.4: Statistical values of measured Coherence Bandwidths $BC_{0.9}$ in kHz.

$BC_{0.9\|kHz}$	Min	Max	Mean	Std deviation
SS-DB direct	70	1290	344.50	405
SS-DB coupled	60	320	152	77.64
SS-DB	60	1290	**248.25**	**303.89**
DB-RP direct	40	410	149.17	107.25
DB-RP coupled	20	240	111.67	64.25
DB-RP	20	410	**130.42**	**89.49**

Table 5.5: Statistical values of measured Coherence Bandwidths $BC_{0.7}$ in kHz.

$BC_{0.7\|kHz}$	Min	Max	Mean	Std deviation
SS-DB direct	230	4390	2012	1652.40
SS-DB coupled	190	3110	1374	1198.10
SS-DB	190	4390	**1693**	**1460.8**
DB-RP direct	130	2520	517.08	561.42
DB-RP coupled	80	940	377.08	244.37
DB-RP	80	2520	**447.08**	**434.13**

$BC_{0.9|kHz}$ and $BC_{0.7|kHz}$, respectively for SS-DB channels ((a1) and (a2) subplots), and DB-RP ones ((b1) and (b2) subplots). The relations between $\sigma_{\tau|\mu s}$ and $BC_{0.9|kHz}$ and $BC_{0.7|kHz}$ can be approximated as hyperbolic relations. By fitting the simulation results, we propose the following relations, obtained minimizing the mean square error between the trend lines and the observed values

$$\sigma_{\tau|\mu s}^{(SS-DB)} = \frac{74}{BC_{0.9|kHz}^{(SS-DB)}} \tag{5.7}$$

$$\sigma_{\tau|\mu s}^{(SS-DB)} = \frac{236}{BC_{0.7|kHz}^{(SS-DB)}} \tag{5.8}$$

$$\sigma_{\tau|\mu s}^{(DB-RP)} = \frac{51}{BC_{0.9|kHz}^{(DB-RP)}} \tag{5.9}$$

$$\sigma_{\tau|\mu s}^{(DB-RP)} = \frac{180}{BC_{0.7|kHz}^{(DB-RP)}}. \tag{5.10}$$

5.4.5 Capacity

In this section, we evaluate the potential transmission performance in terms of link capacity C in the Home Plug AV frequency band [7] 2-28 MHz and in the band 2-50 MHz under the assumption of a transmitted signal PSD $P_{tx} = -50$ dBm/Hz and white Gaussian background

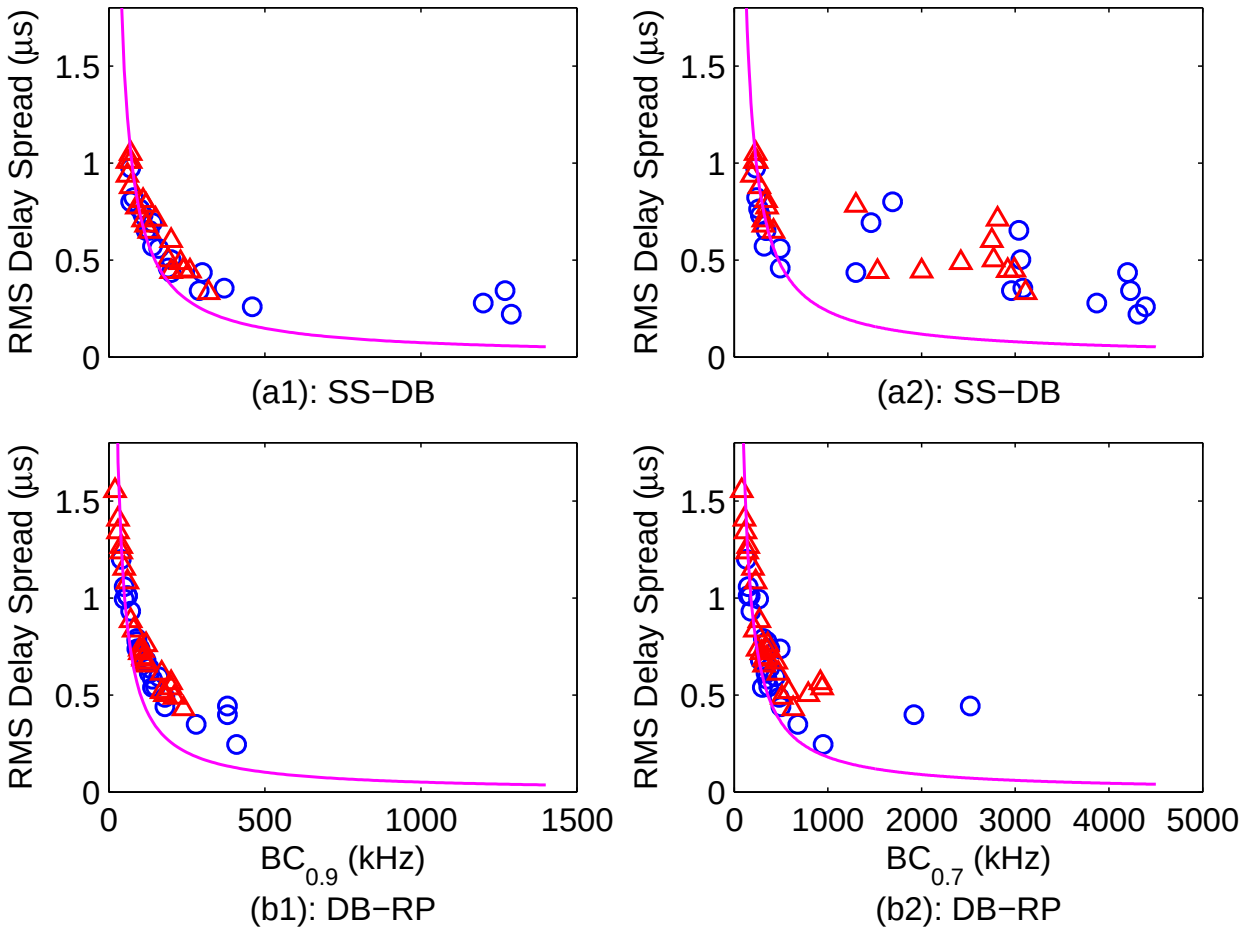

Figure 5.7: RMS Delay Spread as a function of $BC_{0.9|kHz}$ and $BC_{0.7|kHz}$ for the SS-DB links (a1)-(a2), and for the DB-RP links (b1)-(b2).

noise with PSD $P_w = -110$ dBm/Hz or with $P_w = -140$ dBm/Hz, i.e.,

$$C = \Delta f \sum_{m=0}^{M-1} \log_2 \left(1 + \frac{|H(f_m)|^2 P_{tx}}{P_w}\right) [bps]. \tag{5.11}$$

The sub-carriers are spaced by $\Delta f = 24.414$ kHz, with number $M = 1064$ in the HPAV frequency band while $M = 1961$ in the frequency band 2-50 MHz. $H(f_m)$ is the CTF evaluated at the $m-$subcarrier frequency. Measurements of the noise has shown that it ranges between the two considered values of PSD depending on the location and the devices operating on board of the ship.

In Fig. 5.8, we report the complementary cumulative distribution function (C-CDF) of the channel capacities for the SS-DB links in subplots (a1) and (a2), for the DB-RP links in subplots (b1) and (b2), in considered frequency bands.

It is possible to notice that the SS-DB links are those that statistically convey higher rate than the DB-RP links. In the HPAV band, for the SS-DB links, the 70-th percentile of the C-CDF curve is equal to 330 Mbps and 290 Mbps, respectively for the direct and the

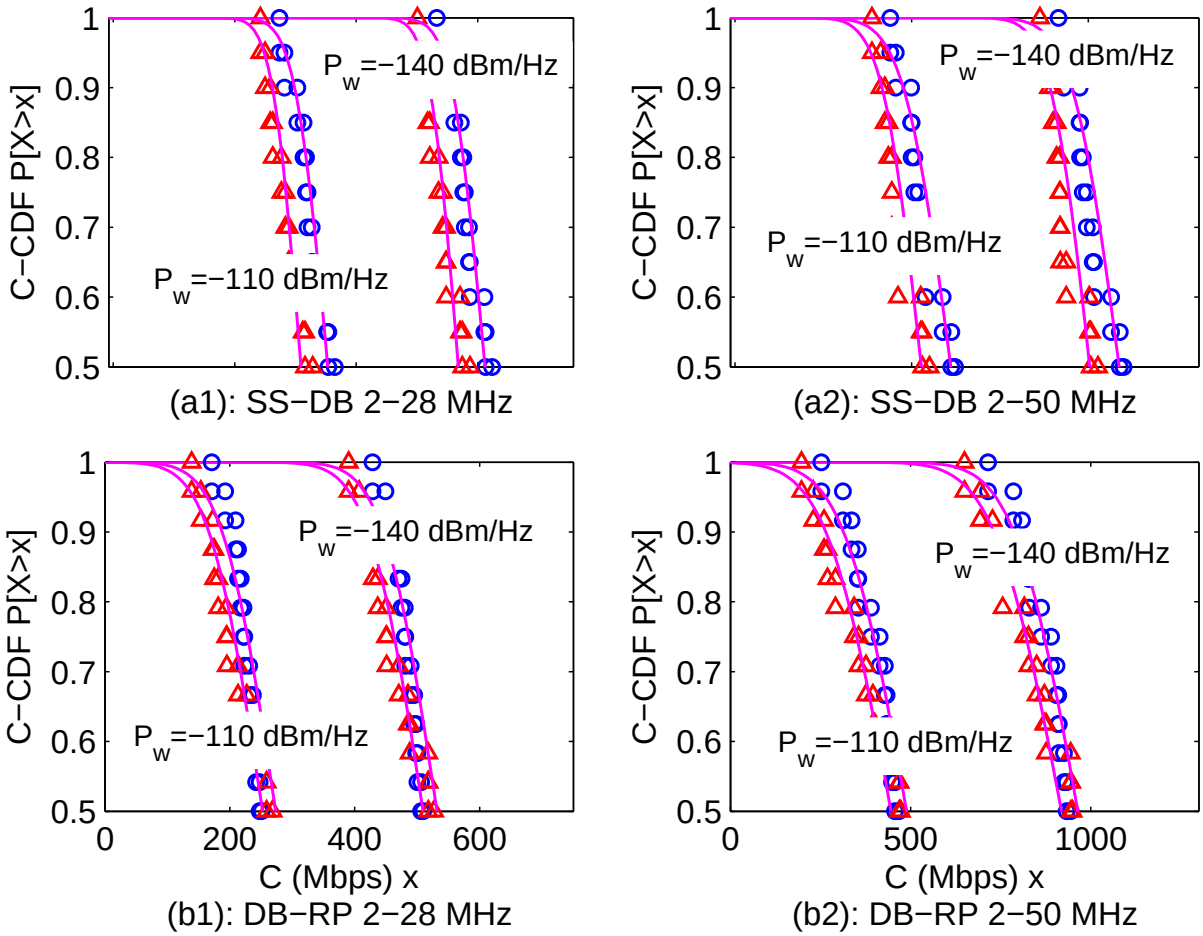

Figure 5.8: C-CDF of capacity for the SS-DB links (a1)-(a2), and for the DB-RP links (b1)-(b2), for two different noise PSD levels and frequency bands. Direct channels marked with blue circles, coupled channels marked with red triangles.

coupled channels with $P_w = -110$ dBm/Hz, and it is equal to 590 Mbps and 550 Mbps with $P_w = -140$ dBm/Hz. For the DB-RP links, the 70-th percentile of the C-CDF curve is equal to 240 Mbps and 220 Mbps, respectively for direct and coupled channels with $P_w = -110$ dBm/Hz, and it is equal to 490 Mbps and 470 Mbps with $P_w = -140$ dBm/Hz. Even if the DB-RP links convey lower rate, we have noted that the capacity of coupled channels is still 90-96% of the capacity of direct ones. The relatively small loss in capacity of the coupled channels, is due to the bus-bar system topology. This yields an advantage in practical scenarios where the modem placed in the rooms can be connected to different pair of phases. In the 2-50 MHz band, performances increase by up to 70% for the SS-DB links and by up to 85% for the DB-RP ones.

Since three phases are available, 2x2 MIMO transmission is possible. It should be noticed that a 2x2 MIMO transmission scheme implies that two signals are simultaneously transmitted in the two transmitting ports (between the RT conductors and ST conductors) and received in the two receiving ports. In our measurement campaign, the direct and coupled

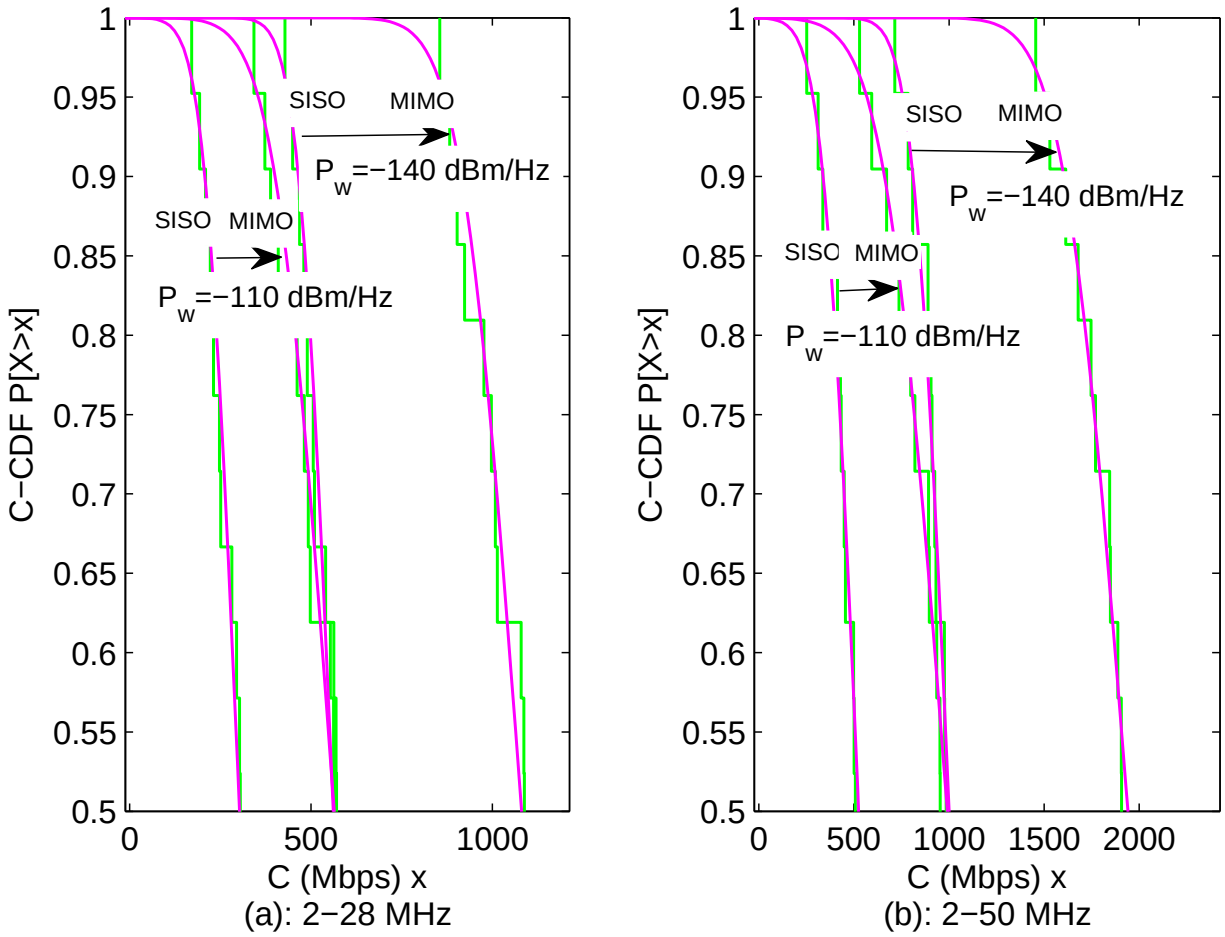

Figure 5.9: C-CDF of capacity for SISO and MIMO transmission for two different noise PSD levels and frequency band 2-28 MHz (a1) and 2-50 MHz (a2).

channels have been measured in a SISO transmission mode, i.e., leaving open the remaining input and output ports. Thus, the numerical results yield only an indication of the achievable capacity. To proceed, the overall CTF matrix of the MIMO transmission scheme $\mathbf{H}(f)$ is defined as

$$\mathbf{H}(f) = \begin{bmatrix} H_{(RT,RT)}(f) & H_{(RT,ST)}(f) \\ H_{(ST,RT)}(f) & H_{(ST,ST)}(f) \end{bmatrix}, \tag{5.12}$$

where $H_{(TX,RX)}$ is a SISO channel CTF with $TX, RX \in \{RT, ST\}$ denoting transmitting port and receiving one. Under the same assumptions in (5.11), the MIMO capacity reads

$$C_{MIMO} = \Delta f \sum_{m=0}^{M-1} \log_2 \left[\det \left(\mathbf{U} + \mathbf{H}_m \mathbf{H}_m^H \frac{P_{tx}}{2P_w} \right) \right], \tag{5.13}$$

where $\mathbf{U}$ is the 2x2 identity matrix, $\mathbf{H}_m$=$\mathbf{H}(f_m)$ and ^{H} denotes the hermitian transpose.

In Fig. 5.9, we report the C-CDF of the MIMO channel capacities achievable over all links (SS-DB and DB-RP) assuming a constant transmit PSD equal to $P_{tx} = -50$ dBm/Hz, and

two different values for the noise PSD, i.e., $P_w = -110$ dBm/Hz and $P_w = -140$ dBm/Hz in the frequency band 2-28 MHz (a1) and 2-50 MHz (a2). On average, the MIMO channel yield a capacity that is double that of the SISO channel, in both considered frequency bands.

5.5 Effect of Circuit Breakers

Herein, we study the effect of the circuit breakers of the distribution boards. In Fig. 5.10-(a), we compare the $ACG_{|dB}$ for the SS-DB links when the receiver is placed at the input of the the primary circuit breaker (RT ST), at the output of it (RT ST (1)), and at the output of the secondary circuit breaker of the distribution board (RT ST (2)) (see Fig. 5.2). The transmitter is fixed at the substation switchboard after the secondary circuit breaker. On average, the attenuation due to primary and secondary circuit breakers is approximately 7 dB. In a dual manner, we compare the $ACG_{|dB}$ for the DB-RP links. Now, we fix the receiver at the room panel and we move the transmitter respectively at the input of the the primary circuit breaker, at the output of it, and at the output of the secondary circuit breaker of the distribution board. Clearly, the $ACG_{|dB}$ of the links between the distribution board and the room panel that do not involve any circuit breaker is 7 dB higher than the links that include circuit breakers (Fig. 5.10-(b)).

5.6 Main Findings

We have reported the results of a measurement campaign on board of a cruise ship over the low voltage power grid. The analysis shows that the channel statistics are similar to those reported in other application scenarios, e.g., the in-home scenario. In particular, the ACG and the RMS-DS are lognormally distributed. However, the mean values are somewhat higher than those found in the in-home case. Nevertheless, the LV in-ship channels can carry high amount of data information as the analysis of the capacity shows. This is in excess of 200 Mbps and up to about 600 Mbps for the band 2-28 MHz depending on the noise conditions and on the power grid section. It increases by up to 85% in the band 2-50 MHz. In particular, the links between the MV/LV substation and the distribution boards have higher capacity than the links between the distribution boards and the room service panels. This can be justified by the fact the latter scenario is characterized by a topology with more branches which causes higher frequency selectivity and fading. Theoretical capacity can be approximately doubled if a MIMO transmission scheme is used, which is applicable to three-phase electrical power distribution system.

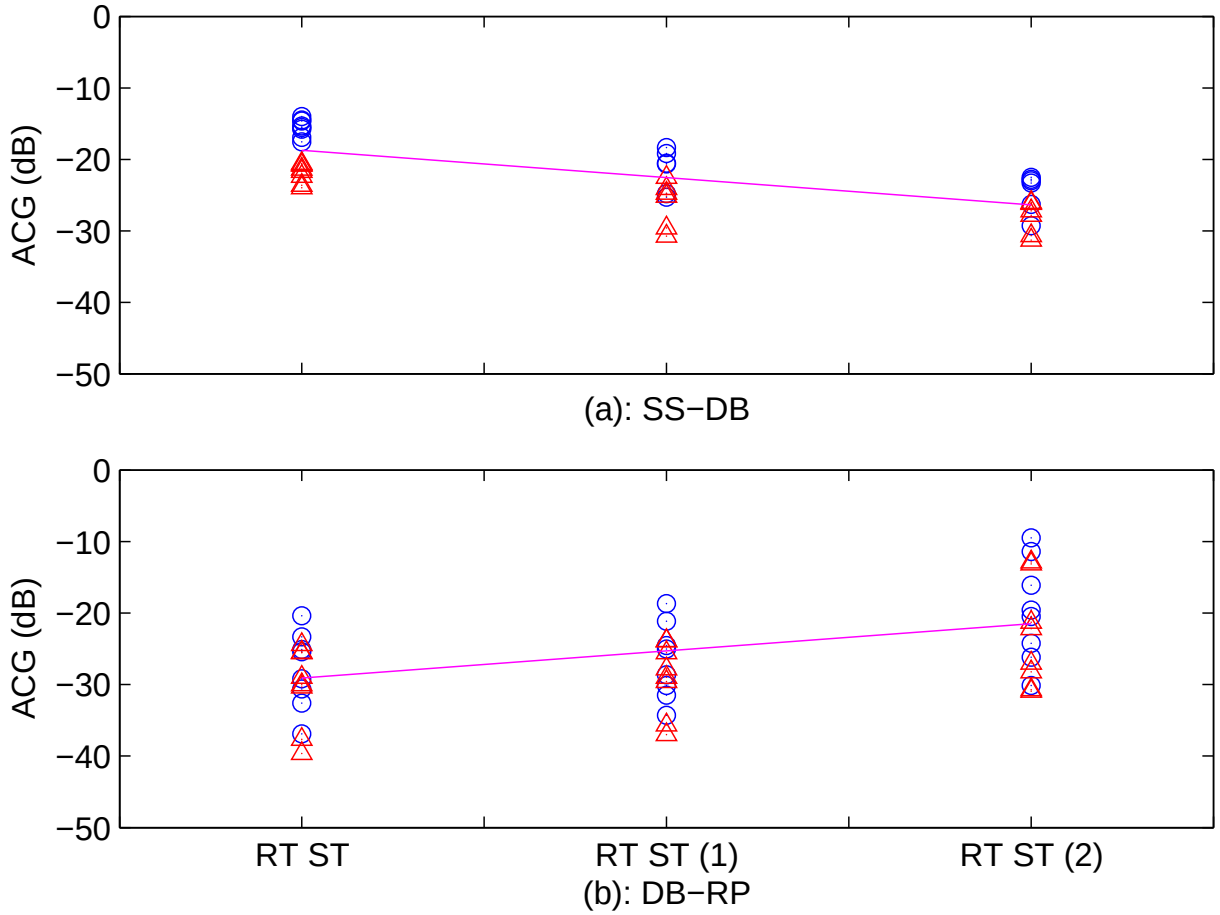

Figure 5.10: Effect of the circuit breakers of the distribution boards. (a): The receiver is placed at the input of the the primary circuit breaker (RT ST), at the output of it (RT ST (1)), and at the output of the secondary circuit breaker of the distribution board (RT ST (2)). The transmitter is fixed at the substation switchboard after the secondary circuit breaker. (b): The receiver is fixed at the room panel, while the transmitter is placed in the distribution board.

Chapter 6

In-car PLC

From a PLC point of view, the world of the electrical vehicles has not been deeply investigated yet. In this chapter, we report the results of an entire PLC noise and channel measurement campaign that we have carried out in a compact electrical car.

Our research activity has been supported by the Italian project (FVG Region) ESTAMOS (Electronics and Systems in the Electrical Car for Sustainable Mobility) `http://www.progettoestamos.it`.

6.1 Introduction

New generation vehicles deploy a wide set of sensors and electronic equipments. As mentioned, PLC is an attractive solution to interconnect them. Since PLC exploits the existing power infrastructure to deliver data services, it is suitable for being an innovative electronic and telecommunication technology for the future smart cars. Focusing on the electrical vehicles, PLC is an interesting solution also due to the intrinsic nature of the electric power system, w.r.t. the wiring infrastructure of standard vehicles. In fact, electrical vehicles are equipped with a dedicated power grid to supply the electric engine. Battery management to control charge, discharge and energy flow to the electric engine and electronic equipments can be made by integrated boards and ECUs connected via power cables. Again, the benefits of using PLC are the reduction of weight, cost and complexity of the vehicle wiring harness.

Early works deal with the analysis of the potential of in-vehicle PLC in conventional cars [55–66]. Conversely, the world of the electrical vehicles has not been deeply investigated yet. The PLC channel characterization in a fully electric commercial vehicle is the topic of the research activity in [67]. In [68], the authors focus on a hybrid electrical vehicle and present the results of a PLC channel measurement campaign.

In this chapter, we report the results of the experimental PLC measurement campaign that we have carried out in a 4-wheel compact electrical car. We study the impact of the existing electric and electronic systems on the PLC transmission medium, and we dig into the noise generated by such devices. We address both the NB and the BB frequency range.

Figure 6.1: Picture of the compact electric car under test.

Therefore, we investigate the potential data transmission performance in terms of theoretical achievable rate in the two mentioned ranges.

The chapter is organized as follows. Section 6.2 provides and overview of the vehicle under test. Section 6.3 explains the measurement scenario and setup. In Section 6.4, we provide the full set of results, i.e., noise, channel, and impedance results. In the NB, we also provide an analytical expression for the harmonic content of the PLC noise that we have measured. Section 6.5 addresses the results of the theoretical analysis of the potential data transmission performance. Finally, Section 6.6 summarizes the main findings.

6.2 Overview of the Vehicle Under Test

We have performed the PLC measurement campaign over the electric power system of the Birò [69], which is a 4-wheel compact electrical car made in Italy (see Fig. 6.1). The vehicle under test is equipped with two 3-phases brushless 48V electric engines. Each electric engine moves one of the two rear wheels. Power is ensured by a battery pack that comprises four 12V-100Ah lead gel batteries. The battery pack directly supplies the two ECUs that drive the electric engines. Basically, each ECU controls the flow of the current through the three

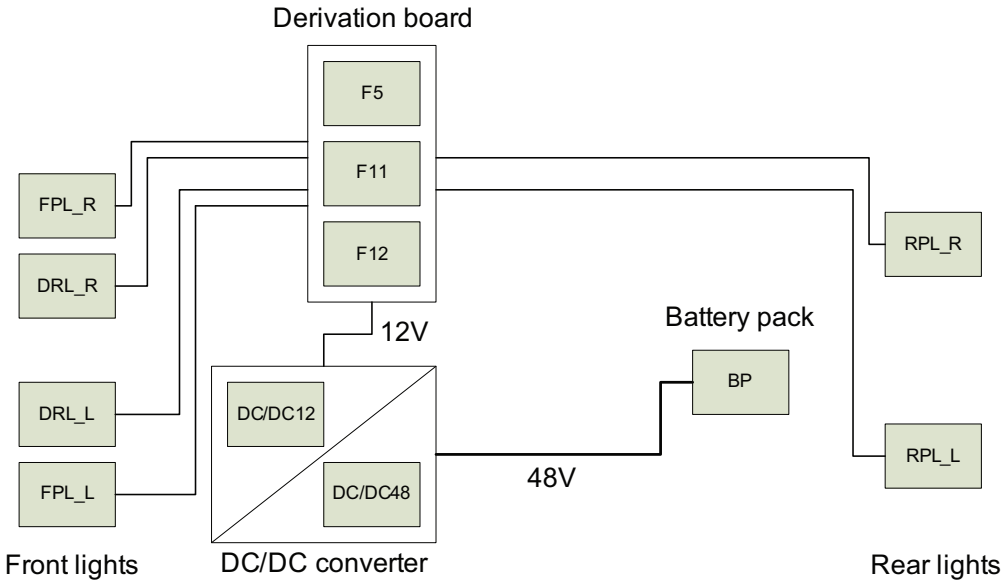

Figure 6.2: Schematic of the measurement scenario.

coils of the engine, i.e, the three phases. The rotation of the rotor of the electric engine is ensured by the commutation of the power through the three phases according to a certain control sequence.

A DC/DC converter is used to convert 48V DC to 12V DC, in order to supply the 12V power network of the vehicle. The 12V electrical system feeds the 12V standard peripherals, i.e., lights, break lights, indicators. The 12V output of the DC/DC converter feeds a derivation board. All the 12V peripherals are connected to the derivation board through two feeding conductors.

The peculiarity of the electric system under test is that each peripheral is fed by a dedicated positive wire, while groups of nearby devices share the same negative wire. The negative wire is distributed to all nodes from the negative pole of the battery and it is not connected to the chassis. As a consequence, positive and negative wires do not necessary are deployed in parallel to each other.

6.3 Measurement Scenario and Setup

We have selected a set of strategic access points for PLC purposes. In the 12V power network, we have placed test points in proximity of the front position and daytime running lights, the rear position lights, in the derivation board (fuse box) and the DC/DC converter (12V side). In the 48V electric power system, we have focused on the battery pack and the DC/DC converter (48V side). The test points can resemble hypothetical PLC nodes, i.e., sensors or new generation lighting drivers controlled via power cables. Fig. 6.2 depicts the schematic of the measurement scenario. In detail, the DC/DC converter is physically located in the front part of the vehicle, near the derivation board. This fact has a strong impact on PLC channel

Table 6.1: List of the test points.

Test Point	Acronym
Front position light, left	FPL_L
Daytime running light, left	DRL_L
Front position light, right	FPL_R
Daytime running light, right	DRL_R
Rear position light, left	RPL_L
Rear position light, right	RPL_R
Battery pack (48V terminals)	BP
DC/DC converter (48V side)	DC/DC48
DC/DC converter (12V side)	DC/DC12
Fuse brake lights	F5
Fuse FPL_L-RPL_R	F11
Fuse FPL_R-RPL_L	F12

measurements, as it will be explained in the following. We have placed test connectors in parallel to the feeding conductors of the peripherals, without disconnecting them from the power supply grid. In the fuse box, we have replaced the correspondent fuse with a built-in connector that act as a shunt connector but, at the same time, it allows access to the test node. We have designed the connectors such that their physical length did not affect the PLC channel properties in the frequency range of interest.

To ease the notation, in the following, we use the acronyms of Table 6.1 to indicate the test points.

We have performed measurements both in the NB and BB frequency range. We have deployed NB and BB capacitive couplers to protect the measurement equipment from the power supply voltage. The frequency response of the NB couplers is flat in the frequency range 3-500 kHz. The BB couplers allow reliable measures up to 100 MHz.

Noise measurements have been made in the time domain using a DSO with 50 Ω input impedance adapter (cf. Section 1.4.1). The sampling rate, the time window and the memory depth of the DSO has been fixed according to the desired time span, frequency range and resolution. In detail, for NB noise measures, we have collected 100k samples with a sampling rate equal to 50 MSamples/s (Δf=500 Hz). For the BB noise measures, we have collected 1M points per trace, with a sampling rate of 250 MSamples/s (Δf=250 Hz).

The channel and impedance measurements have been performed in the frequency domain using a VNA (see Section 1.2.1). We limited the number of access points for the channel and impedance measurements. In fact, we have experienced high level of background noise on the test points in proximity of the DC/DC converter (both 48V and 12V side) and in the derivation board. To prevent the damage of the VNA, we discarded the aforementioned test points. The VNA has been set to acquire the maximum number of measurement points

(1601) in the frequency range 3-500 kHz and 2-100 MHz, respectively the NB and the BB frequency range of interest.

Basically, we have performed the noise and channel measurements for three different states of the vehicle, i.e.,

- electric engines OFF: the front and rear position lights and the daytime running lights are switched ON but the electric engines are in idle state;
- electric engines ON: the electric engines are running but not under heavy load condition;
- heavy load condition: the electric engines are running under heavy load condition.

6.4 Measurement Results

In the following, we first analyze the PLC noise, within the NB and BB frequency range. In the NB, we provide an analytic expression for the harmonic noise components. Thus, we present the channel and impedance measurement results.

6.4.1 PLC Noise

Firstly, we present the results of the noise measurements in the NB frequency range, with a description of the noise components. Afterwards, we will present the results for the BB spectrum.

In this particular PLC environment, the main noise source is the DC/DC converter. As we have described in the previous sections, this block allows to feed the 12V peripherals with the 48V available voltage. The switching DC/DC converter comprises two reactive components, typically an inductor and a capacitor connected as a LC lowpass filter, a MOSFET used as a switch and a diode. The MOSFET is driven with a square wave with a specified duty cycle that gives the conversion ratio. When the square wave is high, the input voltage charges the inductor and the diode is turned OFF. Viceversa, with a low level of the square wave, the diode is turned ON with the discharge current of the inductor. The result at the output is a constant voltage with a triangular ripple caused by the charge-discharge cycle on the inductor. For this reason, the measured noise is composed by a triangular waveform with an additional resonance effect that introduces a high frequency contribution for the noise. The resonance is caused by the reactive components inside the DC/DC converter. Since the MOSFET active transistor is driven by a square wave as mentioned above, this causes a discontinuous current flow to the LC low-pass filter. At the falling or rising edges of the square wave, a overshooting response is added to the triangular ripple voltage. This particular waveform is the common ripple signal present at the output of a switching converter. In the following we will refer to it as triangular noise.

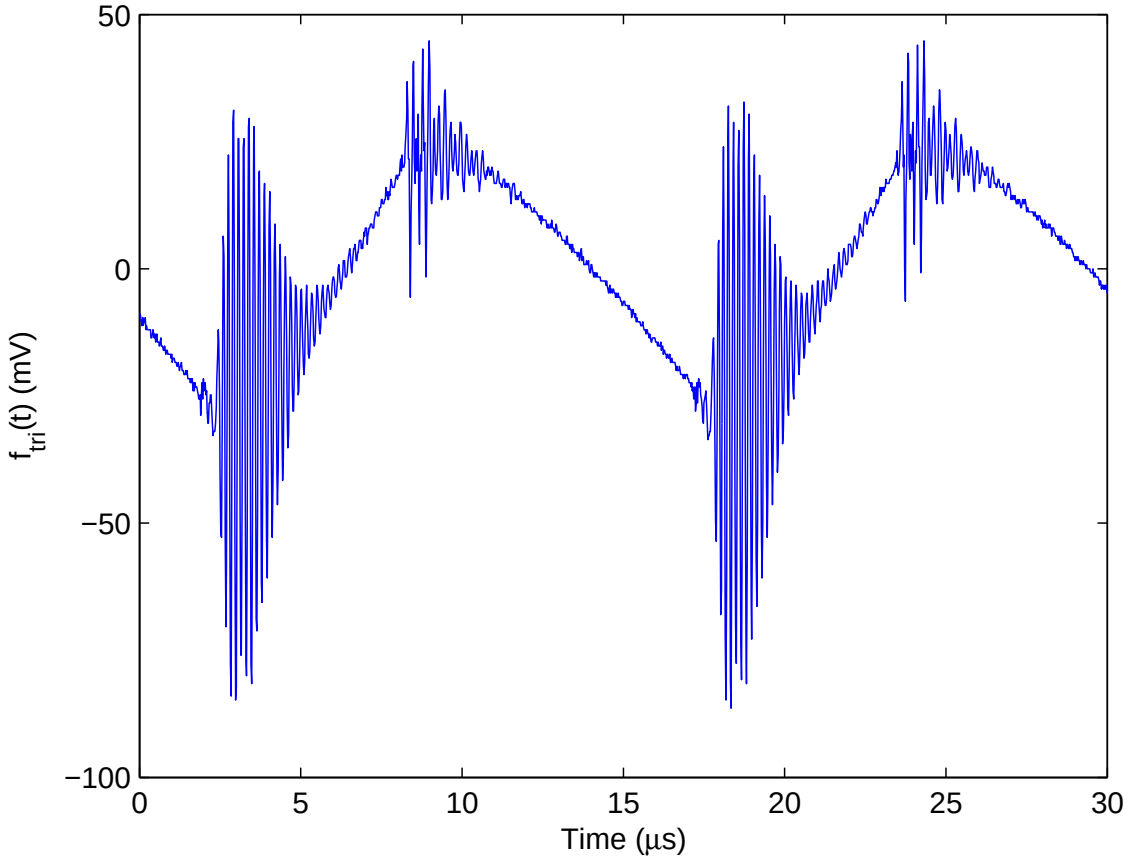

Figure 6.3: Noise voltage waveform experienced at the DRL_L access point. The electric engines were running under heavy load condition.

To measure the noise we have used a DSO. Fig. 6.3 shows the triangular waveform measured at the DRL_L access point. Here, the overshooting is limited to a small voltage value, and the dynamic voltage range of the DSO is entirely used to acquire the noise signal with the best accuracy. We can notice the superposition of other noise component, that is present when the engine is in hig load condition. It is possible to derive an analytical expression for the triangular noise, that affects the NB spectrum as follows.

$$\begin{cases} f_{tri}^{(1)}(t) = A_{tri}\left(\frac{1}{D_{DC}T_{DC}}t - 1\right); \quad t \in [0, D_{DC}T_{DC}[\\ \\ f_{tri}^{(2)}(t) = \frac{A_{tri}}{1-D_{DC}}(1 + D_{DC}) - \frac{A_{tri}}{1-D_{DC}}\frac{1}{T_{DC}}t; \quad t \in [D_{DC}T_{DC}, T_{DC}] \end{cases} \tag{6.1}$$

where T_{DC}, A_{tri}, and D_{DC} are respectively the period, the amplitude and the duty cycle of the triangular waveform. Particularly, the duty cycle depends on the duty cycle of the square waveform that drives the MOSFET transistor. With the Fourier expansion series, it

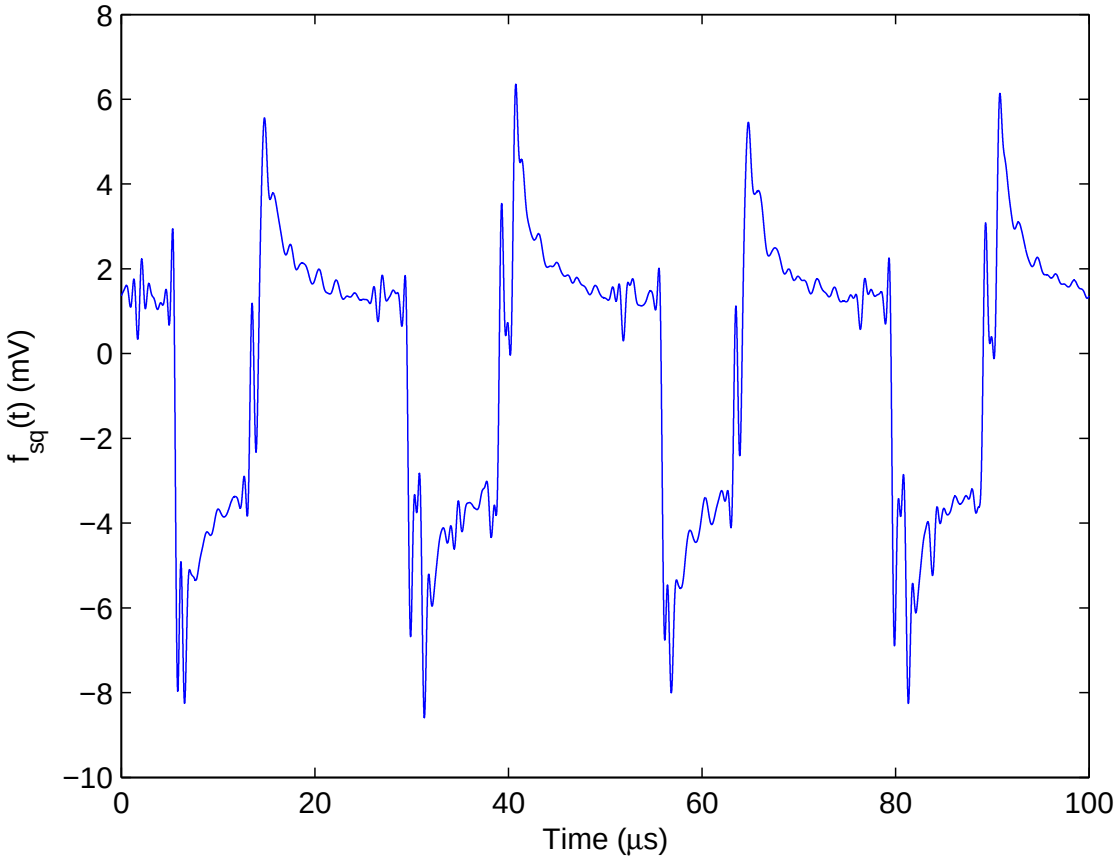

Figure 6.4: Squared power engine waveform measured on a solenoid wrapped on a phase of one of the two engines.

is possible to describe analytically the occupied spectrum:

$$f_{tri}(t) \sim \sum_{k=1}^{+\infty} a_k^{(tri)} \cos\left(\frac{2\pi t}{T_{DC}}k\right) + b_k^{(tri)} \sin\left(\frac{2\pi t}{T_{DC}}k\right) \tag{6.2}$$

with

$$\begin{cases} a_k^{(tri)} = \frac{A_{tri}}{(k\pi)^2}\left[\frac{1}{D_{DC}}[\cos(2\pi k D_{DC}) - 1] - \frac{1}{1-D_{DC}}[1 - \cos(2\pi k D_{DC})]\right] \\ b_k^{(tri)} = \frac{A_{tri}\sin(2\pi k D_{DC})}{\pi^2 k^2 D_{DC}(1-D_{DC})}. \end{cases} \tag{6.3}$$

The triangular noise has a period of $T_{DC} \approx 15.4\ \mu s$, with a duty cycle $D_{DC} \approx 0.37$. This suggests that a flyback DC/DC converter has been used. Another noise source is given by the power signal that feeds the engines. The loaded engine requests a great amount of current to move the wheels, and the current that drives the engines is composed of a square waveform with a different duty cycle D_{EN} for each of the three phases. Fig. 6.4 depicts the square waveform measured on a solenoid wrapped on a phase wire of one of the two engines. This current generates a magnetic field that is concatenated with the rest of the electrical power system. This induces a noise voltage on the other wires, that depends to the load at

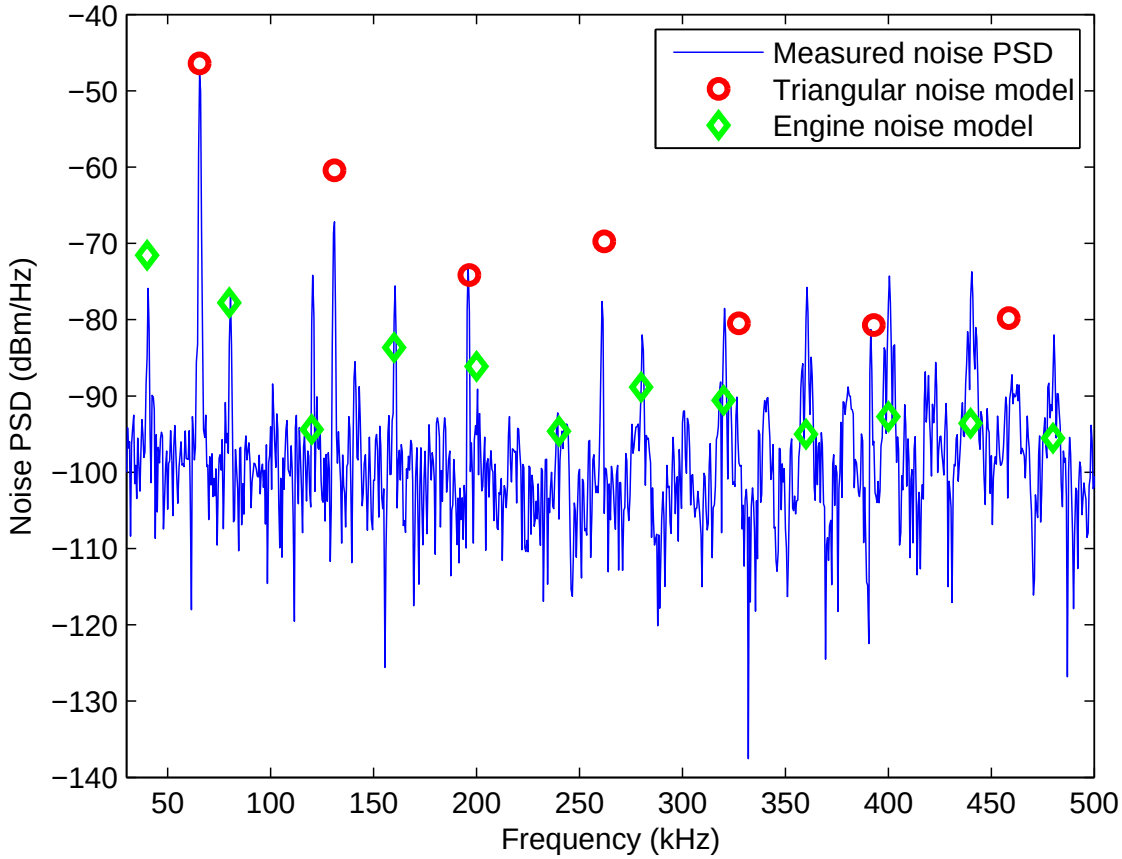

Figure 6.5: PSD of the NB noise experienced at the DRL_L access point. The electric engines were running under heavy load condition.

the engines with an amplitude A_{sq}. This value depends to the amount of current requested by the engines. The Fourier expansion series for the engines' concatenated voltage is

$$f_{sq}(t) \sim \sum_{k=1}^{+\infty} a_k^{(sq)} \cos\left(\frac{2\pi t}{T_{EN}} k\right) + b_k^{(sq)} \sin\left(\frac{2\pi t}{T_{EN}} k\right) \tag{6.4}$$

with

$$\begin{cases} a_k^{(sq)} = \frac{A_{sq}}{k\pi} \sin(2\pi k D_{EN}) \\ \\ b_k^{(sq)} = \frac{A_{sq}}{k\pi} [1 - \cos(2\pi k D_{EN})]. \end{cases} \tag{6.5}$$

For the engines' current, we have calculated $T_{EN} \approx 25\ \mu s$ and $D_{EN} \approx 0.67$.

In the NB, all the harmonic components has been analytically calculated. The measured spectrum in the NB channel is shown in Fig. 6.5. We report the case of electric engines under heavy load condition. As it should be noticed, the highest harmonics are multiple of $1/T_{DC}$, i.e. 65 kHz. The loaded engines instead cause a lot of harmonic contributions at the multiple frequencies of $1/T_{EN}$, i.e., 40 kHz.

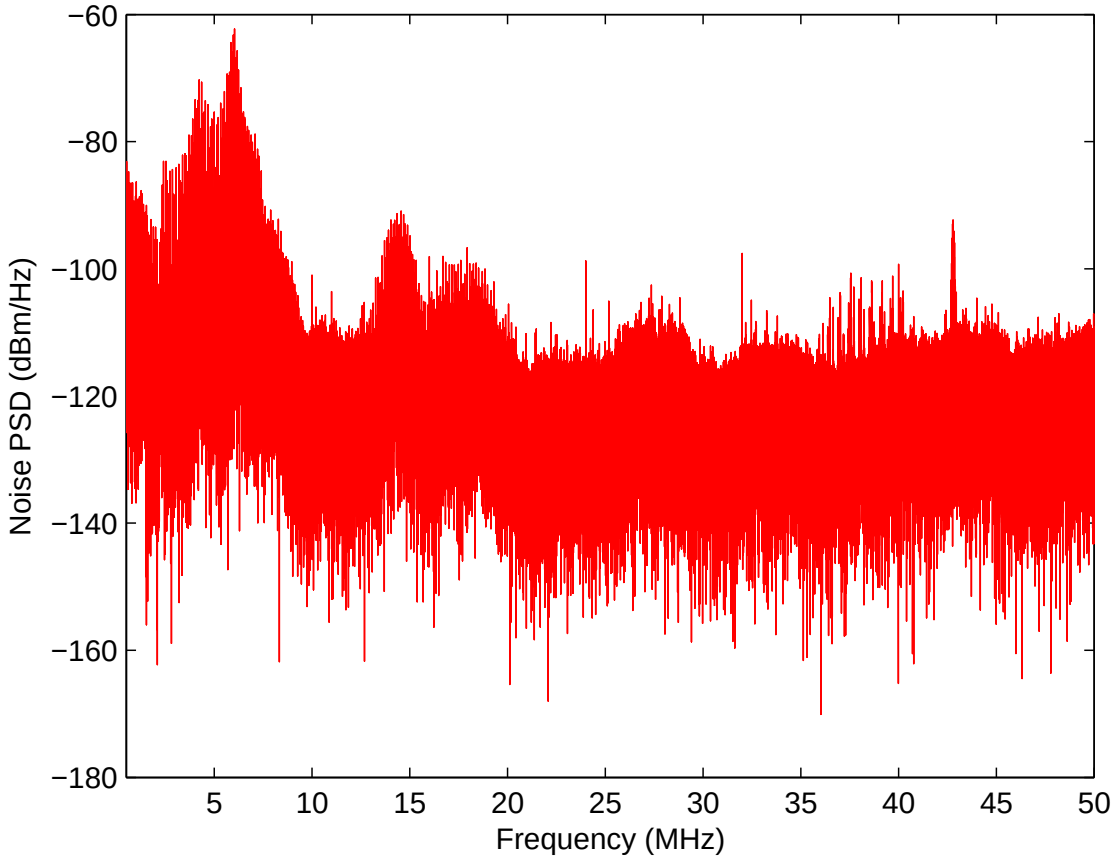

Figure 6.6: PSD of the BB noise experienced at the DRL_L access point. The electric engines were running.

Now, the BB measurements allows us to explore the PSD of the noise at frequencies above 500 kHz. The main contribution is given by the overshooting oscillations. Measuring the oscillation period, we have found a spectral occupancy in the range of 4.5-6.5 MHz. In Fig. 6.6, we show the measured PSD up to 25 MHz. For higher frequencies, the measured PSD approaches the noise floor of the DSO.

6.4.2 PLC Channel and Impedance

Herein, we provide results in terms of of PL (see Section 2.4.1). Again, $PL(f) = |H(f)|^2$, where $H(f)$ is the CTF between two test points. Firstly, we classify the channels into three different classes, according to their NB PL profile. In Fig. 6.7, we show the PL of three representative channels, i.e., one for each of the three classes. In the NB, we have not experienced substantial differences between the channel frequency response for the three different states of the vehicle. Furthermore, there is no relation between the physical length of the electrical paths and the attenuation profiles. We note that the most attenuated channels are the power links between the BP and the other access points. This is amenable to the

Table 6.2: Parameters for NB Data Transmission Performance Analysis.

Parameter	Cenelec A	Cenelec B	Cenelec C
Start frequency (kHz)	35.938	98.4375	128.125
Stop frequency (kHz)	90.625	121.875	137.500
Δf (kHz)	1.5625	1.5625	1.5625
M	36	16	7
P_{tx} (dBm/Hz)	-30	-30	-30

presence of the DC/DC converter that blocks the NB PLC signal. In Fig. 6.8, we analyze the access impedance for three different access points, i.e., in proximity of the FPL_L, the DRL_L and the BP. From measures, we have found that both the light bulbs and the battery pack impose a low impedance value to the access impedance. The very low values of the aforementioned loads are also the cause of the high attenuation of the PLC channel.

Thus, we also investigate the channel frequency response in the 2-100 MHz band. The purpose is to evaluate the possibility to convey BB PLC signal through the power cables of the vehicle under test. Fig. 6.9 and Fig. 6.10 show respectively the PL and the access impedance profiles of the same links of Figs. 6.7-6.8.

6.5 Data Transmission Performance

From measures, we study the potential data transmission performance in terms of theoretical achievable rate, in the NB and BB frequency range. In the NB, we focus on the Cenelec bands A, B, and C. In the BB, we focus on the HPAV frequency band 2-28 MHz [7] and in the extended band 2-100 MHz. As we have seen in the previous chapters, from theory, the theoretical link achievable rate C reads as follows

$$C = \Delta f \sum_{m=1}^{M} \log_2 \left(1 + \frac{P_{tx}(f_m)|H(f_m)|^2}{P_w(f_m)} \right) [bps], \tag{6.6}$$

where $P_{tx}(f_m)$ and $P_w(f_m)$ are respectively the PSD of the transmitted signal and the PSD of the measured noise at frequency f_m, M is the number of sub-carriers and Δf is the sub-carrier frequency spacing. For all the parameters in (6.6), we refer to Tables 6.2 and 6.3, respectively for the NB and BB analysis. In both cases, we assume the PSD of the transmitted signal to be constant.

In Fig. 6.11, we show the C-CDF of the theoretical link achievable rate for the Cenelec bands A, B, and C, for the three different states of the vehicle. As shown in subplot (a), the 70-th percentile of the C-CDF correspondent to the Cenelec band A is in excess of 240 kbps and up to 300 kbps, respectively for the turned OFF engines case and heavy loaded engines case. Similarly, in the Cenelec band B, the depicted C-CDF shows that the theoretical rate

Table 6.3: Parameters for BB Data Transmission Performance Analysis.

Parameter	HPAV	HPAV Ext.
Start frequency (MHz)	2	2
Stop frequency (MHz)	28	100
Δf (kHz)	24.414	24.414
M	1065	4015
P_{tx} (dBm/Hz)	-50	-50

is in excess of 140 kbps and up to 200 kbps, respectively for the turned OFF engines case and heavy loaded engines case. In the Cenelec band C, the theoretical achievable rate is in excess of 60 kbps and up to 80 kbps. It should be noticed that the maximum achievable data rate decreases when we moves from Cenelec A to Cenelec C. This is caused by the decrease of the bandwidth assigned to the three mentioned standard bands.

Therefore, we have experimentally investigated the performance of G3-PLC [2] compliant devices operating in Cenelec bands A, B, C. On average, the experimental data rates are 90-98% lower than the potential attainable ones. Thus, further optimization is necessary to deploy G3-PLC robust solutions for the in-vehicle scenario.

Now, we focus on the HPAV frequency band 2-28 MHz and in the extended band 2-100 MHz. In Fig. 6.12, we show the C-CDF of the achievable rate for the two BB frequency ranges of interest, for two different states of the vehicle. We note that PLC channels can convey high rate. At 70%, the theoretical achievable rate is in excess of 140 Mbps and up to 170 Mpbs in the HPAV band, depending on the vehicle state. The performances increases by up to 400% in the extended band. The analysis shows that there is margin to develop practical schemes that provide high reliability data rates of interest for in-vehicle applications. In this respect, an analysis of the performance that can be achieved by applying multicarrier (MC) and impulsive ultra wideband (I-UWB) modulation to in-car power line channels has been performed in [70].

6.6 Main Findings

In this chapter, we have presented the results of an entire PLC noise and channel measurement campaign that we have performed in a compact electrical car. We have set our focus on the noise caused by the electric and electronic components of the vehicle. We have demonstrated that the main noise sources are the DC/DC converter and the concatenated voltage generated by the high amount of current that flows to the electric engines. We have derived an analytical model for the harmonic content of the NB PLC noise, and we have given an overview to the BB harmonic components. Furthermore, from measures, we have studied the potential data transmission performance in terms of theoretical achievable rate.

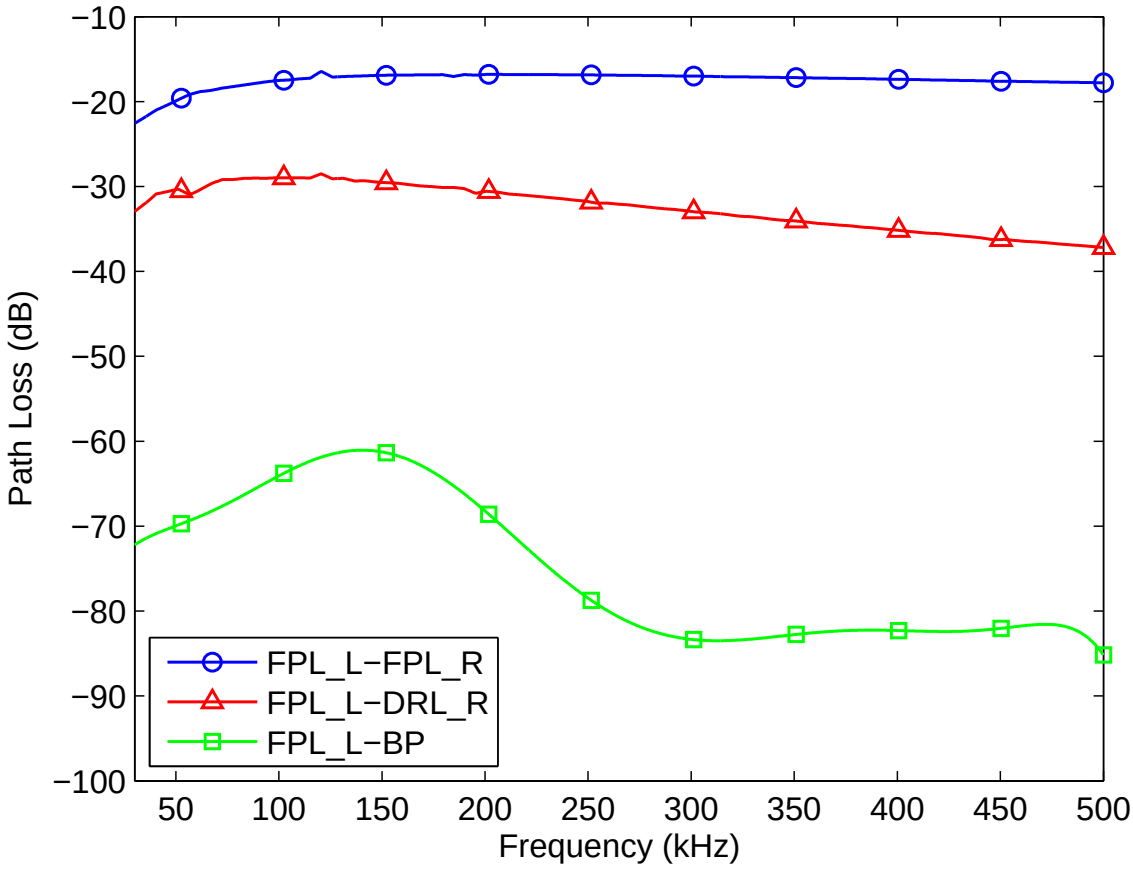

Figure 6.7: NB PL of the three representative channels, i.e., one for each of the three classes.

We have addressed both the NB spectrum, i.e., the Cenelec bands A, B, and C, and the BB. In the NB, the achievable data rate is in excess of 60 kbps and up to 300 kbps depending on the considered band and the vehicle state. In particular, performance decreases by up to 25% when the electric engines run under heavy load conditions. Conversely, the BB PLC channel can potentially convey high data rate. Thus, practical schemes that provide high speed and reliable communications can be deployed.

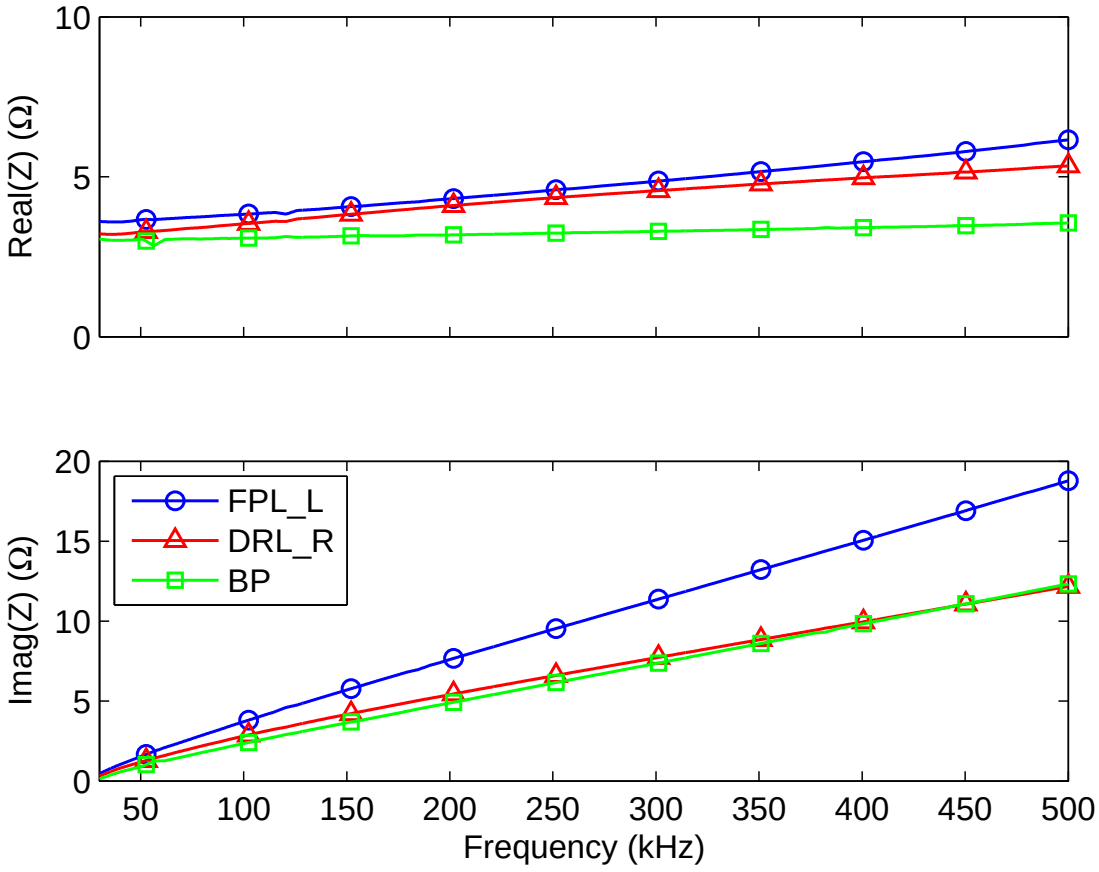

Figure 6.8: NB access impedance of the three representative test points.

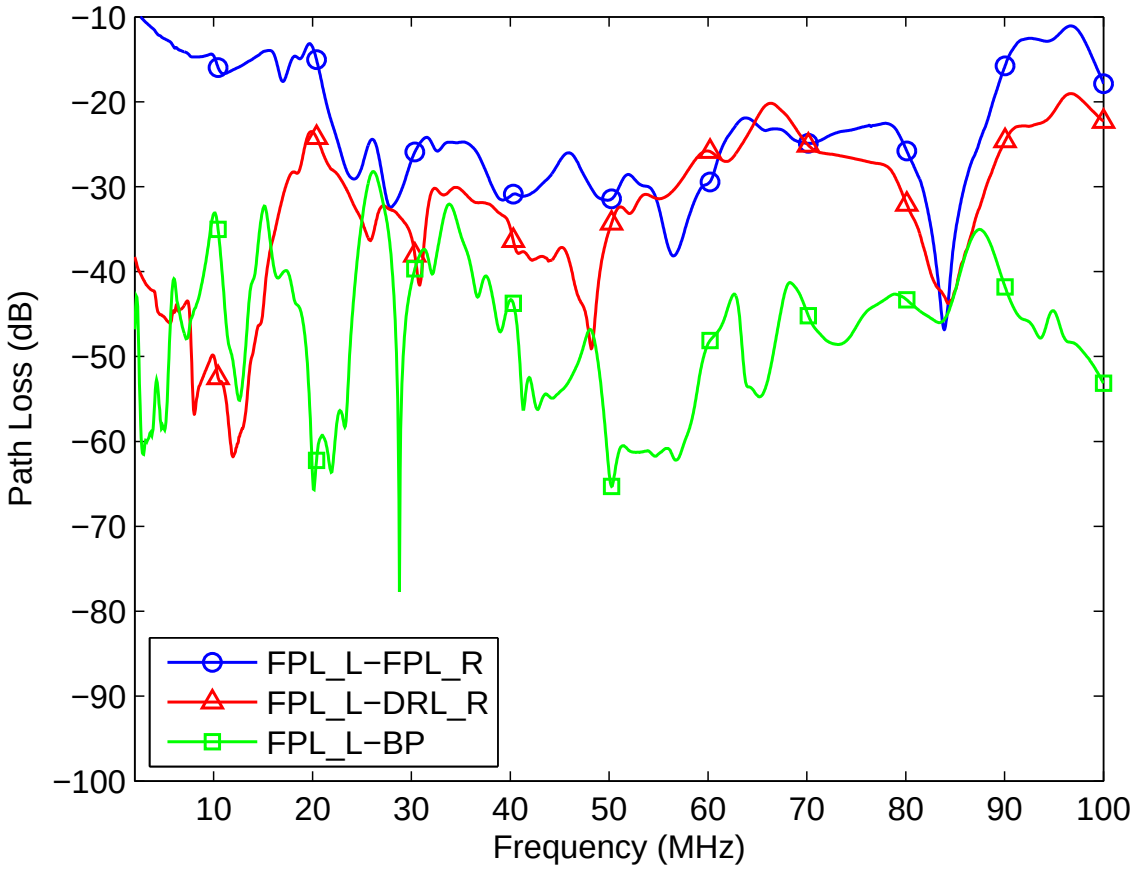

Figure 6.9: BB PL of the three representative channels, i.e., the same channels of Fig. 6.7.

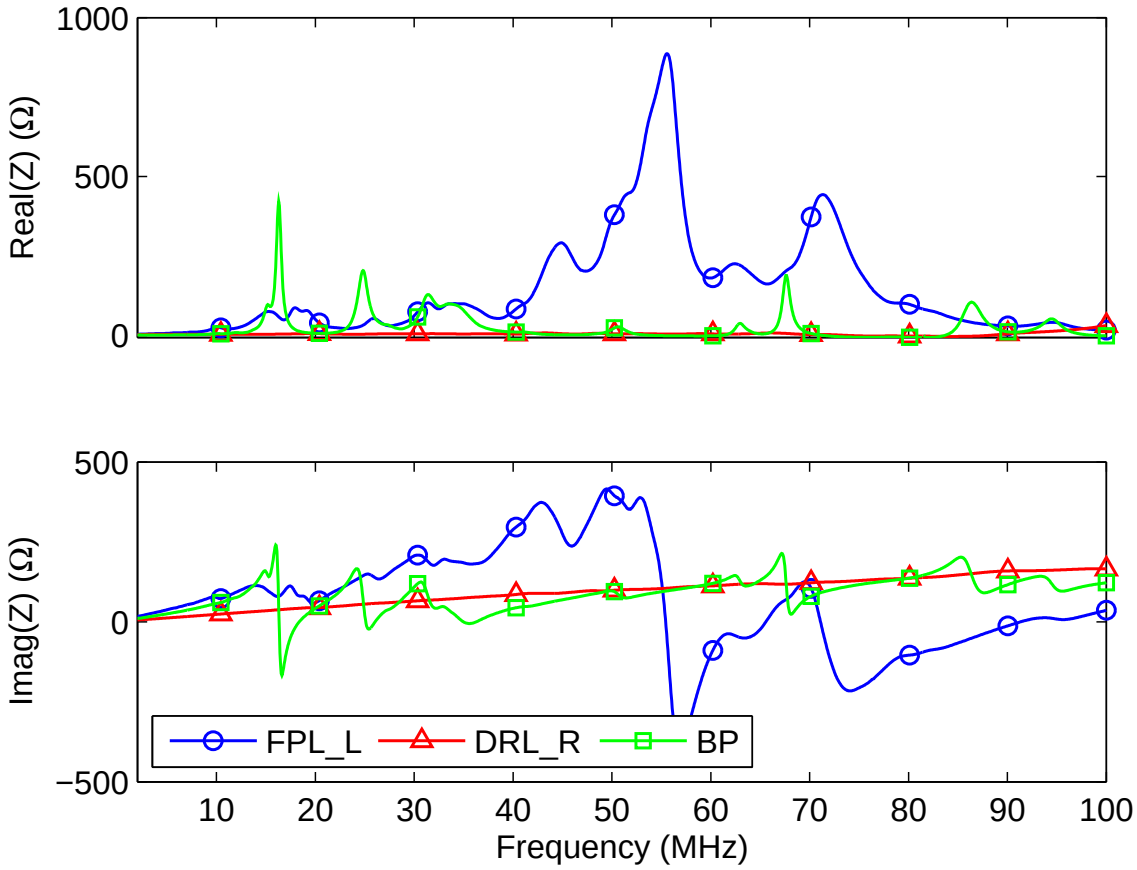

Figure 6.10: BB access impedance of the three representative test points, i.e., the same access points of Fig. 6.8.

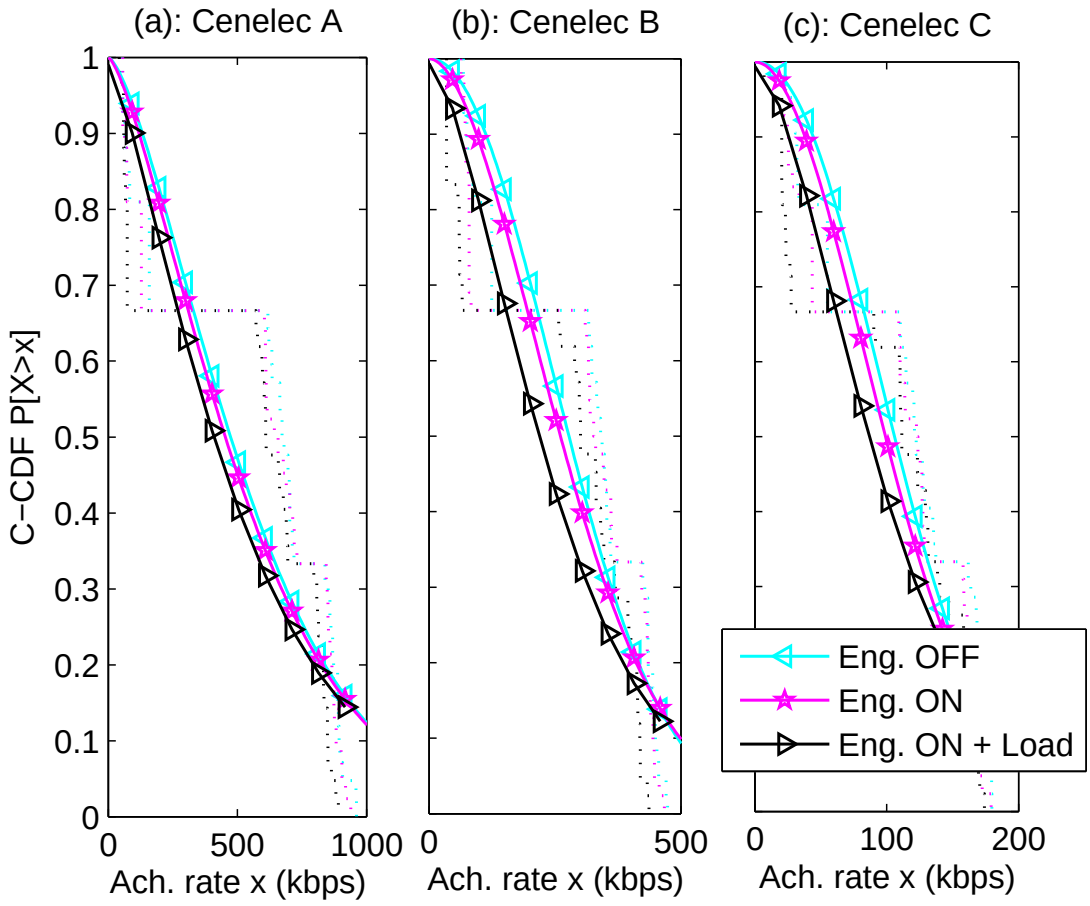

Figure 6.11: C-CDF of the theoretical link achievable rate in the Cenelec bands A (a), B (b), and C (c).

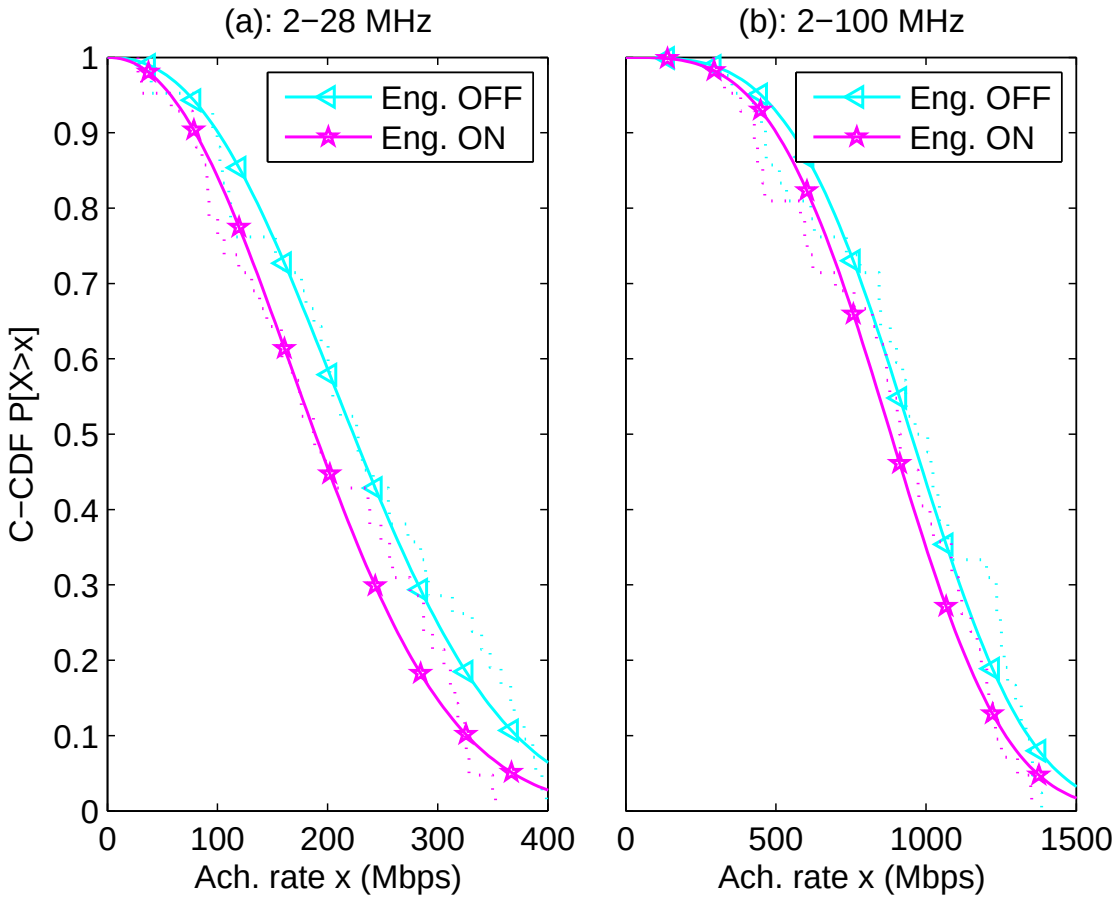

Figure 6.12: C-CDF of the theoretical link achievable rate in the HPAV (a) and in the extended band 2-100 MHz (b) frequency band.

Chapter 7

Conclusions

For the proper design of a PLC system, good knowledge of the grid characteristics in terms of propagation channel and disturbances is required. In this respect, we have performed experimental measurement campaigns in several scenarios where PLC can be applied. We aimed to investigate the grid characteristics from a telecommunication point of view. In this thesis, we have presented the results and the contributions of our experimental activity.

Outdoor and Industrial PLC

We have reported the results of the experimental measurement campaign that we have carried out in a fully-customizable three-phase microgrid with multiple loads and generators that can resemble either an outdoor LV power distribution network, or an industrial or marine power system. The purpose of the experimental campaign has been to deeply investigate the feasibility of PLC solutions within the microgrid, in order to study the possibility to migrate to advanced remote control and monitoring SG applications in the outdoor and industrial scenarios.

We have performed an in-depth analysis of the characteristics of the channel that are due to the structure of the network, e.g., the presence of three phases. We have found that the phases are interchangeable because the channel frequency response seems to be not a function of the specific phase. Therefore, when the transmitter and the receiver are connected to different phases, NB PLC solutions are not suited due to the high attenuation of the channel in the lower frequency range.

Then, we have analyzed the impact of the loads on the channel frequency response, the line impedance and the background noise. Firstly, we have found that the presence of loads may turn into less attenuated channels. Therefore, the measured channels exhibit a low time-variation, i.e., the non-linearities of the loads are negligible. From the analysis of the line impedance, we have pointed out the differences due to the loads, and the lowest and the mean impedance values that we have measured in the Cenelec bands A, B and C. Finally, from the analysis of the measured background noise, we have found that the inverters are

responsible for the highest noise values and we have provided an analytical expression to model the highest, mean and lowest power spectral density profile.

In the BB frequency range, we have limited the study to the channel frequency response. We have found that the interchangeability of the phases holds true and, further, the channel frequency response is similar regardless the loads and the phase where transmitter and receiver are connected to.

Finally, we have tested commercial PLC devices that operate in the NB and BB frequency range. We have considered several configurations, and we have found that the presence of inverters close to the communication nodes compromises NB transmissions. Indeed, BB PLC ensure high speeds even for communications across phases. Therefore, BB PLC are a suitable candidate for PLC in the industrial scenario.

In-home PLC Characterization of Load Impedance and Noise

We have dealt with the analysis of the impact of the electrical devices (loads) connected to the power grid on the PLC medium characteristics and on the quality of the data communication. Their behavior has been investigated both in the time and frequency domain, in terms of load impedance and impulsive noise components that they inject into the network, in the NB and BB frequency band. We have performed a measurement campaign on a large set of devices that can be found in a typical house or office, i.e., a number of home appliances, office equipment and lightning system components.

Firstly, we have investigated the frequency behavior of such devices in terms of voltage-to-current relation between the two feeding conductor, i.e., the line and the neutral wires, in the frequency range 2-30 MHz. Due to the fact that some devices exhibit a periodically time variant impedance with repetition frequency that is an integer multiple of the mains frequency. Interestingly, we have found a limited number of devices characterized by a strong time variant behavior. We have found that the cause of the impedance time variations is simply due to the front-end circuitry of the power supply unit of these devices. Furthermore, the deployment of EMI filters or noise suppression capacitors between the line and the neutral terminals significantly reduces the time variations. We have experimentally proved the above considerations and we have shown the results. Our measurement campaign has also considered the effect of the power cord on the resulting impedance of the devices. Finally, we have proposed a classification of the measured devices according to their time/frequency characteristics.

Thus, we have performed noise at the source measurements in order to deeply characterize the noise injected by any single appliance. We have found that, beyond 15 MHz, the devices do not inject noise. The periodic impulsive asynchronous with the mains components are concentrated below 6 MHz and they do not dependent on the time instant. Instead, the synchronous with the mains components cyclically vary with a repetition rate of 100 Hz. Finally, we have targeted the asynchronous impulsive noise. We have measured noise spikes

greater than 50 V that lasts up to 4 ms.

In-ship PLC

Applications and benefits that the deployment of PLC in a ship environment can bring, have justified our research activity targeting the study of channel characteristics. We have summarized the results of a PLC channel measurement campaign that we have carried out in the LV distribution network of a large cruise ship.

The analysis has shown that the channel statistics are similar to those reported in other application scenarios, e.g., the in-home scenario. Nevertheless, the LV in-ship channels can carry high amount of data information as the analysis of the capacity has shown. This is in excess of 200 Mbps and up to about 600 Mbps for the band of the BB commercial devices, i.e., 2-28 MHz, depending on the noise conditions and on the power grid section. It increases by up to 85% in the band 2-50 MHz. In particular, the links between the MV/LV substation and the distribution boards have higher capacity than the links between the distribution boards and the room service panels. Theoretical capacity can be approximately doubled if a MIMO transmission scheme is used, which is applicable to three-phase electrical power distribution system.

In-car PLC

We have presented the results of an entire PLC noise and channel measurement campaign that we have performed in a compact electrical car. We have set our focus on the noise caused by the electric and electronic components of the vehicle. We have demonstrated that the main noise sources are the DC/DC converter and the concatenated voltage generated by the high amount of current that flows to the electric engines. We have derived an analytical model for the harmonic content of the NB PLC noise, and we have given an overview to the BB harmonic components. Furthermore, from measures, we have studied the potential data transmission performance in terms of theoretical achievable rate. We have addressed both the NB spectrum, i.e., the Cenelec bands A, B, and C, and the BB. In the NB, the achievable data rate is in excess of 60 kbps and up to 300 kbps depending on the considered band and the vehicle state. In particular, performance decreases by up to 25% when the electric engines run under heavy load conditions. Conversely, the BB PLC channel can potentially convey high data rate. Thus, practical schemes that provide high speed and reliable communications can be deployed.

Appendix A

Scattering Theory

Consider the N-port network of Fig. A.1. In a microwave network, a port may be any generic transmission line supporting a propagation mode, i.e., that acts as a waveguide. V_n^+ and V_n^- are, respectively, the amplitudes (magnitude and phase) of the incident and reflected voltage waves on port n, at frequency f. We neglect the frequency dependency for notation simplicity. In a dual manner, I_n^+ and I_n^- are, respectively, the amplitudes (magnitude and phase) of the incident and reflected current waves on port n, at frequency f. Now, at the port n, the total voltage and current is given by

$$V_n = V_n^+ + V_n^- \tag{A.1}$$

$$I_n = I_n^+ - I_n^-. \tag{A.2}$$

$Z_{0,n}$ is the characteristic impedance of the port n and, in general, it is not the same for all ports. Thus, in [71], a new set of generalized wave amplitudes is defined as

$$a_n = V_n^+ / \sqrt{Z_{0,n}} \tag{A.3}$$

$$b_n = V_n^- / \sqrt{Z_{0,n}} \tag{A.4}$$

where a_n represents the incident wave on port n and b_n represents the reflected wave on port n. The scattering matrix $\mathbf{S}$ is defined as the matrix of the elements that relate the generalized wave amplitudes as follows

$$\begin{bmatrix} b_1 \\ b_2 \\ \vdots \\ b_N \end{bmatrix} = \underbrace{\begin{bmatrix} S_{11} & S_{12} & \dots & S_{1N} \\ S_{21} & S_{22} & \dots & \vdots \\ \vdots & \vdots & \ddots & \vdots \\ S_{N1} & \dots & \dots & S_{NN} \end{bmatrix}}_{\mathbf{S}} \begin{bmatrix} a_1 \\ a_2 \\ \vdots \\ a_N \end{bmatrix}. \tag{A.5}$$

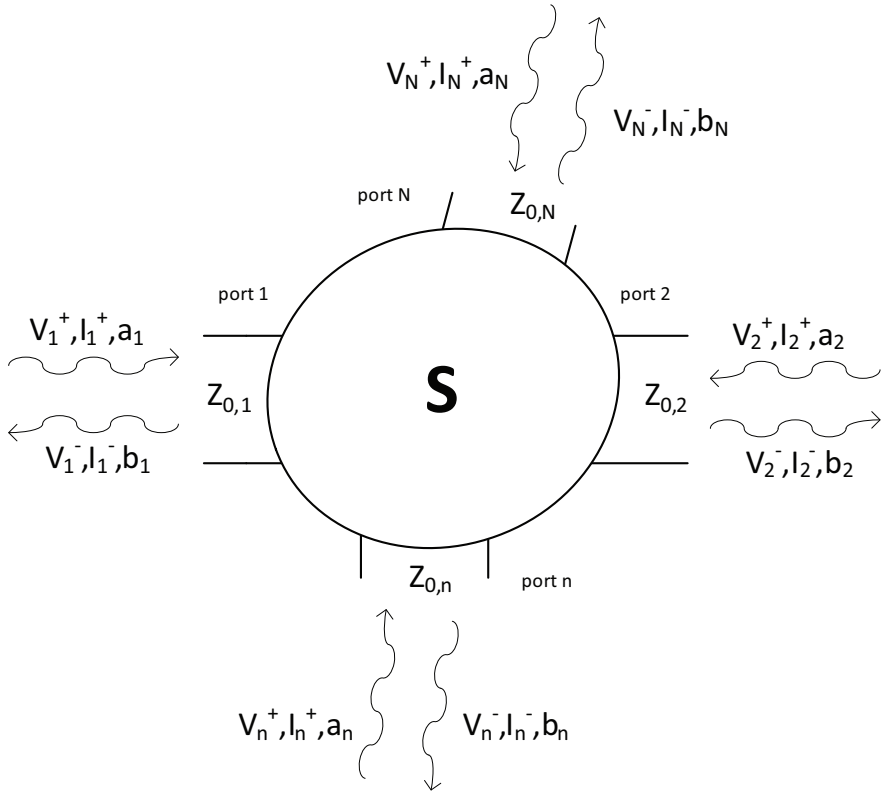

Figure A.1: Incident and reflected waves on ports of the N-port network.

The elements of **S** are determined as

$$S_{ij} = \left.\frac{b_i}{a_j}\right|_{a_k=0 \text{ for } k\neq j} = \left.\frac{V_i^- \sqrt{Z_{0,j}}}{V_j^+ \sqrt{Z_{0,i}}}\right|_{V_k^+=0 \text{ for } k\neq j} . \tag{A.6}$$

Each element is determined by considering the amplitude of the incident voltage wave on port j and the amplitude of the reflected voltage wave on port i, i.e., coming out of port i [71]. All the ports except the port j are terminated in matched loads in order to avoid reflections. Thus, S_{ii} is the reflection coefficient, or scattering coefficient [72], at the port i when all other ports are terminated in matched loads, while S_{ij} is the transmission coefficient from port j to port i when all other ports are terminated in matched loads [71].

Now, we consider the same (real) characteristic impedance for all ports, i.e., $Z_{0,n} = Z_0$ for all ports. Thus, A.5 simplifies as follow [71], [72]

$$\begin{bmatrix} V_1^- \\ V_2^- \\ \vdots \\ V_N^- \end{bmatrix} = \underbrace{\begin{bmatrix} S_{11} & S_{12} & \dots & S_{1N} \\ S_{21} & S_{22} & \dots & \vdots \\ \vdots & \vdots & \ddots & \vdots \\ S_{N1} & \dots & \dots & S_{NN} \end{bmatrix}}_{\mathbf{S}} \begin{bmatrix} V_1^+ \\ V_2^+ \\ \vdots \\ V_N^+ \end{bmatrix} . \tag{A.7}$$

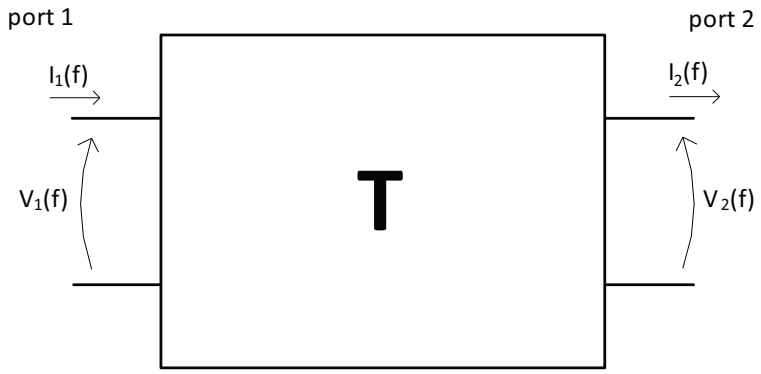

Figure A.2: Voltages and currents of the ports of the two-port network.

In this sense, the elements of the scattering matrix relate the incident and reflected voltage waves on the ports of the N-port network.

Transmission Matrix Representation

In practice, a complex microwave network consists of the cascade connection of multiple two-port networks [71]. For each individual two-port network (cf. Fig. A.2), the transmission matrix **T** relates the voltages and the currents of the ports of the network as follows

$$\begin{bmatrix} V_1 \\ I_I \end{bmatrix} = \underbrace{\begin{bmatrix} A & B \\ C & D \end{bmatrix}}_{\mathbf{T}} \begin{bmatrix} V_2 \\ I_2 \end{bmatrix}. \tag{A.8}$$

V_1 and I_1 are the phasors at frequency f of the voltage and of the current of the port 1. V_2 and I_2 are the phasors at frequency f of the voltage and of the current of the port 2. Note that I_1 flows into the port 1 while I_2 flows out of the port 2. The convention for the current of the port 2 is convenient when a cascade connection of multiple two-port networks is deployed because the (positive) current that flows out of the output port of a two-port network is the (positive) current that flows into the input port of the subsequent two-port network. Thus, the transmission matrix of the cascade is equal to the product of the transmission matrices representing the individual networks. This property is known as the chain rule of the transmission matrices.

The transmission matrix elements can be obtained from the scattering parameters of a two-port network as follows [71]

$$A = \frac{1 + S_{11} - S_{22} - \Delta S}{2S_{21}}, \tag{A.9}$$

$$B = Z_0 \frac{1 + S_{11} + S_{22} + \Delta S}{2S_{21}}, \tag{A.10}$$

$$C = \frac{1 - S_{11} - S_{22} + \Delta S}{2Z_0 S_{21}}, \tag{A.11}$$

$$D = \frac{1 - S_{11} + S_{22} - \Delta S}{2S_{21}}, \tag{A.12}$$

where $\Delta S = S_{11}S_{22} - S_{12}S_{21}$.

Appendix B

EMI Filter

An electromagnetic interference (EMI) filter is a low-pass passive filter properly designed to suppress the electromagnetic and the noise emissions generated by the electronic devices and conducted through the line, neutral and ground wires to the power grid. For the conducted emissions, the electromagnetic norms EN 55022/CISPR 22 regulate the frequency range from 150 kHz to 30 MHz [35]. Two distinct components can be distinguished, i.e., the differential mode (DM) and the common mode (CM) emissions. The DM ones are those that flow from the line (hot) conductor to the neutral wire, while the CM emissions flow in the same direction on the line and the neutral conductors and return through the ground. As depicted in Fig. B.1, the EMI filter is essentially composed of a capacitive and an inductive part. The capacitive part consists of two kind of capacitors which provide bypass paths to the high frequency currents. C_x denotes the line-to-line capacitor, also known as X-cap [35], installed between the line and neutral terminals. At high frequencies, the C_x capacitor acts as a short circuit path for the differential mode currents and it can assume high capacitance values, i.e., typically tens or hundreds nF [35]. Therefore, at the mains frequency of 50 Hz, the effect of the X-cap is negligible, so that its does not interfere with the feeding power signal. C_y denotes the two line-to-ground capacitors, or Y-caps [35], between the line and the ground terminals and between the neutral and the ground wires. The two capacitors are used to suppress common mode currents. Typical values are few nF [35], due to safety reasons. In fact, low impedance paths between the line (or the neutral) wires and the ground conductor have to be avoided at frequency 50 Hz.

The inductive part is essentially composed of a common mode choke, represented in Fig. B.1 by the two coupled inductors (L_1, L_2 and the mutual inductance M) that acts as a transparent device at frequency 50 Hz for the mains signal and blocks the common mode currents at high frequencies.

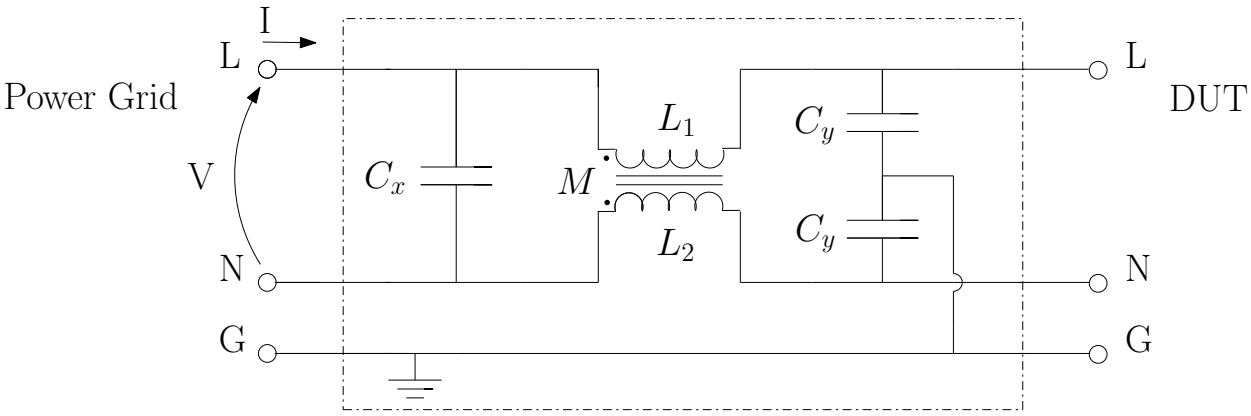

Figure B.1: Circuit schematic of a typical EMI filter.

Bibliography

[1] H. C. Ferreira, L. Lampe, J. Newbury, and T. G. Swart, *Power Line Communications: Theory and Applications for Narrowband and Broadband Communications over Power Lines*. NY: Wiley & Sons, 2010.

[2] ERDF, *PLC G3 Physical Layer Specification*. [Online] Available: http://www.maximintegrated.com/products/powerline/pdfs/G3-PLC-Physical-Layer-Specification.pdf.

[3] PRIME Alliance Technical Working Group, *Draft Standard for PoweRline Intelligent Metering Evolution*. [Online] Available: http://www.prime-alliance.org.

[4] Maxim Integrated, *Supplement to PLC G3 physical layer specification for operation in CENELEC B/C/BC/D/BCD/BD frequency bands*. [Online] Available: http://www.maximintegrated.com/products/powerline/pdfs/G3-PLC-CENELEC-Supplement-B.pdf.

[5] Maxim Integrated, *Supplement to PLC G3 physical layer specifications for operation in the FCC frequency band*. [Online] Available: http://www.maximintegrated.com/products/powerline/pdfs/G3-PLC-FCC-Supplement-B.pdf.

[6] Maxim Integrated, *PLC G3 MAC Layer Specification*. [Online] Available: http://www.maximintegrated.com/products/powerline/pdfs/G3-PLC-MAC-Layer-Specification.pdf.

[7] Home Plug Alliance, *Home Plug Alliance*. http://www.homeplug.org.

[8] HD-PLC Alliance, *High Definition Power Line Communication*. http://www.hd-plc.org/.

[9] IEEE P1901 Working Group, *IEEE Standard for Broadband over Power Line Networks: Medium Access Control and Physical Layer Specifications*. http://grouper.ieee.org/groups/1901/.

[10] F. Versolatto, *Ph.D. Thesis - Power Line Communications: Channel Characterization and Modeling*. University of Udine, 2013.

[11] M. Korki, N. Hosseinzadeh, H. L. Vu, T. Moazzeni, and C. H. Foh, "A Channel Model for Power Line Communication in the Smart Grid," in *Proc. of IEEE/PES Power Systems Conference and Exposition (PSCE)*, pp. 1–7, Mar. 2011.

[12] E. Bakhoum, "S-Parameters Model for Data Communications over 3-Phase Transmission Lines," *IEEE Transactions on Smart Grid*, vol. 2, pp. 615–623, Dec. 2011.

[13] Z. Mingyue, "Measurements and Channel Characteristics of LV Power Line Communications Networks in China," in *Proc. of IEEE Int. Symp. on Power Line Commun. and Its App. (ISPLC)*, pp. 212–216, Mar. 2006.

[14] G. T. Andreou, D. P. Labridis, and G. K. Papagiannis, "Modeling of Low Voltage Distribution Cables for Powerline Communications," in *Proc. of IEEE Power Tech Conference*, p. 6, Jun. 2003.

[15] H. A. Cabral, U. R. C. Vitor, and M. T. de Melo, "Analysis of Noise and Transfer Function Characteristics in a Three-phase Electrical Infrastructure," in *Proc. of IEEE Int. Symp. on Power Line Commun. and Its App. (ISPLC)*, pp. 137–141, Mar. 2010.

[16] M. Zhai and Q. Zeng, "Signal Propagation on Three Phases Power Distribution Lines as Communications Channels for Intelligent Systems," in *Proc. of First Int. Conf. on Innovative Computing, Information and Control (ICICIC)*, pp. 437–40, Aug. 2006.

[17] S. Sun, Y. Wang and C. Wang, "Study on the Behaviour of Access Domain PLC Channel with Low Rate, Low-Voltage," in *Proc. of Int. Workshop on Intelligent Systems and Applications (ISA)*, pp. 1–4, May 2009.

[18] M. Gotz, M. Rapp, and K. Doster, "Power Line Channel Characteristics and Their Effect on Communication System Design," *IEEE Communication Magazine*, vol. 42, pp. 78–86, Apr. 2004.

[19] J. E. Newbury and K. J. Morris, "Power Line Carrier Systems for Industrial Control Applications," *IEEE Transactions on Power Delivery*, vol. 14, pp. 1191–1196, Oct. 1999.

[20] M. A. Mannah, C. Batard, and N. G. M. Machmoun, "Power Line Communication over Feeder Cables in an Industrial Environment," in *Proc. of IEEE Int. Symp. on Power Line Commun. and Its App. (ISPLC)*, pp. 255–260, Mar.-Apr. 2009.

[21] C. Konate, A. Kosonen, J. Ahola, M. Machmoum, and J. F. Diouris, "Power Line Communication in Motor Cables of Inverter-Fed Electric Drives," *IEEE Transactions on Power Delivery*, vol. 25, pp. 125–131, Jan. 2010.

[22] Z. Hua, J. Wu, K. D. Mueller-Glaser, and O. Simon, "A Noise Analysis Based Channel Coding Technique for Multicarrier Channel of an Industrial PLC System," in *Proc. of*

IEEE Int. Symp. on Power Line Commun. and Its App. (ISPLC), pp. 22–26, Mar. 2006.

[23] V. Degardin, K. Kilani, P. Laly, M. Lienard, and P. Degauque, "Power Line Communication between an Inverter and a Motor: Noise Characterization in the Time Domain and in the Frequency Domain," in *Proc. of General Assembly and Scientific Symposium, XXXth URSI*, pp. 1–4, Aug. 2011.

[24] M. Antoniali and A. M. Tonello, "Characterization of Load Impedances in Home Power Line Grids," *IEEE Transactions on Instrumentation and Measurement*, submitted to, Feb. 2013.

[25] H. Philipps, "Modelling of Power Line Communication Channels," in *Proc. of IEEE Int. Symp. on Power Line Commun. and Its App. (ISPLC)*, pp. 14–21, Mar. 1999.

[26] F. J. Cañete, L. Díez, and J. Entrambasaguas, "Indoor Power-Line Communications: Channel Modelling and Measurements," in *Proc. of IEEE Int. Symp. on Power Line Commun. and Its App. (ISPLC)*, pp. 117–122, Apr. 2000.

[27] M. Zimmermann and K. Dostert, "A Multipath Model for the Powerline Channel," *IEEE Transactions on Communications*, vol. 50, pp. 553–559, Apr. 2002.

[28] S. Barmada, A. Musolino, and M. Raugi, "Upper and Lower Bounds for Frequency Response of PLC Channels in Presence of Load Variations," in *Proc. of Int. Symp. on Power Line Commun. and Its App. (ISPLC)*, pp. 12–15, Mar. 2006.

[29] J. Anatory, N. Theethayi, R. Thottappillil, M. M. Kissaka, and N. H. Mvungi, "The Influence of Load Impedance, Line Length, and Branches on Underground Cable Power-Line Communications (PLC) Systems," *IEEE Transactions on Power Delivery*, vol. 23, pp. 180–187, Jan. 2008.

[30] D. Hirata, N. Kuwabara, Y. Akiyama, and H. Yamane, "Influence of Appliance State on Transmission Characteristics of Indoor AC Mains Lines in Frequency Range Used Power Line Communication," in *Proc. of Int. Symp. on Electromagnetic Compatibility (EMC)*, pp. 715–720, Aug. 2005.

[31] F. J. Cañete, J. A. Cortés, L. Díez, and J. T. Entrambasaguas, "Analysis of the Cyclic Short-Term Variation of Indoor Power Line Channels," *IEEE Journal on Selected Areas in Communications*, vol. 24, pp. 1327–1338, Jul. 2006.

[32] T. Esmailian, F. R. Kschischang, and P. G. Gulak, "In-Building Power Lines as High-Speed Communication Channels: Channel Characterization and a Test Channel Ensemble," *Int. Journal of Communication Systems*, vol. 16, pp. 381–400, Jun. 2003.

[33] A. M. Tonello and F. Versolatto, "Bottom-Up Statistical PLC Channel Modeling-Part I: Random Topology Model and Efficient Transfer Function Computation," *IEEE Transactions on Power Delivery*, vol. 26, pp. 891–898, Apr. 2011.

[34] A. M. Tonello and F. Versolatto, "Bottom-Up Statistical PLC Channel Modeling-Part II: Inferring the Statistics," *IEEE Transactions on Power Delivery*, vol. 25, pp. 2356–2363, Oct. 2010.

[35] R. P. Clayton, *Introduction to Electromagnetic Compatibility, 2nd Edition.* Wiley-Interscience, 2005.

[36] R. P. Clayton, *Analysis of Multiconductor Transmission Lines, 2nd Edition.* Wiley-IEEE Press, 2007.

[37] R. Hashmat, P. Pagani, and T. Chonavel, "MIMO Communications for Inhome PLC Networks: Measurements and Results up to 100 MHz," in *Proc. of IEEE Int. Symp. on Power Line Commun. and Its App. (ISPLC)*, pp. 120–124, Apr. 2010.

[38] M. Zimmermann and K. Dostert, "Analysis and Modeling of Impulsive Noise in Broadband Powerline Communications," *IEEE Transactions on Electromagnetic Compatibility*, vol. 44, pp. 249–258, Feb. 2002.

[39] J. A. Cortés, L. Díez, F. J. Cañete, and J. J. Sánchez-Martínez, "Analysis of the Indoor Broadband Power-Line Noise Scenario," *IEEE Transactions on Electromagnetic Compatibility*, vol. 52, pp. 849–858, Nov. 2010.

[40] M. Nassar, K. Gulati, Y. Mortazavi, and B. L. Evans, "Statistical Modeling of Asynchronous Impulsive Noise in Powerline Communication Networks," in *Proc. of IEEE Global Communications Conference (GLOBECOM)*, pp. 1–6, Dec. 2011.

[41] J. Khangosstar, Li Zhang and A. Mehboob, "An Experimental Analysis in Time and Frequency Domain of Impulse Noise over Power Lines," in *Proc. of Int. Symp. on Power Line Commun. and Its App. (ISPLC)*, pp. 218–224, Apr. 2011.

[42] M. Tlich, H. Chaouche, A. Zeddam, and F. Gauthier, "Impulsive Noise Characterization at the Source," in *Proc. of IFIP Wireless Days (WD)*, pp. 1–6, Nov. 2008.

[43] F. Gianaroli, F. Pancaldi, E. Sironi, M. Vigilante, G. M. Vitetta, and A. Barbieri, "Statistical Modeling of Periodic Impulsive Noise in Indoor Power-line Channels," *IEEE Transactions on Power Delivery*, vol. 27, pp. 1276–1283, Jul. 2012.

[44] H. Meng, Y. L. Guan, and S. Chen, "Modeling and Analysis of Noise Effects on Broadband Power-Line Communications," *IEEE Transactions on Power Delivery*, vol. 20, pp. 630–637, Apr. 2005.

[45] J. A. Cortés, L. Díez, F. J. Cañete, and J. J. Sánchez-Martínez, "Analysis of the Periodic Impulsive Noise Asynchronous with the Mains in Indoor PLC Channels," in *Proc. of Int. Symp. on Power Line Commun. and Its App. (ISPLC)*, pp. 26–30, Mar. 2009.

[46] S. Tsuzuki, M. Yoshida, Y. Yamada, H. Kawasaki, K. Murai, K. Matsuyama, and M. Suzuki, "Characteristics of Power-Line Channels in Cargo Ships," in *Proc. of IEEE Int. Symp. on Power Line Commun. and Its App. (ISPLC)*, pp. 324–329, Mar. 2007.

[47] S. Barmada, L. Bellanti, M. Raugi, and M. Tucci, "Analysis of Power-Line Communication Channels in Ships," *IEEE Transactions on Vehicular Technology*, vol. 59, pp. 3161–3170, Sept. 2001.

[48] J. Nishioka, S. Tsuzuki, M. Yoshida, H. Kawasaki, T. Shinpo, and Y. Yamada, "Characteristics of 440V Power-Line Channels in Container Ships," in *Proc. of IEEE Int. Symp. on Power Line Commun. and Its App. (ISPLC)*, pp. 217–222, Mar.-Apr. 2009.

[49] M. Yoshida, S. Tsuzuki, Y. Yamada, K. Murai, M. Takechi, K. Matsuyama, T. Shinpo, Y. Saito, and S. Takaoka, "Characteristics of Power-Line Channels in the Training Ship YUGEMARU," in *IEICE Technical Report, Vol. 07, N. 257, WBS2007-46*, pp. 41–46, Oct. 2007.

[50] M. Yoshida, S. Tsuzuki, Y. Yamada, H. Kawasaki, K. Murai, K. Matsuyama, T. Shinpo, Y. Saito, and S. Takaoka, "A Study of Unintentional Radiation by PLC in Ships," in *Proc. of Electronics, Information and Systems Society Conference*, Sept. 2007.

[51] S. Tsuzuki, M. Yoshida, Y. Yamada, K. Murai, H. Kawasaki, K.Matsuyama, T. Shinpo, Y. Saito, and S. Takaoka, "Channel Characteristic Comparison of Armored Shipboard Cable and Unarmored one," in *Proc. of IEEE Int. Symp. on Power Line Commun. and Its App. (ISPLC)*, pp. 7–12, Apr. 2008.

[52] E. Liu, Y. Gao, G. Samdani, O. Mukhtar, and T. Korhonen, "Powerline Communication over Special Systems," in *Proc. of IEEE Int. Symp. on Power Line Commun. and Its App. (ISPLC)*, pp. 167–171, Apr. 2005.

[53] S. Galli, "A Simplified Model for the Indoor Power Line Channel," in *Proc. of IEEE Int. Symp. on Power Line Commun. and Its App. (ISPLC)*, pp. 13–19, Apr. 2009.

[54] A. M. Tonello, *Brief Tutorial on the Statistical Top-Down PLC Channel Generator*. [Online]. Available: `http://www.diegm.uniud.it/tonello/PAPERS/WHITE/TUTORIAL_CHAN_2010.pdf`, 2010.

[55] A. Schiffer, "Statistical Channel and Noise Modeling of Vehicular DC-lines for Data Communication," in *Proc. of IEEE Vehicular Technology Conf. (VTC)*, pp. 158–162, May. 2000.

[56] P. A. J. van Rensburg and H. C. Ferreira, "Automotive Power-Line Communications: Favourable Topology for Future Automotive Electronic Trends," in *Proc. of IEEE Int. Symp. on Power Line Commun. and Its App. (ISPLC)*, pp. 103–108, Mar. 2003.

[57] P. A. J. van Rensburg, H. C. Ferreira, and A. J. Snyders, "An Experimental Setup for In-circuit Optimization of Broadband Automotive Power-line communications," in *Proc. of IEEE Int. Symp. on Power Line Commun. and Its App. (ISPLC)*, pp. 322–325, Apr. 2005.

[58] T. Huck, J. Schirmer, and K. Dostert, "Tutorial about the Implementation of a Vehicular High Speed Communication System," in *Proc. of IEEE Int. Symp. on Power Line Commun. and Its App. (ISPLC)*, pp. 162–166, Apr. 2005.

[59] M. O. Carrion, M. Lienard, and P. Degauque, "Communication over Vehicular DC Lines: Propagation Channel Characteristics," in *Proc. of IEEE Int. Symp. on Power Line Commun. and Its App. (ISPLC)*, pp. 2–5, Mar. 2006.

[60] W. Gouret, F. Nouvel, and G. El-Zein, "Powerline Communication on Automotive Network," in *Proc. of IEEE Vehicular Technology Conf. (VTC)*, pp. 2545–2549, Apr. 2007.

[61] V. Degardin, M. Lienard, P. Degauque, and P. Laly, "Performances of the HomePlug PHY Layer in the Context of In-Vehicle Powerline Communications," in *Proc. of IEEE Int. Symp. on Power Line Commun. and Its App. (ISPLC)*, pp. 93–97, Mar. 2007.

[62] M. Lienard, M. Carrion, V. Degardin, and V. Degauque, "Modeling and Analysis of In-Vehicle Power Line Communication Channels," *IEEE Transactions on Vehicular Technology*, vol. 57, pp. 670–679, Mar. 2008.

[63] V. Degardin, M. Lienard, P. Degauque, E. Simon, and P. Laly, "Impulsive Noise Characterization of In-Vehicle Power Line," *IEEE Transactions on Electromagnetic Compatibility*, vol. 50, pp. 861–868, Nov. 2008.

[64] M. Mohammadi, L. Lampe, M. Lok, S. Mirabbasi, M. Mirvakili, R. Rosales, and P. van Veen, "Measurement Study and Transmission for In-Vehicle Power Line Communication," in *Proc. of IEEE Int. Symp. on Power Line Commun. and Its App. (ISPLC)*, pp. 73–78, Mar.-Apr. 2009.

[65] A. B. Vallejo-Mora, J. J. Sáchez-Martínez, F. J. Cañete, J. A. Cortés, and L. Díez, "Characterization and Evaluation of In-Vehicle Power Line Channels," in *Proc. of IEEE Global Communications Conference (GLOBECOM)*, pp. 1–5, Dec. 2010.

[66] J. A. Cortés, M. Cerdá, L. Díez, and F. J. Cañete, "Analysis of the Periodic Noise on In-vehicle Broadband Power Line Channels," in *Proc. of IEEE Int. Symp. on Power Line Commun. and Its App. (ISPLC)*, pp. 334–339, Mar. 2012.

[67] S. Barmada, M. Raugi, M. Tucci, and T. Zheng, "Power Line Communication in a Full Electric Vehicle: Measurements, Modelling and Analysis," in *Proc. of IEEE Int. Symp. on Power Line Commun. and Its App. (ISPLC)*, p. 2010, Mar. 331-336.

[68] N. Taherinejad, R. Rosales, L. Lampe, and S. Mirabbasi, "Channel Characterization for Power Line Communication in a Hybrid Electric Vehicle," in *Proc. of IEEE Int. Symp. on Power Line Commun. and Its App. (ISPLC)*, pp. 328–333, Mar. 2012.

[69] Estrima S.r.l., *Birò*. `http://www.estrima.com`.

[70] M. Antoniali, M. Girotto, and A. M. Tonello, "In-car Power Line Communications: Advanced Transmission Techniques," *Int. Journal of Automotive Technology*, accepted, Dec. 2012.

[71] D. M. Pozar, *Microwave Engineering, 2nd Edition*. Wiley & Sons, 1998.

[72] R. E. Collin, *Foundations For Microwave Engineering, 2nd Edition*. Wiley-Interscience, 2001.